Study of exotic decay near proton drip line

by

Priyabrata Das

PHYS05201804021

Saha Institute of Nuclear Physics, Kolkata

A Thesis Submitted to the

Board of Studies in Physical Sciences

In partial fulfillment of requirements

For the Degree of

Doctor of Philosophy

of

HOMI BHABHA NATIONAL INSTITUTE

April, 2024

Homi Bhabha National Institute

Recommendations of the Viva Voce Committee

As members of the Viva Voce Committee, we certify that we have read the dissertation prepared by **Priyabrata Das** entitled **'Study of exotic decay near proton drip line'** and recommend that it maybe accepted as fulfilling the thesis requirement for the award of degree of Doctor of Philosophy.

M. K. Agrawal ______________________________ Date: 03/04/2024

Chairman - Professor Bijay Kumar Agrawal

Ushasi Datta ______________________________ Date: 03/04/2024

Guide / Convener - Professor Ushasi Datta

B P Singh ______________________________ Date: 03/04/2024

Examiner - Professor Bhanu Prakash Singh

______________________________ Date: 03/04/2024

Member 1 - Professor Sukalyan Chattopadhyay

Debasish Majumdar ______________________________ Date: 03/04/2024

Member 2 - Professor Debasish Majumdar

G. Gangopadhyay ______________________________ Date: 03/04/2024

Member 3 - Professor Gautam Gangopadhyay

Final approval and acceptance of this thesis is contingent upon the candidate's submission of the final copies of the thesis to HBNI.

I hereby certify that I have read this thesis prepared under my direction and recommend that it may be accepted as fulfilling the thesis requirement.

Ushasi Datta

Signature

Date: 03/04/2024

Place: Kolkata

Guide: PROF USHASI DATTA

STATEMENT BY AUTHOR

This dissertation has been submitted in partial fulfillment of requirements for an advanced degree at Homi Bhabha National Institute (HBNI) and is deposited in the library to be made available to borrowers under rules of the HBNI.

Brief quotations from this dissertation are allowable without special permission, provided that accurate acknowledgment of the source is made. Requests for permission for extended quotation from or reproduction of this manuscript in whole or in part may be granted by the competent authority of HBNI when in his or her judgment the proposed use of the material is in the interests of scholarship. In all other instances, however, permission must be obtained from the author.

Priyabrata Das

Priyabrata Das

DECLARATION

I hereby declare that the investigation presented in the thesis has been carried out by me. The work is original and has not been submitted earlier as a whole or in part for a degree/ diploma at this or any other institution/ university.

Ushasi Datta
Professor Ushasi Datta

Priyabrata Das
Priyabrata Das

Annexure 1

CERTIFICATION ON ACADEMIC INTEGRITY

1. I **PRIYABRATA DAS** HBNI Enrolment No. **PHYS05201804021** hereby undertake that, the Thesis titled ***"STUDY OF EXOTIC DECAY NEAR PROTON DRIP LINE"*** is prepared by me and that the document reports the original work carried out by me and is free of plagiarism.

2. I am aware and undertake that if plagiarism is detected in my thesis at any stage in future, suitable penalty will be imposed as per the applicable guidelines of the Institute/ UGC.

Priyabrata Das
30/10/2023
Signature of the Student
(with date)

Endorsed by the PhD Supervisor

Ushasi Datta 30/10/2023
Signature (with date)

Name: Ushasi Datta
Designation: Senior Professor "H"
Department/ Centre: Nuclear Physics Division
Name of the CI/ OCC: Saha Institute of Nuclear Physics

List of Publications

Publications included in the thesis

1. P. Das, U. Datta, *et al.*, *Exotic decay of* ^{115}Cs. , Phys. Rev. C **108**, 064304 (2023).

2. P. Das, U. Datta, *et al.*, *Study of exotic decay of Cs isotope close to the proton drip line.* , Journal of Physics. **1643**, 012127 (2020).

3. P. Das, U. Datta, *et al.*, *Study of exotic decay near proton drip-line.* , 64th DAE BRNS Symposium on nuclear physics, 304-305 (2019).

4. P. Das, U. Datta, *et al.*, *Bound and unbound states of* ^{115}Xe. , 65th DAE BRNS Symposium on nuclear physics, 202-203 (2021).

5. P. Das, U. Datta, *et al.*, *Particle unbound states of* ^{115}Xe. , 66th DAE BRNS Symposium on nuclear physics, 130-131 (2022).

Other publications

1. A. Bhattacharyya, U. Datta, P.Das, *et al.*, *Neutron capture cross sections of light neutron-rich nuclei relevant for r-process nucleosynthesis.* , Phys. Rev. C **104**, 4, 045801 (2021)..

2. A. Bhattacharyya, U. Datta, P.Das, *et al.*, *Measurement of Radiative Capture Cross-section relevant in Astrophysical Scenarios.* , 64th DAE BRNS Symposium on nuclear physics, 578-579 (2019).

3. J. Dey, U. Datta, P.Das, *et al.*, *Exotic decay of* ^{116}Cs. , 66th DAE BRNS Symposium on nuclear physics, 182-183 (2022).

4. S. Basak, D. Kumar, T. Bhattacharjee, U. Datta, P.Das, *et al.*, *New scenario of shape co-existence in* ^{152}Sm. , 66th DAE BRNS Symposium on nuclear physics, 108-109 (2022).

5. S. S. Nayak, S. Basu, G. Mukherjee, U. Datta, P.Das, *et al.*, *Evidence of collective excitations at low and medium spin in* ^{59}Ni. , 65th DAE BRNS Symposium on nuclear physics, 134-135 (2021).

Priyabrata Das

Priyabrata Das

Dedicated to
the people of my country

ACKNOWLEDGMENTS

It gives me great pleasure to place my indebtedness to my supervisor Prof. Ushasi Datta. Her expertise, enthusiasm, guidance, and immense dedication were the most instrumental in finishing my doctoral thesis. Her patience, encouragement, and unwavering support have contributed significantly to my growth as a researcher. I am also thankful to her for keeping her trust on me at trying times and for providing me with the opportunity to gather hands-on experience in experimental nuclear physics at the SINP-laboratory, and also at different national accelerator facilities. I express my sincere gratitude to my father, mother and wife for their unwavering support, encouragement, and care. Their presence and guidance have been instrumental in my journey. I would also like to extend my thanks to other family members and teachers who have provided continuous encouragement and motivation as I treated this path. I extend my thanks to Prof. María José García Borge, Prof. Olof Tengblad and other IS545 collaborators in the IDS project that have assisted in this work and also the ISOLDE (CERN) groups for their help and experience through which I have gained many of my nuclear-physics related knowledge. I also express my sincere gratitude to the Head of the Division of my department, the Director of my institute and Academic Dean of HBNI for their support, encouragement. I consider myself fortunate to have had Dr. Anisur Rahaman and Dr. Santosh Chakrabarty by my side when embarking on this journey. They have imparted valuable lessons that have shaped my path. I would also like to acknowledge to Joydip and Writabrata for their valueable support. I express my gratitude to the SINP, DAE and CSIR for giving me the chance and support to continue the years as a researcher. I am thankful to my friends and colleagues who generously shared their time with me by changing valuable to invalueable hours, are an integral part of my PhD days. I wish them all the success they deserve in the years to follow.

Priyabrata Das

ABSTRACT

Present thesis is reporting first detailed study of the β^+/EC decay of the very neutron-deficient, proton and alpha-unbound nucleus, ^{115}Cs. The measurement was performed at the ISOLDE, CERN. The delayed charged particles and γ-rays were detected by four sets of double-sided silicon strip detector with pad detector and clover detector-array, respectively. The observed delayed γ-rays are in agreement with the previously reported characteristics γ-rays of ^{115}Xe. Based on the experimental observations, the tentative ground state spin of ^{115}Cs is suggested to be $7/2^+$ or $9/2^+$. Furthermore, the measured decay branching ratio of delayed protons exceeds the previously reported value. Half life of ^{115}Cs has been measured from time distribution of proton spectrum and the half life is in agreement with previous reported value. Additionally, new delayed α-branching ratio and several reconstructed proton and α-unbound excited states of ^{115}Xe are being reported for the first time. The properties of proton unbound states at excitation energies from 3.9 MeV to 7.9 MeV have been obtained by fitting the delayed proton spectrum via the Bayesian method. The measured lifetimes of these proton-unbound states are in the order of zeptoseconds. The properties of unbound states above proton threshold may shades light for (p,γ) capture cross-section which is important for rp-process.

Contents

List of Figures

Chapter 1

Introduction

1.1 Atomic Nucleus

The nucleus is indeed the dense, central part of an atom, consisting of protons and neutrons. It accounts for more than 99.9 % of an atom's mass but it is 100,000 times smaller in size compared to the overall size of the atom. The term "nucleus" was derived from the Latin word "kernel of a nut", emphasizing its central and fundamental nature within the atom. The concept of the nucleus was first introduced by Michael Faraday in 1844 when he used the term to describe the central point of an atom. Ernest Rutherford described the exact meaning of nucleus in 1911. Fig 1.1 shows the schematic representation of atomic nucleus.

In 1911, Ernest Rutherford conducted an experiment in which he directed alpha particles at a gold foil. By analyzing the scattering patterns of these particles, he proposed the existence of a small, dense atomic nucleus at the center of an atom. Rutherford's model suggested that the atom consists of a positively charged nucleus, containing most of the mass, surrounded by negatively charged electrons in orbit. Rutherford's experiments indicated that the nucleus was much smaller in size compared to the overall atomic radius.

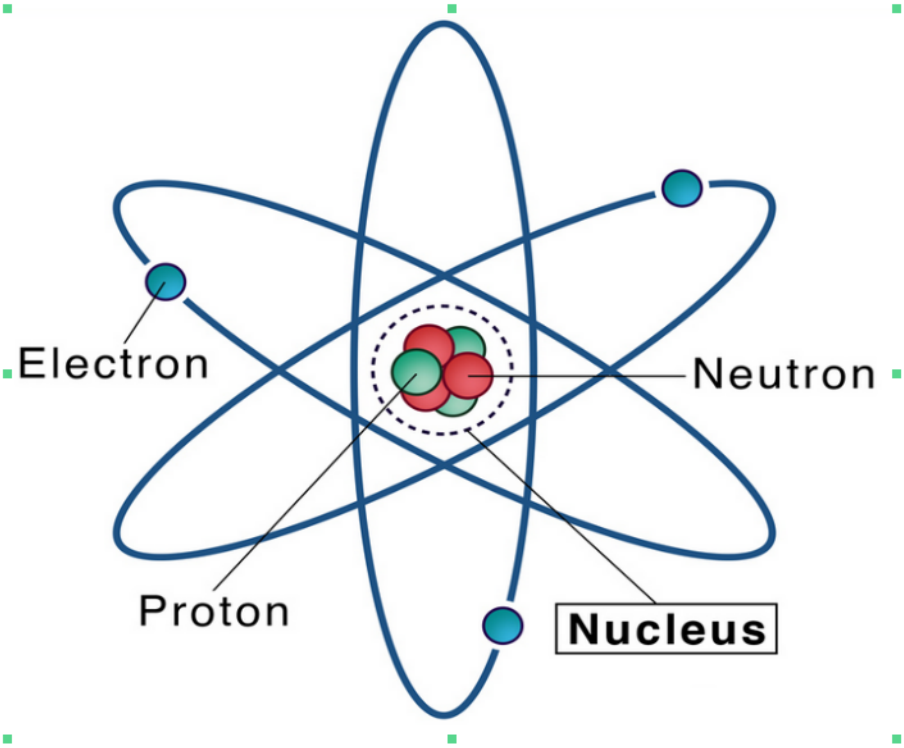

Figure 1.1: The schematic representation of Atomic Nucleus.

1.2 Stable isotope

Stable nuclides are nuclides that are not radioactive and so (unlike radionuclides) do not spontaneously undergo radioactive decay. In case of stable isotopes the half-life of a nuclide is comparable to, or greater than, the Earth's age (4.5 billion years), which is shown in Fig 1.2 by using black dots.

1.3 Nuclear models

Today, nuclear physics posits that the fundamental constituents of the atomic nucleus are quarks and gluons. These particles are bound together by the strong nuclear force, governed by the theory of quantum chromodynamics (QCD). One of the major challenges in nuclear physics is bridging the gap between the interactions of quarks (few-body) and the interactions among nucleons (many-body) that govern the structure and properties of nuclei. Theoretical predictions in nuclear physics are often made using models based on a few fundamental assumptions. The first suc-

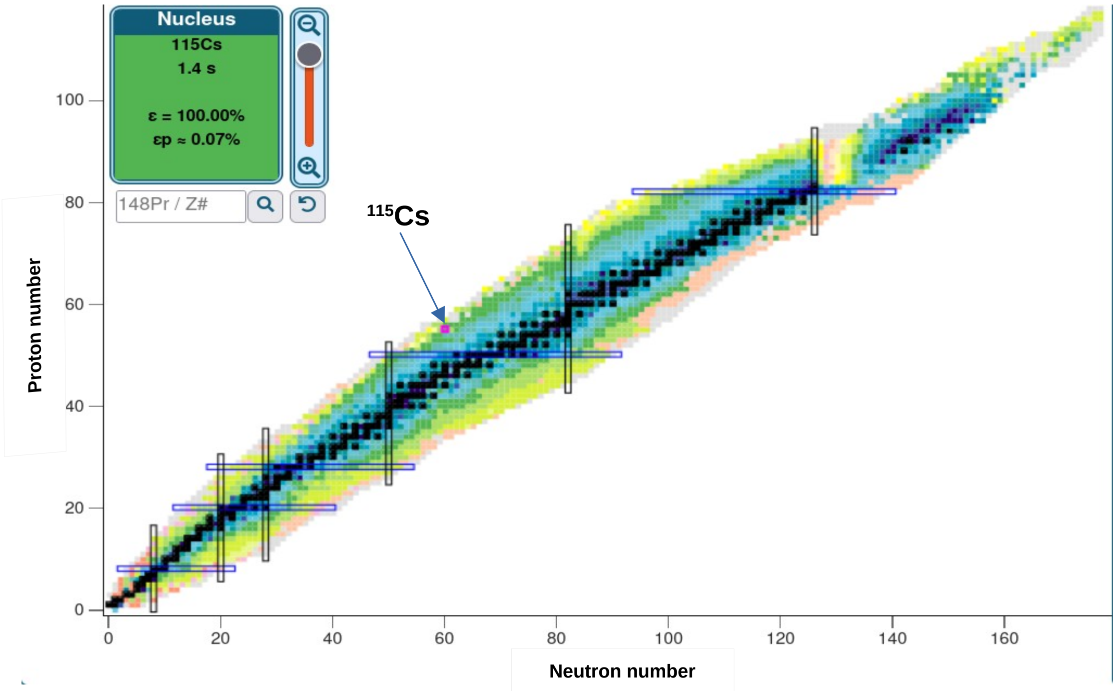

Figure 1.2: Nuclear landscape [1].

cessful nuclear model is liquid drop model, proposed by Gorge Gamow (1928). The liquid drop model treats the nucleus as a uniform sphere of nuclear matter, similar to an incompressible liquid droplet. That model extended by Carl Friedrich, von Weizsäcker and Niels Bohr. Later Meitner and Frisch (1938), using that extended liquid drop model explained the phenomenon of fission. In 1935, Weizsacker developed the Semi-Empirical Mass Formula based on this model, which described the general trend of binding energy in nuclei. However, it failed to account for certain peaks in the binding energy plot known as "magic numbers". The IPM (Independent particle model) assumes that nucleons move independently in an effective potential, taking into account the interaction with other nucleons. By filling energy levels according to the Pauli exclusion principle, the IPM successfully reproduces the magic numbers which is shown in Fig 1.3. The model incorporates a strong spin-orbit coupling in the effective potential, which helps explain the behavior of certain strongly bound nuclei. The independent particle model's success in explaining magic numbers led to Maria Goeppert Mayer and J. Hans D. Jensen being awarded the Nobel Prize in Physics in 1963.

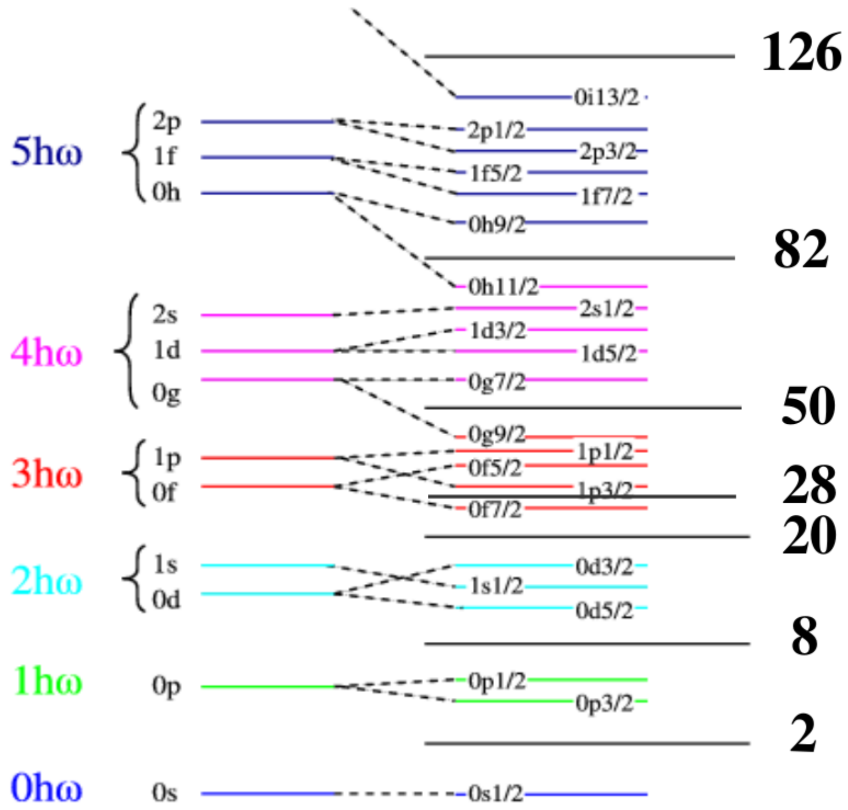

Figure 1.3: The schematic representation of shell structure inside nucleus.

The mean field models play a crucial role in describing the main part of the nuclear chart and understanding nuclear properties. However, no single model can fully capture all aspects of the nucleus or explain every nuclear property. Different models are required to describe different phenomena and properties. The development of mean field models has closely followed experimental results. As new experimental techniques and technologies emerge, they allow scientists to study more exotic and less-studied nuclei. By pushing the boundaries of experimental knowledge, researchers can gather data that helps refine and improve the existing models or develop new ones to explain the behavior of these exotic nuclei.This iterative process of experimentation and theoretical modeling is essential for advancing our understanding of nuclear physics. The interplay between theory and experiment allows scientists to test and refine models, uncover new phenomena, and deepen our knowledge of the nucleus. It also helps identify areas where current models fall short and guide future research directions.In summary, mean field models form a significant part of nuclear physics, but their development and improvement rely on ongoing experimental investigations and discoveries. By continually pushing the boundaries of what we can observe and measure, researchers can expand our knowledge of the nucleus and refine our theoretical models. However recent studies using Radioactive Ion Beam facility show these so called magic numbers are no longer applicable to the nuclei near dripline. So the fundamental question comes in - Is the existing nuclear theory need a major modification? A number of theoretical approach are being persuade. To validate various theoretical approaches, experimental data on the shell evolution, ground state properties of nuclei away from beta stability line is necessary. This thesis is a very tiny effort in that direction.

1.4 Drip lines

The first nuclear mass models demonstrated that certain ensembles of protons and neutrons are inherently unstable. That is to say, the ground-state configurations of such nuclei are energetically unstable to the emission of a constituent nucleon. For each element there are minimum and maximum numbers of neutrons that can be supported if the nucleus is to remain stable under nucleonic emission. These limits define the proton and neutron drip-lines which are shown in Fig 1.4.

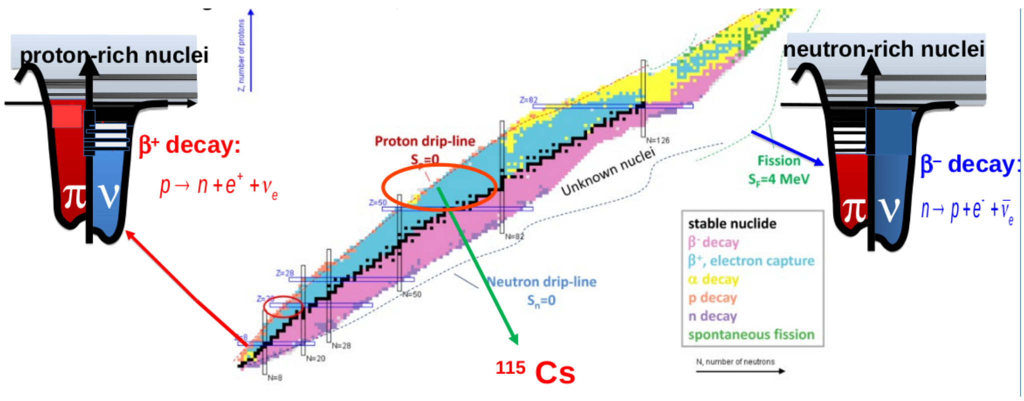

Figure 1.4: Nuclear Landscape.

The experimental data obtained from nuclei around the drip line is essential for validating nuclear models and refining our understanding of nucleon-nucleon interactions. By comparing the observed properties of these exotic nuclei with theoretical predictions, scientists can improve and refine nuclear models, which are essential for describing and predicting nuclear phenomena. Fig 1.4 describes the "nuclear landscape," a graphical representation of the arrangement of known nuclei on a chart. This chart displays the number of protons (atomic number) on the x-axis and the number of neutrons on the y-axis, allowing us to visualize the distribution of stable and unstable nuclei. The drip lines would be represented as boundaries beyond which nuclei become unstable and decay. Overall, the study of nuclei at the limits of stability near the drip lines offers a unique and valuable perspective on nuclear structure, properties, and interactions, providing insights into the fundamental building blocks of matter.

As the names suggest, too few neutrons causes a proton to be ejected, while too many neutrons will result in the emission of a neutron. Basically the nuclear drip line is the boundary delimiting the zone beyond which atomic nuclei decay by the emission of a proton or neutron. An arbitrary combination of protons and neutrons does not necessarily yield a stable nucleus. However, adding nucleons one at a time to a given nucleus will eventually lead to a newly formed nucleus that immediately decays by emitting a proton (or neutron). Colloquially speaking, the nucleon has 'leaked' or 'dripped' out of the nucleus, hence giving rise to the term "drip line". Drip lines are defined for protons and neutrons at the extreme of the proton-to-neutron ratio; at p:n ratios at or beyond the drip lines, no bound nuclei can exist. While the location of the proton drip line is well known for many elements, the location of the neutron drip line is only known for elements up to Neon. Nuclear stability is limited to those combinations of protons and neutrons described by the chart of the nuclides, also called the valley of stability. The boundaries of this valley are the neutron drip line on the neutron rich side, and the proton drip line on the proton-rich side. If one goes towards the proton drip line by reducing the number of neutron of a particular nucleus, the proton separation energy decreases and at the proton drip line proton separation energy becomes zero. Similarly if one goes towards the neutron drip line by increasing the number of neutron of a particular nucleus, the neutron separation energy decreases and at the neutron drip line neutron separation energy becomes zero. As such, the drip line may be defined as the boundary beyond which proton or neutron separation energy becomes negative, favoring the emission of a particle from a newly formed unbound system.The proton drip-line lies much closer to stability than does the neutron drip-line.

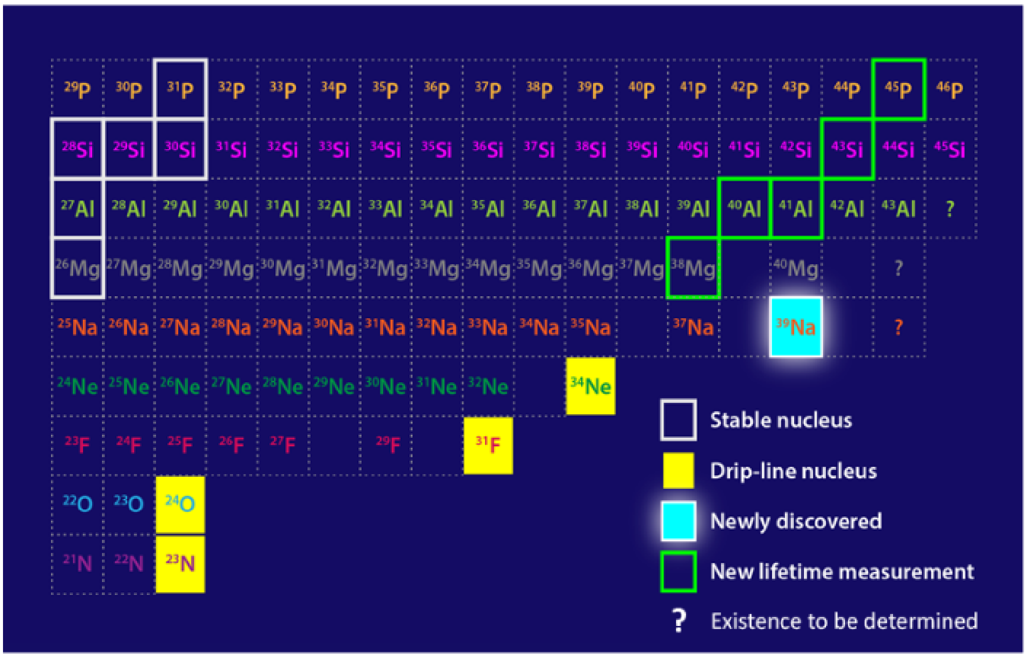

Figure 1.5: Nuclear landscape with ^{34}Ne as drip line nucleus and ^{39}Na as bound nucleus [2].

1.5 Neutron Drip-Line

As of now, the establishment of the neutron drip-line has only been achieved up to Z = 10, corresponding to the isotope ^{34}Ne [2, 3]. Fig.1.5 shows partial nuclear landscape around neutron drip-line close to ^{34}Ne [2]. Using RIBF, a team of international scientists observed ^{39}Na as a bound nucleus but no bound Ne nucleus has been observed above ^{34}Ne [3]. Though many loosely bound neutron-rich nuclei have been observed around A$\sim$ 100 region but existence of neutron drip line has been observed upto Ne nucleus. This limited progress can be attributed to the challenges posed by the remote location of the neutron drip-line, combined with the absence of a suitable reaction mechanism for accessing neutron drip-line nuclei with moderately high atomic numbers. We expect that significant advancements in the production and study of new neutron-rich isotopes, especially with the emergence of new radioactive beam facilities, it will be possible that our knowledge of the neutron drip-line will be expanded in near future. In natural processes, the successive rapid capture of neutrons during supernova explosions, known as the r-process, is responsible for generating highly neutron-rich nuclei. This mechanism primarily contributes to the production of 27 trans-iron isotopes [4]. However, the r-process is not expected to extend close to the neutron drip-line. Experimentally, the most critical information needed to define the path of nucleosynthesis includes the half-lives, neutron binding energies, and β-delayed neutron emission probabilities of neutron-rich isotopes and also capture rates. On the surface, it may seem that the study of neutron drip-line nuclei offers relatively limited potential. However, this pessimistic outlook was shattered by the discovery of a significantly expanded nuclear matter distribution within the nucleus ^{11}Li, achieved through groundbreaking nuclear reaction studies using fragmented radioactive beams at Berkeley [5]. In these studies, the exceptionally significant interaction cross section observed for ^{11}Li nuclei was attributed to the presence of a large matter radius. Subsequent research by Hansen and Jonson [6] introduced the fundamental theoretical model for this phenomenon, which is commonly referred to as the "neutron halo". According to their model, the substantial matter radius of ^{11}Li can be explained by the existence of a region characterized by nearly pure neutron matter, associated with the presence of two very loosely bound (S_{2n} = 0.31 MeV) $p_{3/2}$ valence neutrons. Since the initial discovery of the two-neutron halo in ^{11}Li, various other neutron halo nuclei have been identified, including examples of a one-neutron halo, such as ^{11}Be. In all of these cases, certain conditions appear to be prerequisites for the formation of a neutron halo. These conditions include an extremely low one or two neutron binding energy and a low orbital angular momentum, which collectively enable a significant portion of the wave function to extend to large distances. The study of the halo phenomenon continues to evolve with increasingly sophisticated experiments. This suggests that the exploration of neutron halo nuclei remains a vibrant and fertile domain for nuclear physics research, as highlighted in [7, 8].

1.6 Nuclei along the Proton Drip-Line

The proton drip line is not as easily found as the neutron drip line. Using an equivalent definition as for the neutron drip line,the proton drip line is located where the proton separation energy (or two-proton separation energy) crosses zero. Nuclei beyond the proton drip line are technically unbound and can therefore decay by proton emission. However, many nuclei, especially for elements of medium mass and above, do exist beyond the proton drip line as a result of the proton's charge(due to coulomb barrier). For the unbound proton (or protons) to be emitted, they have to tunnel through the Coulomb barrier, which is holding protons in the nucleus, leading to half-lives of the order of milliseconds up to seconds.

Proton halos The one unavoidable difference betweenthe proton and neutron drip-lines is that in the case of the proton drip-line the last bound particle experiences a potential energy barrier caused by its mutual long-range electrostatic interaction with all the core protons. This simple fact is responsible for the profound differences in phenomena at the proton and neutron drip-lines. It might be supposed that this distinction does not manifest itself until nuclei with moderately high atomic numbers (Z $>$ 20) are considered. This assumption seems reasonable since the locus of stable nuclei exactly follows the N = Z line up to ^{40}Ca. However, although the proton drip-line has been mapped extensively, no clear examples of proton halo nuclei have been discovered. Riisager has argued that because of the attenuating effect of the Coulomb barrier on the spatial extent of the proton wavefunction, the proton halo may only exist for loosely bound nuclei with Z$<$ 10 in either an s or a p state . It was initially thought that a prime candidate for a one-proton halo would be ^{8}B, which has a p $_{3/2}$ proton with a very low separation energy(0.14 MeV). Evidence supporting this theory includes a break-up experiment performed at GSI and the large quadrupole moment of ^{8}B compared to ^{8}Li. The other remaining candidate in this region is the nucleus ^{17}Ne, which has a low two-proton separation energy, S_{2p} = 0.95 MeV, which could produce a two-proton halo. Unlike the neutron drip line, pinpointing the location of the proton drip line is a more complex task. By using an equivalent definition to that used for the neutron drip line, the proton drip line is identified as the point where the proton separation energy (or two-proton separation energy) reaches zero. Nuclei located beyond the proton drip line are technically unbound and can potentially decay through proton emission. However, many nuclei, particularly for elements of medium mass and higher, do exist beyond the proton drip line, mainly due to the influence of the proton's electric charge, which results in the formation of a Coulomb barrier. For unbound protons (or protons), emitted from these nuclei, to escape, they must tunnel through the Coulomb barrier that retains protons within the nucleus. This tunneling process leads to relatively long half-lives, typically on the order of milliseconds up to seconds, as the Coulomb barrier presents a formidable obstacle to proton emission. In contrast to the neutron drip-line, there is an inherent distinction in the case of the proton drip-line. Here, the last bound particle encounters a potential energy barrier due to its long-range electrostatic interaction with all the core protons. This fundamental difference in phenomena at the proton and neutron drip-lines can be attributed to this unique characteristic. It may seem that this distinction becomes significant only when dealing with nuclei of moderately high atomic numbers ($Z > 20$). This assumption appears reasonable because the line of stable nuclei precisely follows the N = Z line up to ^{40}Ca. However, despite extensive mapping of the proton drip-line, no clear examples of proton halo nuclei have been discovered. Riisager [9] has proposed that the proton halo may only exist for loosely bound nuclei with $Z < 10$, residing in either an s or a p state. It was initially theorized that a prime nucleus for a one-proton halo could be ^{8}B, which possesses a p $_{3/2}$ proton with an exceptionally low separation energy of

0.14 MeV. Supporting evidence for this hypothesis includes a break-up experiment conducted at GSI [10] and the notable difference in quadrupole moments between ^{8}B and ^{8}Li [11]. Another nucleus in this region is ^{17}Ne, which has a low two-proton separation energy, $S_{2p} = 0.95$ MeV, indicating the potential for a two-proton halo to exist. Very recently, significant studies of proton drip line nuclei with higher mass region has been started.

1.7 Importance of study of the exotic nuclei

It is an important point regarding the applicability of magic numbers near the dripline, where the nuclear structure can deviate significantly from stable nuclei. The study of exotic nuclei, particularly those near the dripline, has indeed challenged our understanding of nuclear theory and called for potential modifications. The discovery of shell evolution and the breakdown of traditional magic numbers in these exotic nuclei has prompted theoretical researchers to explore new approaches and modifications to existing nuclear models [12]. The goal is to develop theories that can accurately describe the properties and behavior of these nuclei. To validate and refine these theoretical approaches, experimental data on the shell evolution and ground state properties of nuclei away from the beta stability line are crucial. Experimental studies at Radioactive Ion Beam facilities play a vital role in providing data on exotic nuclei, contributing to our understanding of their structure and properties. Therefore the study of nuclei at the limits of stability has recently become the central focus of nuclear structure research [13–15] that focuses on examining the properties of atomic nuclei that are located near or beyond the “drip lines.” The drip lines represent the boundaries of nuclear existence, where nuclei become unstable and undergo radioactive decay by losing nucleons (protons or neutrons). Investigating these nuclei provides valuable insights into the nature of nuclear interactions, particularly neutron-neutron (n-n) interactions. One crucial aspect studied near the drip lines is the nucleon separation energy. This energy represents the amount of energy required to remove a nucleon from a nucleus. As nuclei approach the drip lines, the nucleon separation energy decreases, and at the drip line itself, the nucleon separation energy becomes zero. This indicates that nucleons at the drip line are weakly bound and can easily detach from the nucleus. The nuclei found near the drip lines exhibit numerous interesting properties. One significant observation is the breakdown of traditional "magic numbers" in these exotic nuclei. Magic numbers are specific values of protons or neutrons that correspond to particularly stable configurations within the nucleus. However, in nuclei far from stability, the presence of additional or missing nucleons can lead to the breakdown of traditional magic numbers [16–20], challenging our understanding of nuclear structure physics. Furthermore, the nuclei near the drip lines can exhibit the emergence of new magic numbers [21–24], the presence of PIGMY resonance [25–28] which are different from those observed in stable nuclei. These new magic numbers are a consequence of the unique nuclear configurations found in these exotic systems. Experiments conducted on nuclei around the drip line also provide insights into exotic decay processes [29–31]. Before explaining more details of exotic decay, some preliminary of discussion on decay processes is presented below for completemess.

1.8 β^- Decay

In nuclear physics, β decay is a type of radioactive decay in which an atomic nucleus emits a beta particle (fast energetic electron or positron), transforming into an isobar of that nuclide. In case of β^- a neutron transforms it into a proton by the emission of an electron accompanied by an antineutrino. Neither the beta particle nor its associated (anti-neutrino) exist within the nucleus prior to beta decay, but are created in the decay process. By this process, unstable atoms obtain a more stable ratio of protons to neutrons. The probability of a nuclide decaying due to beta and other forms of decay is determined by its Q value. β decay is a consequence of the weak force, which is characterized by relatively lengthy decay times. Nucleons are composed of up quarks and down quarks, and the weak force allows a quark to change its flavour by emission of a W boson leading to creation of an electron/antineutrino or positron/neutrino pair. For example, a neutron, composed of two down quarks and an up quark, decays to a proton composed of a down quark and two up quarks. In electron capture, an inner atomic electron is captured by a proton in the nucleus, transforming it into a neutron, and an electron neutrino is released.

1.9 β^+Decay

Positron emission or β^+decay is a subtype of radioactive decay called β decay, in which a proton inside a nucleus is converted into a neutron while releasing a positron and an electron neutrino (ν_e). Positron emission is mediated by the weak force. Because positron emission decreases proton number relative to neutron number, positron decay happens typically in large "proton-rich" radionuclides. Positron decay results in nuclear transmutation, changing an atom of one chemical element into an atom of an element with an atomic number that is less by one unit.

1.10 Electron capture

Electron capture (K-electron capture, also K-capture, or L-electron capture, L-capture) is a process in which the proton-rich nucleus of absorbs an inner-shell atomic electron. The electrons are mainly from the K or L shells. This process changes a proton to a neutron within nucleus and it simultaneously emits an electron neutrino. Since this single emitted neutrino carries the total decay energy, it carries single characteristic energy. Thus due to emission of the neutrino, the daughter atom recoils with a single characteristic momentum. One or more characteristic X-ray photons are emitted when the nucleus captures an inner electron from the atom then an outer electron replaces the previous one. Electron capture sometimes also results in the Auger effect, where an electron is ejected from the atom's electron shell. If the Q value of β-decay is less than 1.022 MeV, positron emission is forbidden. Schemetic diagram of two types of electron capture is shown in Fig.1.6. Top of Fig 1.6 shows, the nucleus absorbs an electron. Lower right of Fig 1.6 shows the Auger effect.

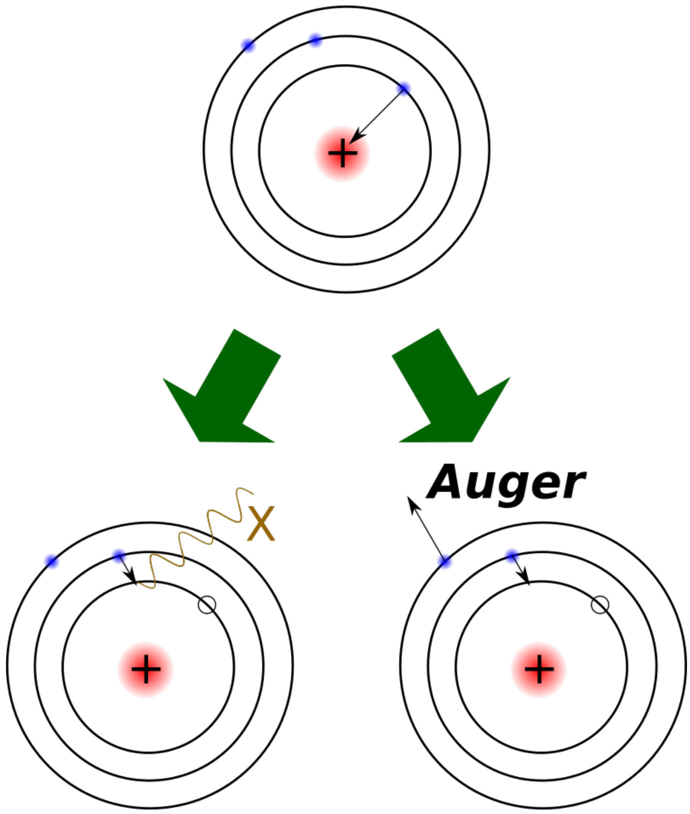

Figure 1.6: Electron capture.

1.11 Fermi theory of β decay

In 1934, Enrico Fermi developed a theory of β-decay based on Wolfgang Pauli hypothesis of the neutrino. Beta decay is a type of radioactive decay where a nucleus transforms into another nucleus by emitting a β-particle (electron or positron) and an antineutrino or neutrino. Fermi theory successfully explained the essential features of β-decay and paved the way for the understanding of weak interactions in nuclear physics.

The theory is based on the assumption that the interaction responsible for β-decay is weak compared to other nuclear interactions. In other words, the characteristic timescale of β-decay (half-lives typically of order seconds or longer) is much longer than the characteristic nuclear timescale.

Fermi Golden Rule is a general result in quantum mechanics that provides a way to calculate transition probabilities for quantum systems undergoing weak perturbations. In the context of β-decay, it allows us to calculate the transition probability for a nucleus in an initial state to transition to a final state through the weak interaction responsible for β-decay.

The basic expression of Fermi Golden Rule for a transition rate is given as follows

$$\lambda = \frac{2\pi}{\hbar}|V_{fi}|^2\rho(E_f), \tag{1.1}$$

where

$$V_{fi} = \int \psi_f^* V \psi_i dv, \tag{1.2}$$

The factor $\rho(E_f)$ is the density of the final states which can be written as dn/d(E_f), the number of final states (dn), in the energy interval dE_f. The ψ_f and ψ_i represents the final and initial states of the system respectively.

1.11.1 Allowed Decays

In the allowed decays, it is assumed that the electron and neutrino have been created at r = 0. Thus they cannot carry any orbital angular-momentum, and the only change in the angular momentum of the nucleus must result from the spins of the electron and neutrino. These two spins can be S = 1 or 0. If the spins are antiparallel, known as a Fermi decay then in the allowed approximation (l = 0), no change in the nuclear spin: $\Delta I = |I_i - I_f| = 0$ is expected. If the electron and neutrino spins are parallel, known as Gamow-Teller decay, a total angular momentum of 1 unit is carried and thus I_i is equal to $I_f + 1$. This is possible only if $\Delta I = 0$ or 1 (except for $I_i = 0$ and $I_f = 0$, in which case only the Fermi transition can contribute). If the electron and neutrino carry no orbital angular momentum, then the parities of the initial and final states must be identical since the parity associated with orbital angular momentum l is $(- 1)^l$. Thus following selection rules for allowed beta decay: $\Delta I = 0$,1 and $\Delta\pi$ (parity change) = no

1.11.2 Forbidden Decays

The "forbidden" decays are usually less probable than allowed ones. The frequent forbidden decay is when the initial and final states are with opposite parities. For the change in parity, the electron and neutrino must be emitted with an odd value of the l relative to the nucleus. Though it is less likely to have non-zero values of l relative to l= 0, and decays with l = 3,5,7,. . . are extremely unlikely, and we can for the moment consider only those forbidden decays with l = 1. These are called first-forbidden decays, and like the allowed decays they have Fermi types, with the electron and neutrino spins opposite (S = 0), and Gamow-Teller types, with the spins parallel (S = 1). The coupling of S = 0 with l = 1 for the Fermi decays gives total angular momentum of one unit carried by the beta decay, so that ΔI= 0 or 1. Coupling S = 1 with l = 1 for the Gamow-Teller decays gives 0, 1, or 2 units of total angular momentum, so that ΔI = 0, 1, or 2. Thus the selection rules for first-forbidden decays are ΔI = 0,1,2 and $\Delta\pi$ (parity change) = yes. Fig 1.7 shows the schematic diagram of Fermi and Gamow-Teller type β-transitions.

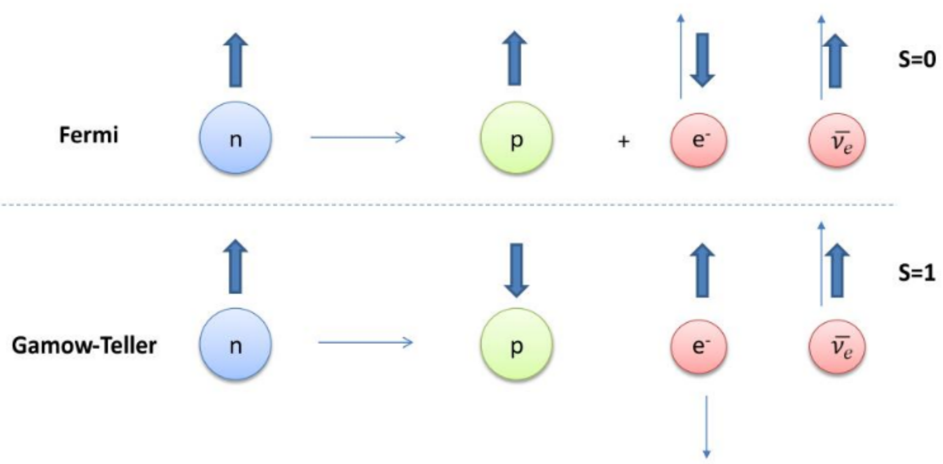

Figure 1.7: Schematic diagram of Fermi and Gamow-Teller type beta-transitions.

1.12 Delayed Proton emission

Proton emission is a rare type of radioactive-decay in the nuclei around proton-drip line. Proton emission can occur from high-lying excited states in a nucleus following a β-decay. This process is known as β-delayed proton emission. The rate of proton emission is governed by the nuclear, Coulomb, and centrifugal potentials of the nucleus. Half-life of proton emission is affected by the proton energy and its orbital angular momentum. The study of proton emission has aided the understanding of nuclear deformation, masses, and structure, and it is a pure example of quantum tunneling. Fig 1.8 shows the decay of a proton rich nucleus ${}^{A}X_{Z}$ populates excited states of a daughter nucleus ${}^{A}Y_{Z-1}$ by β emission or electron capture (EC). Those excited states that lie below the separation energy for protons(Sp) decay by γ emission towards the ground state of daughter ${}^{A}Y_{Z-1}$. For the higher excited states a competitive decay channel of proton emission and population to the grand-daughter ${}^{A-1}Q_{Z-2}$ exists.

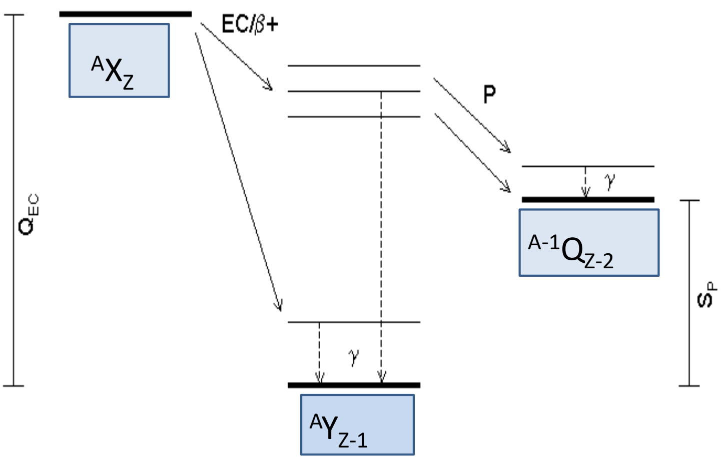

Figure 1.8: beta-delayed proton emission.

In present situation, ^{115}Cs undergoes β-decay to produce the daughter nucleus ^{115}Xe in excited state. After one proton emission from the excited states above proton threshold, the grand-daughter ^{114}I is produced, which is shown in Fig 1.9.

These decay processes around the drip-line nuclei can involve the emission of particles such as protons, neutrons, alpha particles, or other light nuclei, providing further evidence of the instability of these exotic nuclei.

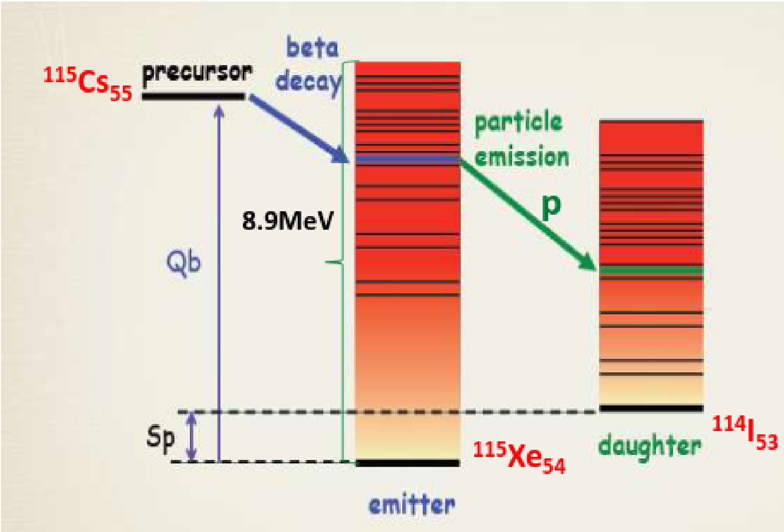

Figure 1.9: Schematic diagram of beta-delayed proton emission from ^{115}Cs.

In 1963 R. Barton, had reported the first positive identification of a β -delayed proton precursor, ^{25}Si, and the tentative identification of several others nearby [32]. At the time, its unique signature opened a window onto a new world of exotic nuclei: on-line isotope separation was not yet available to isolate newly produced nuclei, but a readily separable decay mode was a fine alternative. In the first two decades after its discovery, β-delayed proton decay was a rich source of spectroscopic information on nuclei far from stability [33], yielding everything from analog states and atomic masses to level densities and excited-state lifetimes in the femtosecond region. However, with the advent of more sophisticated methods for the production and isolation of exotic nuclei, the importance of beta-delayed protons as an identifier of new nuclei effectively disappeared. Fig.1.10 shows a compilation of observation of delayed proton at various mass regions near proton-drip line. It is clear that the shape of the delayed proton-spectrum is different corresponding to different regions. In that figure, it is clear more evidences are available at lower mass nuclei (A$\sim$ 20-40) and higher mass region (A>140). But experimental information around A$\sim$

100-120 is limited. In this thesis, exotic decay of ^{115}Cs has been studied.

Additionally, the study of nuclei near the drip lines has revealed the presence of cluster structures [34–36]. Cluster structure refers to the formation of small, self-contained clusters of nucleons within the nucleus. These clusters can consist of protons, neutrons, or both and have a distinct arrangement within the nucleus. The investigation of cluster structures contributes to our understanding of nuclear dynamics and the interplay between nucleons. Exploring the nuclear characteristics of doubly magic heavy nuclei near the proton drip-line offers valuable insights into the dynamic interplay between neutrons and protons at the outer limits of nuclear stability [37–39] . This investigation is particularly significant because in heavier nuclei with an equal number of neutrons and protons (N = Z), there is an augmentation of proton-neutron pairing interactions, leading to wider reduced α-decay widths [40]. These increased decay widths are indicative of the emergence of α-cluster formation [41, 42]. As a result, delving into the various decay modes of nuclei in the vicinity of ^{100}Sn is a valuable means of unraveling crucial nuclear properties at the brink of nuclear stability [43, 44]. Nuclei situated near the proton drip-line exhibit a notable distinction in binding energies between protons and neutrons. This substantial difference in binding energies leads to a high Q value for β-decay, enabling the excitation of states in the daughter nucleus above the particle threshold. Consequently, the exploration of the spectroscopic characteristics of these unbound states offers valuable insights into the nucleon-nucleon (n-n) interaction and its connection to the continuum.

Furthermore, the influence of the proton skin thickness on the decay of neutron-deficient nuclei demands further examination. The region encompassing nuclei with a mass of approximately A $\sim$ 100-120, close to the proton drip-line, is anticipated to be "island of cluster emitter" [34]. While there is evidence of heavy cluster emissions, such as ^{14}C, from nuclei like ^{222}Ra and ^{224}Ra [45, 46], observations regarding the emission of ^{12}C from^{114}Ba remain inconclusive [47–49], necessitating additional investigation in this mass range. Another intriguing facet of this mass region is the

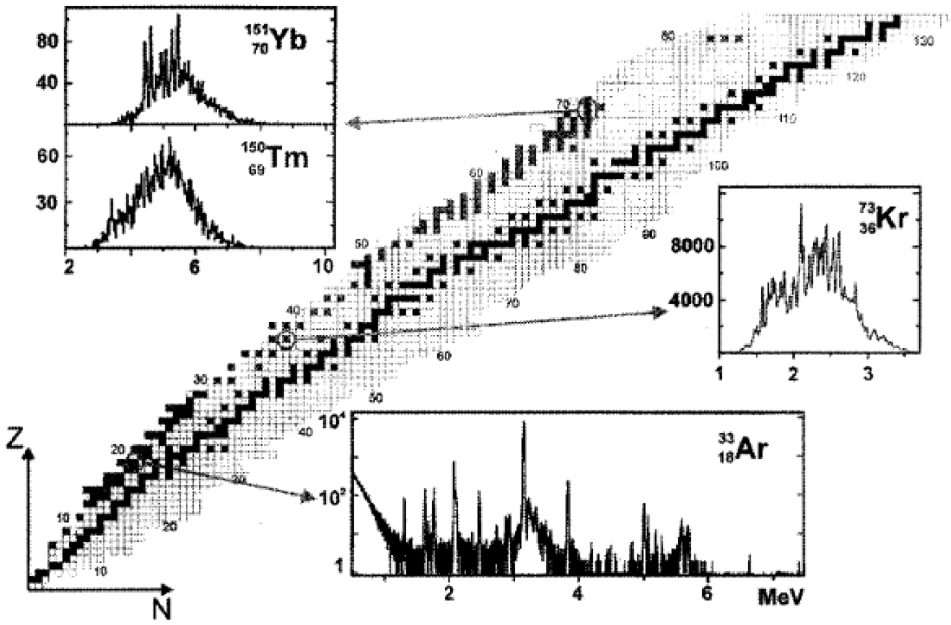

Figure 1.10: Delayed proton emission from nuclei at various mass region near proton drip-line [33].

rp-process, responsible for the synthesis of neutron-deficient nuclei near the proton drip-line [50, 53]. Fig.1.11 shows nuclear landscape and related nucleosynthesis process at that mass region. As evident from figure, the rp-process is responsible for synthesis of nuclei near proton drip line. The exact element with the highest mass produced by this process is still a topic of debate [51–53]. Limited experimental data on the exotic decay modes of these nuclei [54–57] are currently available, and further experimental studies are required to deepen our understanding. The primary challenges in comprehending this process primarily stem from uncertainties related to (p, γ) reaction rates. Due to experimental limitations, calculated reaction rates are mainly used. Hence, understanding the level structure above the proton threshold of nuclei in this vicinity becomes crucial in constraining these reaction rates and their strengths. However, it is essential to note that only a limited amount of experimental data is currently available [54–57], underscoring the need for further experimental investigations to deepen our understanding.

The specific nucleus of interest is ^{115}Cs, which possesses characteristics of being both proton and alpha unbound [1]. Previously, only the delayed proton branching ratio and lifetime of ^{115}Cs were reported [55]. This study represents the first comprehensive exploration of the decay modes of ^{115}Cs. Following electron capture and/or β^+ decay, the excited states of the daughter nucleus, ^{115}Xe, are populated above the thresholds of one and two protons or alpha clusters, among others. Consequently, potential decay channels include $\beta\gamma$, βp, βpγ, β2p, β2pγ, and $\beta\alpha$, etc. The nucleus's lifetime was determined from the time distribution of delayed proton events [56], and this value was consistent with a previously reported one [55]. In this article, a comprehensive data analysis is presented, which includes information about delayed proton and alpha branching ratios, as well as several reconstructed proton and alpha unbound excited states of ^{115}Xe, marking the first such report in the literature [58].

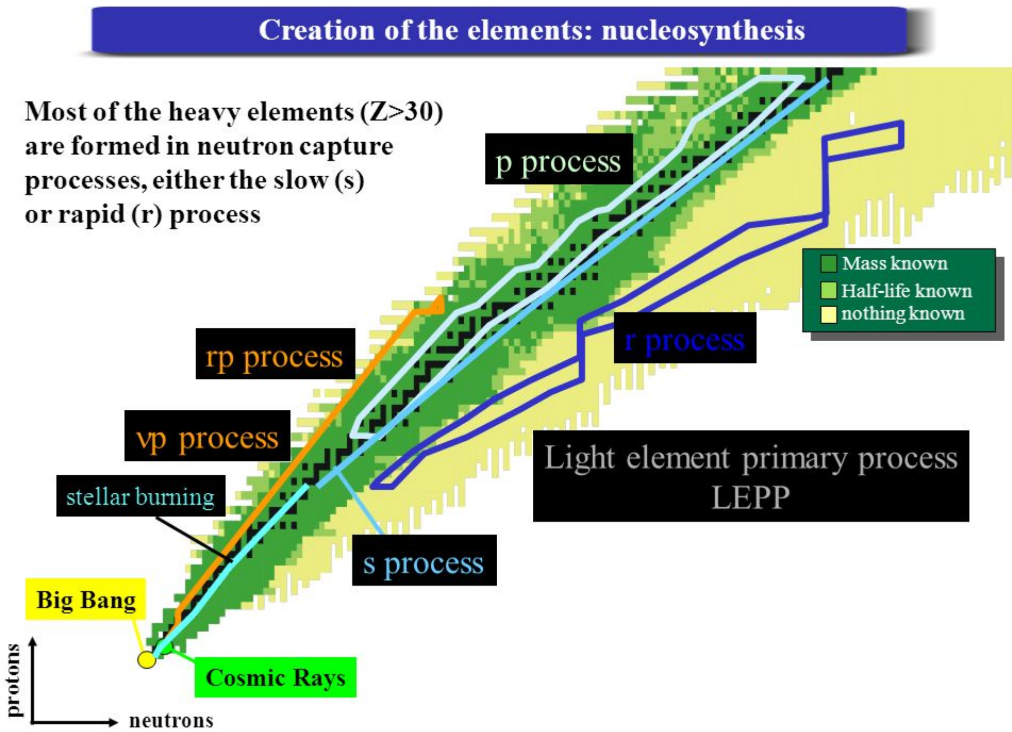

Figure 1.11: Nuclear Lanscape and various nucleosynthesis processes [59].

Chapter 2

Radioactive Ion Beam

In this chapter of the thesis a brief description on Radioactive Ion Beam (RIB) facilities and their production techniques are discussed. Here I will discuss about both ISOL facility and In-flight facility. As my experiment is based on ISOL facility, I shall discuss details of ISOLDE technique.

2.1 Radioactive Ion Beam Facilities

The idea and realization of Radioactive Ion Beam (RIB) has changed the face of study of the nuclear science since around three decades ago. Scientists and physicists have offered large amounts of time and brains into the production and scientific exploitation of RIB. New ways, methods and utilizations have been identified and applied by several groups in Asia, U.S.A. and Europe. There are two broadly classified methods to produce beams of the exotic (unstable) nuclei, and they are Isotope-Separation-OnLine (ISOL) and In-Flight Separation (IFS). The different properties of the beams from these two techniques make them complementary to each other. Different types of experiments have been performed by utilizing the ISOL and IFS methods of RIB [60]. The main aim of any RIB facility is to deliver intense and pure beams with good ion-optics parameters and having various energy ranges ranging from rest to the highest energies of few MeV/nucleon. Thus, the entire production process must be very fast, efficient and selective. The main difficulties encountered are the low production cross-sections for the nuclei of interest, overwhelming production of unwanted nuclei, very short half-lives and the targets that have to cope with very intense beams.

2.1.1 Isotope Separation OnLine (ISOL)

The “ISOL” is an abbreviation for Isotope Separation OnLine. In the general ISOL scheme, a primary stable beam is implanted on a thick target, like UC_2. The stable beam is usually of heavy ions, protons or thermal neutrons. Until now, largest beam intensity has been achieved by using high energy protons at ISOLDE, CERN from PS Booster [61]. The high-energy protons synthesize radioactive nuclei through spallation, fission and target fragmentation reactions. The beam stops within the thick target, and products of the reaction are extracted using radiochemical techniques. The extracted atoms are then ionized in an ion source which can either be in the target or after the transfer line. The properties of the elements like ionization potential, diffusion constant and also the temperature of the target play a vital role here. Hence some isotopes will be more difficult to be produced compared to others. Enhancements and developments are ongoing regarding the laser ion source and target geometries, porosities to synthesize a wider range of exotic isotopes. A magnetic spectrometer separates the beam after extraction from the ion source with which an experiment is concerned. The now purified beam is sent to the experimental hall. The post-acceleration of the beams is now being pursued. Depending on selectivity of target and ion sources, the beams are often very pure and the separator setup is not as complicated as an IFS facility. The beams from ISOL facilities usually have higher intensities and their quality is also superior than those of IFS facilities. Low-energy beams can be implanted into foils and the decay properties of these nuclei can be studied. However, this method requires large order of time to separate and perform measurements after the reaction at the target. Nuclei with very low life time are not suitable to study by this technique. The life time of isotopes to be studied should be in the order of milliseconds, at least. This "ISOL" method is now successfully used in many research institute and laboratories for low-energy experiments (a few keV to few MeV/nucleon). ISOLDE CERN, Switzerland is providing an excellent facility for performing experiments with low energy beam utilizes this technique to produce RIB [61]. Others laboratories are Holifield RIB Facility at Oak Ridge, USA, Louvain-la-Neuve, Belgium are also using the "ISOL" technique for the production of RIB. Present thesis is an effort in that direction and the experiment was performed at ISOLDE, CERN, Switzerland using IS545 setup.

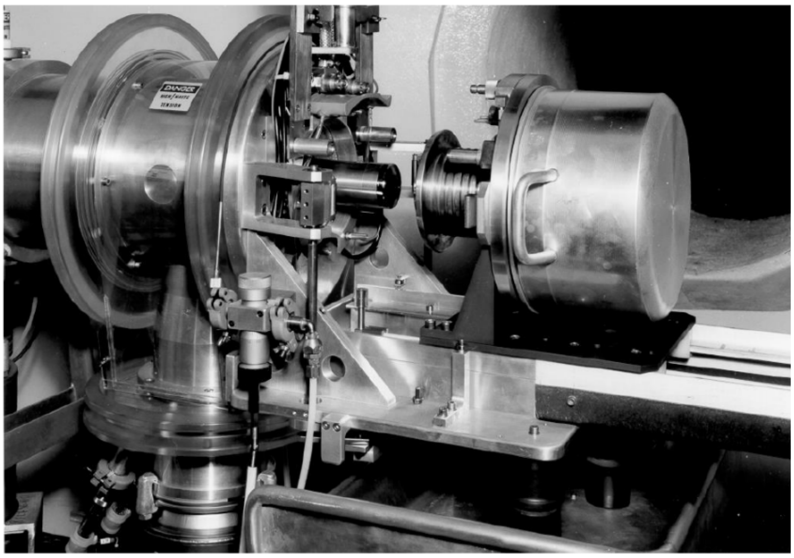

Figure 2.1: One of the first target and ion-source systems used in the ISOLDE facility of CERN [61].

2.1.2 InFlight Separation (IFS)

The "IFS" is the abbreviation for In-Flight Separation. In-flight techniques are used in many radioactive ion beam (RIB) laboratories such that the the National Superconducting Cyclotron Laboratory at Michigan State University; GSI Helmholtzzentrum für Schwerionenforschung, Darmstadt; the SPIRAL facility at GANIL; the TRIUMF, Canada; the Flerov Laboratory at Dubna, the RIKEN; etc. In this process a heavy ion-beam at energies 100 − 1000A MeV is collided against a target made of a material with optimal thickness required for production of required isotopes. Usually, it corresponds to the beam suffering an energy loss of only a few percent. The projectile reacts with the target nuclei, and the fragments produced continue with nearly same energy as the primary beam. Several reaction channels are simultaneously open in this case. The most widely used favourable reaction for production of high energy exotic nuclear beam, is projectile fragmentation. After the target area, there is a magnetic separator system which selects the required isotopes from the different types of nuclei produced in the target- projectile reaction. The separator comprises dipole magnets that select ions by using their momentum to charge ratios. In the IFS technique, it is possible for light ions to be completely stripped off all electrons. A degrader is also used for increasing isotopic resolution and getting the cleanest beam possible. Quadrupole and higher order magnets are sometimes used to focus the beam at different ion-optical planes in the separator. A major advantage of the IFS method is that the limit on lifetime of the nuclei is constrained only by flight-path through the spectrometer and the speed of the beam. Typically, nuclei with lifetimes lower than milliseconds region can be studied using IFS method. This enables identification of extremely exotic species on the nuclear landscape. However, high energies and emittance of secondary beams are not suitable for all experiment. IFS facilities have sometimes been extended for the storage rings with coolers, where the energy and its spread for the ion beams are lowered by electron cooling. The concept of fragment-separator in IFS has been pioneered with relativistic heavy-ion beams at Berkeley using beam-line elements. The In-Flight technique was pioneered in 1979 at the Bevalac facility in Berkeley, CA, USA by using an ^{40}Ar beam at 213 MeV/nucleon to bombard a carbon target. The projectile fragments were detected at several angles and identified using thick Si detectors.

2.1.3 Similarities and differences between ISOL and In-flight techniques

The ISOL method uses light ion beams (or neutrons, photons) which induce fragmentation, spallation and/or fission in a thick high-temperature target. These processes are shown in the below Fig 2.2. Afterwards the resulting nuclei diffuse out of the target, are ionized using various sources and separated using a mass separator. The beams are initially accelerated at a few tens of kV potential but can be further post accelerated using special techniques.

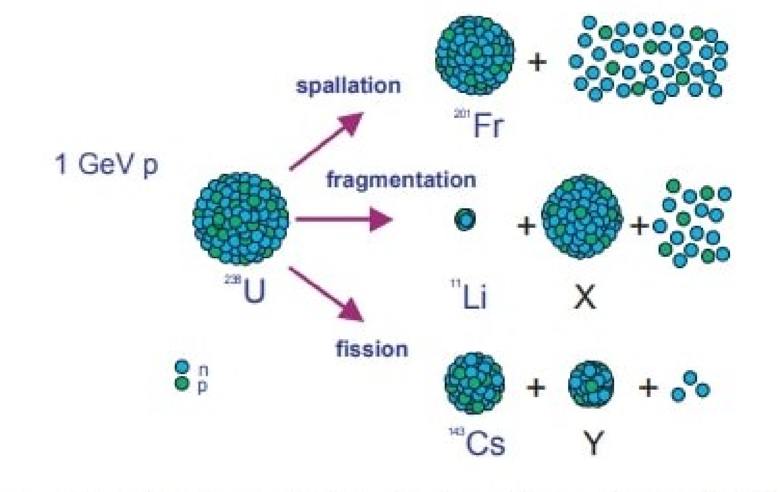

Figure 2.2: Schematic diagram showing nuclear reactions involved in the production of RIB [61].

The In-Flight method makes use of highly energetic heavy ion beams that produce fragmentation (in the case of high mass projectiles) or fusion-evaporation (for lighter projectiles) reactions in a thin target. The ionized energetic nuclei of various atom recoil out of the target and are sent to a fragment separator. Afterwards the separated fragments can be either sent directly to the experimental hall, to a gas catcher or storage ring.

The main differences between the two techniques are represented by the primary beam, the target thickness and the separation stage. As a consequence, the reaction products in the ISOL method are in most of the cases stopped while in the In Flight case, the projectile is fragmented by traversing the target and the ejectiles continue with almost the same energy that the incoming beam, making the time losses between production of the ejectile and magnetic separation negligible. The resulting beams will have different energies that range from rest up to roughly 10 MeV/nucleon (ISOL) and 1 GeV/nucleon (In-flight). Also the extraction time of ISOL beams is quite slow (ms - s) compared to the In-flight which translates directly into a lower efficiency for the ISOL technique. Nevertheless this is compensated by the good beam quality and high resolution of the mass separator. The ISOL and In-flight techniques for the production of RIB is shown in Fig 2.3.

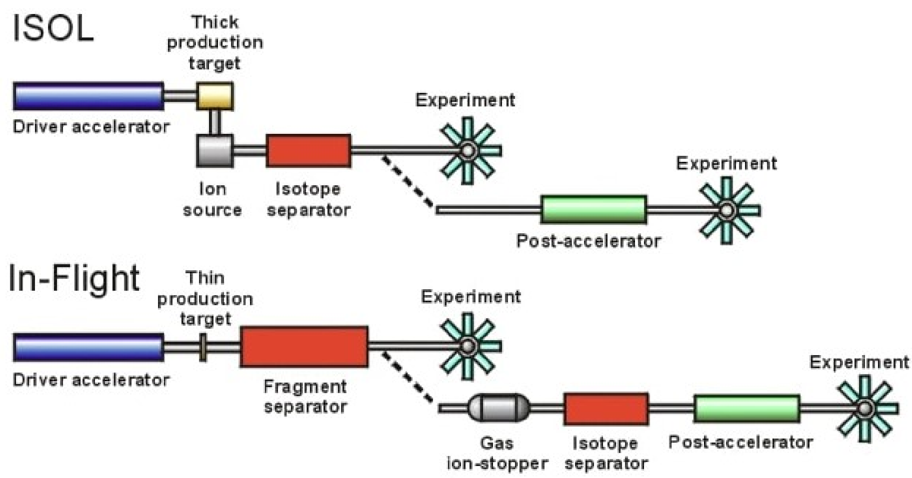

Figure 2.3: ISOL and In-flight techniques for the production of RIB.

2.1.4 Main Facilities

At the present moment there are three main ISOL-based facilities offering a large choice of beams: ISOLDE, CERN and SPIRAL, GANIL in Europe and TRIUMF in Canada. ISOLDE is the oldest one, pioneering the ISOL technique and is located at CERN, Geneva, Switzerland.

Accelerator complexes of high-energy heavy ions (usually cyclotrons) offer the choice of creating RIBs from projectile fragmentation if the primary target is coupled to a suitable fragment separator device. The major In-flight high-energy heavy ion facilities in operation since the year 1990, MSU-NSCL, GANIL, RIKEN and GSI, have been operating at an increasing pace being dedicated to RIB production due to the broad scientific opportunities

2.1.5 Beam intensity

The decisive characteristics for any RIB facility is the intensity and purity of the beams it delivers. The release and transport time through the different steps of the desired atomic elements will influence considerably the overall production efficiency especially if it is comparable to the decay half-life of the radioactive isotopes that will be extracted. To facilitate a systematic description of each production stage, it is desired to treat separately the decay efficiency ϵ_{decay}. Therefore, the other factors will be considered for stable isotopes. The production of the desired isotopes in the target, P, is given by the following formula: P = $\phi \cdot \sigma \cdot$N where ϕ is the flux of incident particles, σ the production cross-section and N the total number of atoms in the target which are exposed to the incident beam, proportional to the primary beam size and target density. The yield formula, specific for an ISOL facility, can be written as: i = $\epsilon_{target} \cdot \epsilon_{ion} \cdot \epsilon_{sep} \cdot \epsilon_{transp} \cdot \epsilon_{postacc} \cdot \epsilon_{decay}$

The intensity of the beam provided to the end-user is given not only by the production in the target but several other factors which define the efficiency of extraction from the target, ϵ_{target} , ionization ϵ_{ion} , separation ϵ_{sep} , transport ϵ_{transp} and the decay of the radioactive isotopes during the entire process. The two parameters, ϵ_{transp} and ϵ_{sep} are ideally close to unity but in realistic cases they usually range around 90%. Another important parameter is represented by the selectivity of the separation. A less selective method will yield a higher isobaric background and more statistics will be required in order to discriminate the desired isotope.

2.1.6 The Isotope Separation On-Line Facility of CERN

ISOLDE uses thick targets, the most used type being the uranium carbide which are irradiated with a pulsed beam of protons having an average intensity of 2 μA and being accelerated at 1.4 GeV by the Proton Synchrotron Booster (PSB) of the CERN accelerator complex. In 2016, ISOLDE received 61% of the total number of protons delivered to all CERN experiments, being by far the main user of the proton beam. The protons initiate reactions such as spallation, fragmentation and fission in the heated target and then the exotic isotopes diffuse out of it through a transfer line connected to an ion source. Plasma, hot-cavity or laser ion sources are used to ionize the radioactive ion beams. These beams can be delivered directly to temporary or fixed experimental setups after being accelerated using a 30-60 kV accelerating potential and separated using the General Purpose Separator (GPS) or the High Resolution Separator (HRS). There is also the possibility of accelerating the beam with a linear accelerator up to 3.1 MeV/nucleon. This is done by the REX-ISOLDE post-accelerator system. Fig 2.4 shows the schematic diagram of ISOLDE facility at CERN.

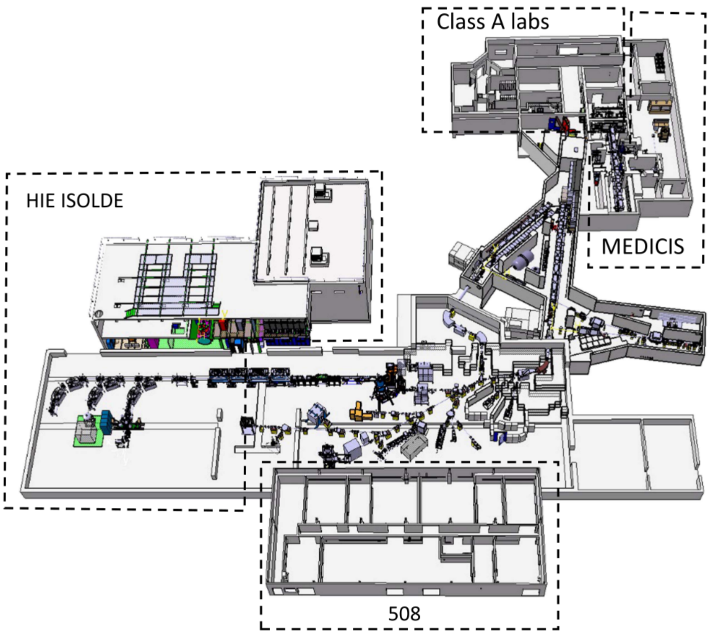

Figure 2.4: ISOLDE facility at CERN.

2.2 Target development

In ISOL (Isotope Separation On-Line) facilities, one of the main challenges is to separate the small number of nuclei produced in the target from the vast number of target atoms. This is typically on the order of 10^{12} nuclei per second compared to approximately 10^{23} target atoms. The goal is to transfer these separated nuclei to the ion source for further manipulation and analysis. To achieve this separation, the target material is heated to a sufficiently high temperature. At this elevated temperature, the nuclei of interest become more volatile compared to the target and target holder, allowing them to be released through diffusion and desorption processes. By carefully controlling the temperature, the flow of material can be kept low enough to prevent overwhelming the ion source, which could result in reduced efficiency. In the ISOLDE (Isotope Separator On-Line Detector) facility, the target and ion source systems have been extensively studied to determine the overall delay of the system. The time-dependent production of radioactive ions can be assessed by taking advantage of the pulsed structure of the proton beam used in the facility. The proton beam is typically structured as short pulses, such as a 2.4 μs long proton bunch, containing around 3×10^{13} protons. These pulses are delivered at regular intervals, typically every 1.2 seconds. By analyzing the production of radioactive ions as a function of time after the impact of the proton beam, researchers can gather valuable information about the dynamics of the system and optimize the experimental conditions. This allows them to understand the behavior of the target material and make adjustments to maximize the yields of the desired elements while maintaining the efficiency of the ion source.

2.3 Ion sources

2.3.1 Hot-cavity Ion Sources

The hot-cavity approach is a simple and commonly used design for ion sources. It relies on a tungsten cavity or tube that is heated to temperatures exceeding 2000°C.

The purpose of this high temperature is to enable high ionization efficiencies for elements with low ionization potentials. When the target material is heated to such high temperatures, the thermal energy provided is sufficient to liberate electrons from the atoms, creating a plasma-like environment. This plasma consists of both electrons and positively charged ions. The high temperature also increases the likelihood of collisions between ions and electrons, leading to ionization of the atoms present in the cavity. The hot-cavity ion source exhibits a high degree of selectivity for specific elements. This selectivity arises from the fact that elements with low ionization potentials are more easily ionized at the elevated temperatures provided by the tungsten cavity. This means that elements with lower ionization potentials have higher ionization efficiencies in this type of ion source. In some cases, efforts are made to create negative ion beams using the hot-cavity approach through a process called surface ionization. Surface ionization involves the preferential ionization of atoms on the surface of the cavity or tube. This technique aims to optimize the reduction of positively ionized contaminants in specific scenarios where negative ions are desired. Overall, the hot-cavity ion source offers a relatively simple design that can provide efficient ionization for elements with low ionization potentials. It allows for a certain degree of selectivity and, in specific cases, negative ion beams can be generated to minimize contamination from positively ionized elements.

2.3.2 Plasma Ion Sources

The forced-electron beam induced arc-discharge (FEBIAD) ion source is indeed widely used and highly successful in various applications. It operates on the principle of extracting electrons from a heated cathode and accelerating them into a low-pressure plasma. This accelerated electron beam ionizes the atoms or molecules in the plasma, resulting in the generation of ions. One of the key advantages of the FEBIAD ion source is its high efficiency, with efficiencies of up to 50% achievable. This means that a significant proportion of the extracted atoms or molecules can be ionized, resulting in a high ion beam current. At ISOLDE, a specific ion source based on the FEBIAD-type design is utilized. This ion source is connected to the target through a transfer tube. The temperature of the transfer tube can be adjusted to facilitate the selective adsorption of isotopes of less volatile elements onto its walls. This allows for the separation and retention of these isotopes, while isotopes from gaseous elements or gaseous molecules can pass through the transfer tube and reach the ion source. By employing this approach, a high degree of chemical selectivity can be achieved. The less volatile isotopes can be selectively adsorbed, while gaseous elements or molecules can bypass this adsorption and proceed to the ion source. This selective process enables the production of pure beams of noble gas isotopes, further enhancing the purity and specificity of the ion beam. Overall, the FEBIAD ion source, coupled with a temperature-adjustable transfer tube, provides a highly efficient and chemically selective method for generating pure beams of noble gas isotopes at ISOLDE.

2.3.3 Laser Ion Sources

Laser ionization has been implemented in ISOL systems through two different methods: gas cell and hot cavity. In the gas cell approach, laser ionization is employed to ionize atoms within a gas-filled cell. The atoms are stored in a gaseous phase and can be maintained in their metastable or ground states between laser pulses. This method allows for precise control over the ionization process and enables efficient production of ion beams. The hot cavity approach also utilizes laser ionization but within a heated cavity or tube. Similar to the gas cell method, atoms are ionized using laser radiation. The high temperatures of the cavity ensure that the released atoms are in a gaseous phase and can be stored in their metastable or ground states until they are extracted as ions. The Resonance Ionization Laser Ion Source (RILIS) is a specific type of laser ion source used at ISOLDE. It is designed to achieve chemically selective ionization through resonant excitation of atomic transitions using adjustable laser radiation. RILIS has been in use at ISOLDE since 1994 and has played a crucial role in the production of radioactive beams. The RILIS system offers significant advantages, which is why approximately 50% of all running experiments at ISOLDE rely on its capabilities. It enhances the production rate of specific isotopes by providing efficient and selective ionization. With RILIS, a high degree of isobar-free isotope selectivity can be achieved, meaning that the ion beams produced are largely free from unwanted isobaric contaminants. In summary, laser ionization in both gas cell and hot cavity configurations has been successfully implemented at ISOL facilities like ISOLDE. The Resonance Ionization Laser Ion Source (RILIS) stands out as a chemically selective ion source that has greatly contributed to the production of radioactive beams since its introduction, offering high isotope selectivity and improved production rates. Fig 2.5. Shows the periodic table of all the elements where different colours represents different methods of production of ion sources (e.g surface ionization, plasma ionization etc.). In our experiment surface ionization technique has been used.

Figure 2.5: Periodic table showing the optimal extraction method of each chemical element, at ISOLDE, CERN.

Chapter 3

Experimental-Setup

In chapter II, I have discussed about RIB facilities. Here in this chapter I shall present the details experimental setup for performing the experiment (IS545). I shall discuss about the Clover detectors, Double Sided Silicon Strip Detector(DSSD) and PAD detectors.

The experiment was performed at ISOLDE, CERN. The pulses of 1.4 GeV protons from Proton Synchronous (PS) Booster were directed at a Lanthanum Carbide target and unstable Cs isotopes were produced along with other nuclei via fragmentation and spallation. The radioactive nuclei were ionized and directed to the mass separator, General Purpose Mass spectrometer (GPS). The nucleus, ^{115}Cs was transferred to the IDS setup [61] at experimental hall and implanted on a 20μg/cm^2carbon target. The IDS setup consisted of five DSSDs (Double Sided Silicon Strip Detectors), four PAD detectors behind the DSSD (vertical ones), functioning as ΔE-E telescopes. Those DSSDs were of different thicknesses. Thin DSSDs (thickness 65 μm and 67μm) can fully stop low energy protons ($<$ 2.5 MeV), α ($<$9.6 MeV) and heavier clusters (for ^{12}C $<$ 51 MeV). The thick DSSD2 (525μm) can fully stop high energy protons ($<$ 8.4 MeV), while a fifth thick horizontal DSSD5 (1000 μm) mainly was used for detection of β radiation. The PADs were used for detection of β particles. The solid angle coverage of DSSD1, DSSD2, DSSD4, DSSD5, DSSD6 were 7.3%, 8.8%, 8.8%, 14.8%, 6.1% of 4π respectively. Four clover detectors were placed around the chamber for γ-ray detection. Fig 3.1 shows schematic diagram of the experimental setup for performing experiment IS545 at ISOLDE, CERN. Fig 3.2 shows the experimental setup during the experiment IS545 at ISOLDE, CERN.

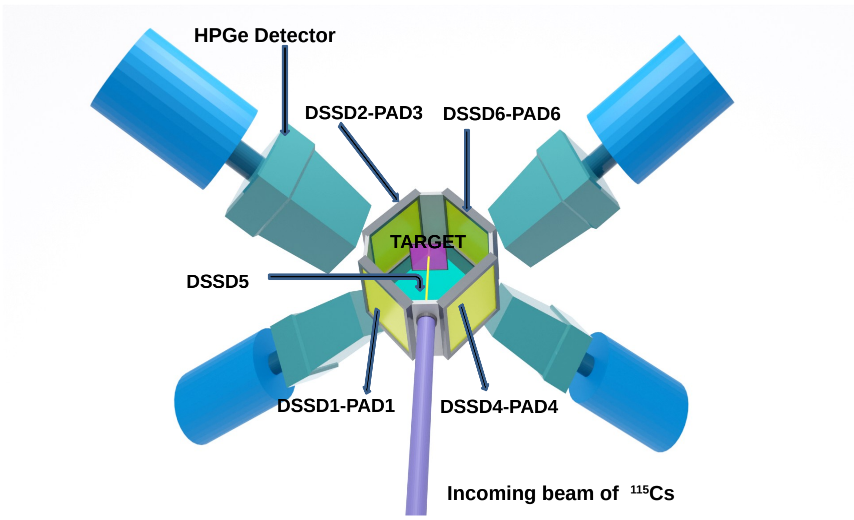

Figure 3.1: Schematic diagram of the Experimental setup.

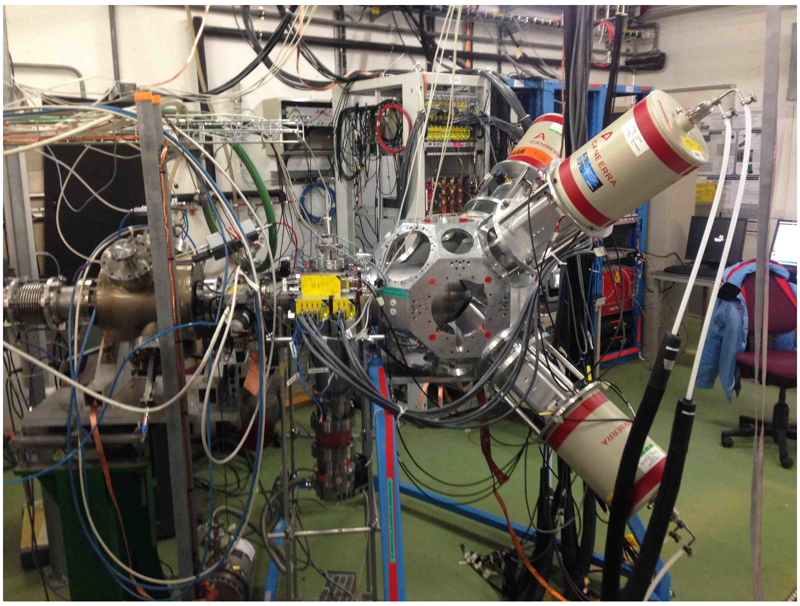

Figure 3.2: Experimental setup during the experiment IS545 at ISOLDE, CERN.

3.1 Clover detectors

Germanium detectors, specifically High Purity Germanium (HPGe) detectors, are commonly used in nuclear physics and industry for detecting gamma rays. They offer several advantages for gamma ray detection due to their unique characteristics. One important advantage of Germanium detectors is their high atomic number (Z), which increases the effective cross-section of the photoelectric effect. This means that gamma rays interacting with Germanium have a higher probability of undergoing the photoelectric effect, resulting in efficient detection.

Another significant characteristic of Germanium detectors is their excellent energy resolution for gamma radiation. It requires very little energy to create electron-hole pairs in Germanium when gamma rays interact with the material. This allows for precise measurement and identification of the energy of the detected gamma rays.

To maintain the high energy resolution, Germanium detectors need to be cooled to reduce noise. Cooling the detectors helps to minimize thermal fluctuations and improves the signal-to-noise ratio, leading to better energy resolution.

In experiments such as IS545, where the excited levels of a nucleus are being characterized, especially those just above the proton separation energy, Germanium detectors are particularly useful. They provide detailed information about the gamma de-excitation process in addition to the detection of charged particles. The combination of Germanium detectors with other detectors like the DSSD (Double-Sided Silicon Strip Detector) allows for proton-gamma coincidences, enabling comprehensive studies of the nuclear reactions and properties.

Segmented HPGe detectors, known as clover detectors due to their four-crystal cloverleaf shape, are commonly used in these experiments which is shown in Fig 3.3. Unlike silicon detectors that have segmented bands, the segmentation in HPGe detectors is achieved through external and internal contacts of the crystals. The substrate of segmented HPGe detectors is of n-type, similar to silicon detectors.

Although Germanium detectors are larger in size and have varied shapes compared to DSSD or PAD, their geometry is designed to accommodate the thickness required for gamma rays to deposit all their energy. The larger size also affects the voltage applied to the space charge zone. In germanium detectors, several thousand bias voltage is applied to increase depletion region.

In summary, Germanium detectors, particularly segmented HPGe detectors, are widely used in nuclear physics and industry for detecting gamma rays. They offer high energy resolution and are essential for characterizing excited nuclear levels and performing proton-gamma coincident studies. Cooling is necessary to maintain their excellent performance, and their geometry and voltage requirements differ from other types of detectors due to the unique properties of gamma radiation.

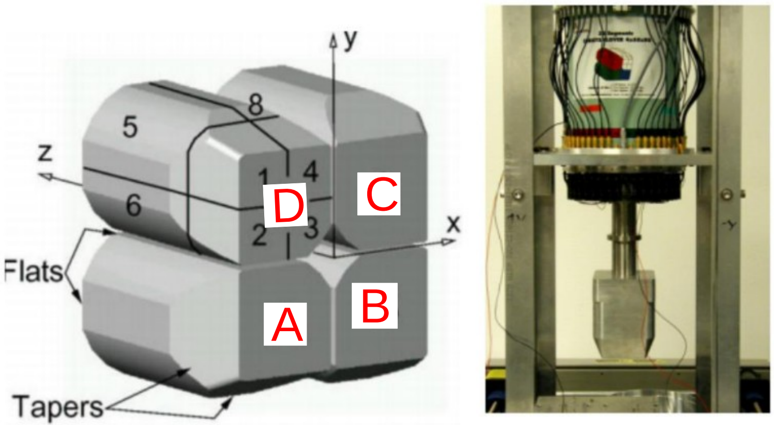

Figure 3.3: Left side: Schematic diagram of Clover detector. Right side: HPGe Clover detector used in this expriment IS545 at ISOLDE.

The segmented configuration of Germanium detectors, is utilized to enhance the photopeak efficiency through a technique called add-back. This method improves the Photopeak/Compton ratio by combining Compton events from different crystals and reconstructing the total energy of the incident radiation. By determining which crystals the gamma ray deposits energy in, all the signals can be added together to reconstruct the initial energy of the incident radiation. The advantage of this approach is that the add-back efficiency is higher than the sum of the individual crystal efficiencies.

The add-back technique is particularly valuable for high-energy gamma rays (above 1 MeV) and situations with limited statistics in the measurement. Arrays or sets of multiple segmented Germanium detectors are constructed to increase the geometric efficiency, compensating for the low intrinsic efficiency of individual detectors. The combination of multiple detectors allows for a higher probability of detecting the gamma ray and improves the overall efficiency of the system.

Segmented Germanium detectors also offer the advantage of reducing Doppler broadening. Doppler broadening occurs when gamma ray emission originates from a moving nucleus, resulting in scattering in velocity and angle, which can significantly degrade the energy resolution. However, by reducing the solid opening angle and dividing the Germanium volume into segmented regions, the resolution can be restored in the detector. The segmentation effectively minimizes the effects of Doppler broadening and improves the accuracy of energy measurements.

In our experiment, there are four HPGe detectors, each segmented into four crystals, surrounding the implantation/detection chamber which is shown in Fig 3.4. This configuration allows for efficient add-back of Compton events and enhances the overall photopeak efficiency. The distance of these detectors from the implantation point is about 20 cm. Additionally, the segmentation helps in reducing Doppler broadening and maintaining good resolution in the detection of gamma rays.

3.2 Silicon Detectors

DSSDs (Double Side Silicon Strip Detector) are silicon semiconductor detectors commonly used in nuclear physics for the detection of charged particles. These detectors offer several advantages for this purpose.

One key advantage of DSSDs is their low atomic number (Z), which means they have a high critical energy. The critical energy is the energy at which the loss of energy through ionization is equal to the loss through radiation. In DSSDs, the critical energy is high, which helps to avoid the problematic braking radiation(bremsstrahlung) that can interfere with the detection of charged particles.

Another important feature of DSSDs is their high segmentation. The detector

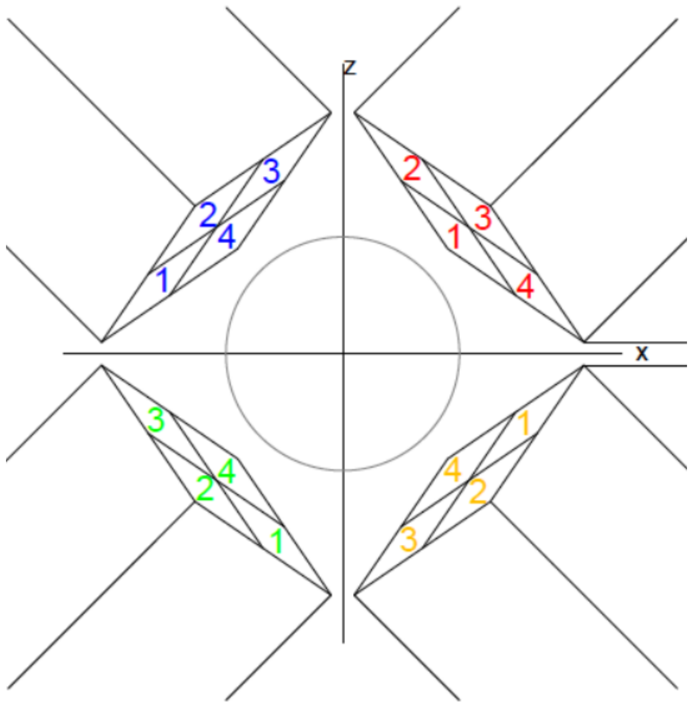

Figure 3.4: Orientation of the clover detectors. Each detector, made up of four crystals, is marked with a different color. In this case, the beam comes from the direction of the viewer. The distance of these detectors from the implantation point is about 20 cm.

is divided into strips, with two types of contacts perpendicular to each other on both sides of the silicon substrate. These contacts are either p-type or n-type bands, depending on the type of doping used (n^+ or p^+). To prevent the connection between these bands and to ensure individual signals for each strip, an insulator such as silicon dioxide is placed between them. This region, known as the interstrip, is not active for particle detection.

The segmentation of DSSDs allows for the detection of multiple charged particles emitted simultaneously at different angles within the detector's angular coverage. This capability is crucial for studying excited states of light nuclei that involve the simultaneous emission of several particles and require knowledge of their angular correlations. The granularity provided by the strip segmentation enables the determination of the 2D position of the detected particles with high precision. By analyzing the angular distributions of the emitted charged particles, researchers can characterize the nuclear states from which they originated.

DSSDs also offer intrinsic detection efficiency close to 100% and high energy resolution for charged particles. These properties make them well-suited for experiments like the IS545, where the objective is to study disintegration channels involving the emission of one or two protons in coincidence over a wide range of energies, with the angular distribution playing a crucial role.

In the case of the n-type bands in DSSDs, additional measures are taken to ensure proper isolation. A p^+ zone is introduced to prevent charge accumulation at the Si-SiO_2 interface, helping to maintain the individual signal for each strip. The schematic diagram of Double Sided Silicon Strip Detector is shown in Fig 3.5.

Overall, DSSDs with their segmentation, low Z, high detection efficiency, and energy resolution are valuable tools in nuclear physics experiments for studying charged particle emission, angular distributions, and excited nuclear states.

In DSSDs, the substrate is typically n-type, allowing for the extension of the depletion zone from the p^+ doped bands towards the interior of the silicon substrate when an reverse bias is applied. When radiation interacts with this sensitive area, electron-hole pairs are created. These charge carriers are collected by the anode and the cathode, resulting in two types of signals—one from the electrons and the other from the holes. Although they originate from the same event, the electrons and holes have different properties, leading to differences in the signals obtained from each side of the detector. One side may have better resolution than the other due to variations in charge carrier properties and other factors such as noise.

To facilitate the free flow of electrons and holes for the generation of electrical signals, ohmic contacts or metal-semiconductor junctions are employed. Aluminum is commonly used as the metal, either in the form of a sheet or a mesh on top of the p^+ or n^+ doped layer. These regions (dopant + metal) constitute the dead layer of the material, where part of the energy deposited by particles is not measured by the detection system. The thickness of the dead layer can vary for both the aluminum cover and the band on the detector.

One of the objectives during analysis is to correct for the energy loss in the dead layer. Additionally, guard rings are used to create dead space for particle detection. These rings surround the p and n bands and help eliminate edge effects, ensuring a uniform potential across all bands, including those at the edges of the detector. This results in a consistent depletion zone throughout the detector.

In our specific experiment, 16 horizontal n-band and 16 vertical p-band DSSD detectors were used, providing a total of 256 pixels or detection regions for charged particles. However, there are only 32 energy signals available due to the configuration. Each pixel measures 3×3 mm^2 and is separated by a 0.1 mm SiO_2 insulator. The active detection surface area is 49.5×49.5 mm^2. The p bands were positioned facing the radiation source, making the n bands the rear ones. Only one detector (DSSD1) was placed in the reverse direction. The reverse voltage required for complete depletion varies between 20 and 200 V, depending on the thickness of the detector. The leakage current ranges from 60 nA to 600 nA for DSSDs and from 200 nA to 2 μA for PADs.

The front face of the detector is covered with aluminum in a mesh-like configuration, resulting in a variable thickness of the dead layer. On the rear face, the aluminum is in the form of a sheet, providing a homogeneous dead layer. Typically, the dead layer thickness consists of 50 nm (doped) plus mesh-like metal on the front side, and 400 nm (doped) plus 200 nm (metal) on the back side.

In addition to determining the position and energy of incident particles, DSSDs can be combined with other semiconductor detectors (PADs), in a telescope configuration. This configuration allows for the identification of different types of particles present in the measurement.

PADs are silicon detectors without segmentation and are typically thicker than DSSDs. They are primarily used for beta spectroscopy since beta particles have a larger range compared to charged particles. PADs can also be employed to stop high-energy charged particles, which require greater thickness for effective stopping power. In the IS545 experiment, four PADs with different thicknesses were utilized.

The telescope configuration involves placing a PAD behind a thinner DSSD which

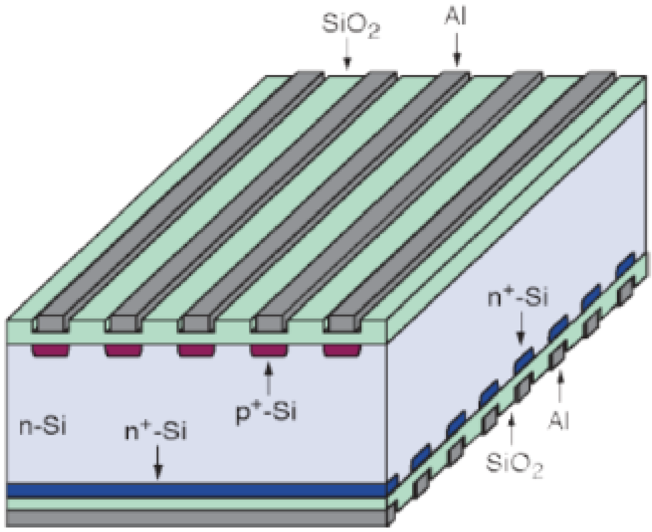

Figure 3.5: Double Sided Silicon Strip Detector.

is shown in Fig 3.6. The incident particle deposits part of its energy in the front detector (DSSD) and the remaining energy is deposited in the rear detector (PAD). By plotting the energy of the DSSD as a function of the energy of the PAD (or the sum of energies), a graph is obtained where particles of different charges follow hyperbolic curves. This configuration helps to distinguish protons from beta particles, as beta particles do not exhibit this hyperbolic behavior. Additionally, the telescope configuration allows for the rejection of particles that are not of interest, effectively selecting the particles for analysis.

The telescope configuration is particularly useful for selecting charged particles emitted after a beta emission, enabling the cleaning of spectra from beta contamination and facilitating the study of low-energy protons.

In conclusion, the use of silicon detectors, such as DSSDs and PADs, is highly suitable and necessary for detecting charged particles. To reconstruct the energy and emission angle accurately, employing DSSDs and PADs, preferably in a telescope configuration, around the radiation source is very important for our analysis.

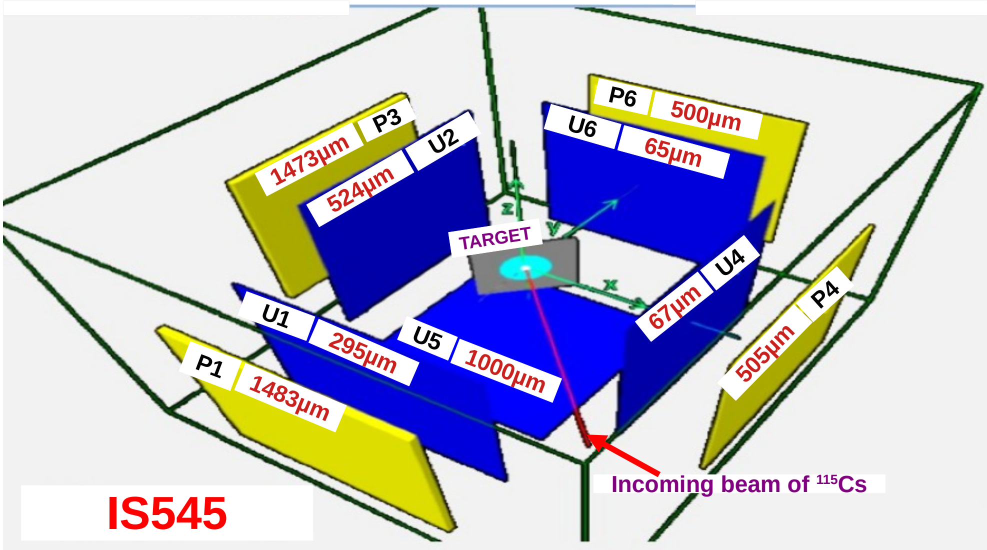

Figure 3.6: Schematic diagram of Double Sided Silicon Strip Detector and PAD detectors during the experiment IS545 at ISOLDE, CERN.

Chapter 4

Calibration

In chapter III, a detailed description of the detectors which were used in the experiment (IS545) has been presented. In this chapter I shall discuss about the calibration of those detectors and the procedure of extraction of energy and time from the calibrated data for further analysis. Here I will also discuss about the efficiency of those detectors.

4.1 Calibration of the detectors

Calibration of the detector is very crutial step for experimental nuclear physics. Calibration ensures that the detectors respond accurately to the radiation they are designed to measure, and it establishes a relationship between the detector's signal and the energy or properties of the incident charge particle. This calibration process is fundamental for obtaining reliable and precise experimental data. Calibrations should be performed regularly to ensure the continued accuracy and reliability of the detectors. Additionally, documenting calibration procedures and results is essential for traceability and for maintaining the quality of experimental data in nuclear physics research. We have used two types of detectors that are Double sided silicon strip detectos and Clover(Hp-Ge) detectors.

4.2 Efficiency of detectors

Detection efficiency is a critical parameter for any detection system, whether it's used in scientific research, medical imaging, industrial quality control, or other applications involving the measurement of particles or radiation. It quantifies how effectively a detector converts incident particles or radiation (input signals) into measurable output signals. A detector with high detection efficiency is desirable for several reasons, as we mentioned:

High Conversion Efficiency:

High detection efficiency implies that a significant portion of the incident particles or radiation is converted into measurable signals. This is crucial for obtaining accurate and reliable data from the detector.

Short Dead Time:

Dead time refers to the time interval during which a detector is unable to record subsequent events after registering one event. Short dead times are important because they enable the detector to handle a high rate of incoming particles or radiation without missing or overlapping signals.

Low Noise:

Noise in a detector's output signals can introduce uncertainty and reduce the quality of measurements. High detection efficiency can help minimize noise relative to the signal, improving the signal-to-noise ratio.

Achieving high detection efficiency often involves optimizing various aspects of the detector design and operation, depending on the type of particles or radiation being detected:

Material Selection:

Choosing the right detector material is critical. Different materials have varying levels of sensitivity to different types of particles or radiation. For example, silicon detectors are commonly used for detecting charged particles, while scintillators are used for detecting photons.

Geometry and Size:

The size and geometry of the detector can impact its efficiency. Optimizing these factors can maximize the probability of particle or radiation interaction within the detector's active region.

Efficient Conversion:

Ensuring that the detector has a high probability of converting incident particles or radiation into detectable signals is essential. This may involve factors like the thickness of the detector material, the presence of amplification structures, or coatings to enhance absorption.

Electronics and Signal Processing:

Efficient electronics and signal processing techniques can help improve detection efficiency by minimizing signal loss and enhancing the sensitivity of the detector.

In practical applications, detectors with high detection efficiency are often favored because they allow for better sensitivity and accuracy in measuring particles or radiation. However, achieving high detection efficiency may involve trade-offs with other factors, such as cost, complexity, and physical size, depending on the specific application's requirements.

4.3 Calibration of Clover detectors

HPGe detectors are calibrated using known γ-ray sources. Typically, we use sources with γ-ray energies spanning the energy range of interest. Common sources include ^{60}Co, ^{137}Cs, and ^{152}Eu. Here we have used ^{152}Eu as γ-ray source of known strength for calibration of the HpGe Clover detectors.

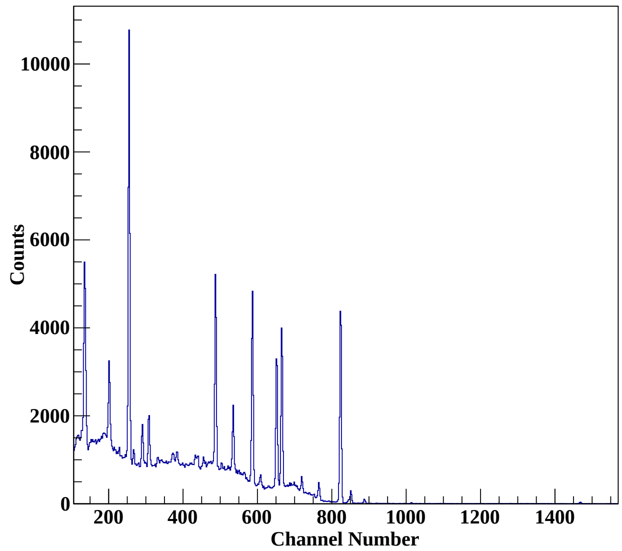

Figure 4.1: Raw gamma spectrum of ^{152}Eu obtained from Clover detector.

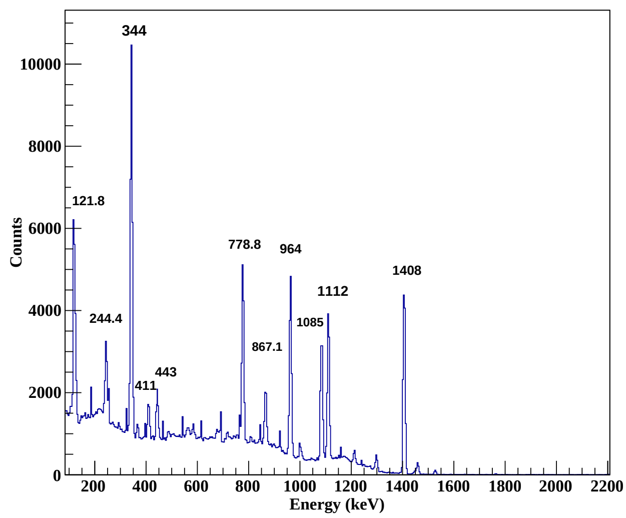

Figure 4.2: Calibrated gamma spectrum of ^{152}Eu obtained from Clover detector.

Germanium detectors have been calibrated first with a ^{152}Eu source. This calibration was improved using the background peaks (^{40}K, ^{232}Th). (four crystals for each of the four Ge detectors), and the sum spectrum of all crystals. This is the one we used for the rest of the analysis.

Calibration with a ^{152}Eu Source:

Calibration is a crucial step in using detectors like Germanium detectors. It involves determining the relationship between the energy deposited in the detector and the output signal produced. In this case, a ^{152}Eu source was used for calibration. This is a common practice in gamma-ray spectroscopy as ^{152}Eu emits gamma rays at known energies, making it suitable for calibrating the detector's energy response. Fig 4.1 shows the raw spectrum of ^{152}Eu obtained from Clover detector and Fig 4.2 shows the corresponding calibrated spectrum.

Improving Calibration with Background Peaks:

After the initial calibration with the ^{152}Eu source, further refinements were made using background peaks. It's common to observe background radiation in experiments, and specific gamma-ray lines are associated with naturally occurring radioactive isotopes like (^{40}K) and (^{232}Th). These background peaks were likely used to fine-tune the calibration of the Germanium detectors, ensuring accurate energy measurements.

Use of Segmented Detectors:

It's mentioned that four segmented detectors were used. Segmented detectors divide the active volume of the detector into smaller segments, allowing for more precise localization of gamma-ray interactions. This segmentation can improve energy resolution.

Obtaining 16 Calibration spectra:

It appears that each of the four clover detectors was further divided into four segments, resulting in a total of 16 calibration spectra. This likely means that for each crystal or segment, the energy response was characterized at various gamma-ray energies. These lines represent the detector's response at different energy levels.

Sum Spectrum for Analysis:

Finally, it's mentioned that the sum spectrum of all crystals or segments was used for the rest of the analysis. This means that the data from all the individual detectors and segments were combined to create a single spectrum. This aggregated spectrum is used for further analysis of the data collected in the experiment. So we have performed a comprehensive calibration process was carried out to ensure the accuracy of the Germanium detectors in measuring γ-ray energies. This is essential for any experimental work involving γ-ray spectroscopy, such as nuclear physics or environmental monitoring for radioactive materials.

Algorithm for add-back in clover detector:

When the γ-rays deposites all its energy by photoelectric process then a single crystal is enough to measure the energy of that γ-ray. But with the increase of the γ-ray energy the other two processes (compton effect, pair-production) play important role. Hence the energy corresponding to a single γ-ray is deposited in more than one crystal. So it is necessary to find out the crystals which are fired corresponding to that single γ-ray related event. We considered that the highest energy deposited crystal is fired at first and the nearest two neighbours receive the remaining energy if they are fired at all at that particular event. So after identifying the highest energy deposited crystal , the energy deposited in that crystal is summed with the energy deposited in the nearest neighbour crystals(excluding the corner crystal).

Here is the overview of the whole calibration process of clover detector.

- Calibration of all four Clover detectors using standerd radioactive source ^{152}Eu.

- Gain matching of all the crystal of Clover detectors.
- Identification of the crystal number to which the maximum energy is deposited.
- Check the neighbouring crystals.
- Adding the deposited energies of the neighbouring crystals(excluding the corner crystal) with the central one.

4.4 Efficiency of Clover detector

The efficiency of a germanium detector, or any radiation detector for that matter, is an important parameter that quantifies how effectively it can detect radiation. In the context we provided, the efficiency of the germanium detector is determined by comparing the number of photons detected by the detector to the total number of photons emitted by a radioactive source. This efficiency can be calculated using the following equation:

Efficiency(%)=(number of detected photons/total number of emitted photons)×100

Here's what each of the terms in the equation means:

Number of detected photons: This refers to the actual number of photons that are registered by the germanium detector. These photons typically correspond to the area under the peaks observed in the spectrum of the detector.

Total number of emitted photons: This represents the total number of photons that were emitted by the radioactive source. This value is determined by the source's activity and the measurement time.

To calculate the efficiency using this method, we need to:

Measure the area of the peaks in the spectrum of the detector corresponding to the photons of interest. This is done to determine the number of detected photons.

We have to know the activity of the radioactive source. Activity is usually measured in becquerels (Bq) and represents the rate at which the source emits radiation. We measure the time for which the source (source measurement time) is exposed. This is usually measured in seconds. Fig 4.3 shows the absolute efficiency curve of the Germanium detectors. Once we have these values, we can plug them into the efficiency equation to calculate the efficiency of our germanium detector. Keep in mind that the intrinsic efficiency of the detector, which depends on the type of detector material and its design, might not be 100%. Therefore, it's important to take into account both the intrinsic efficiency and the geometric factors when determining the overall efficiency of the detector.

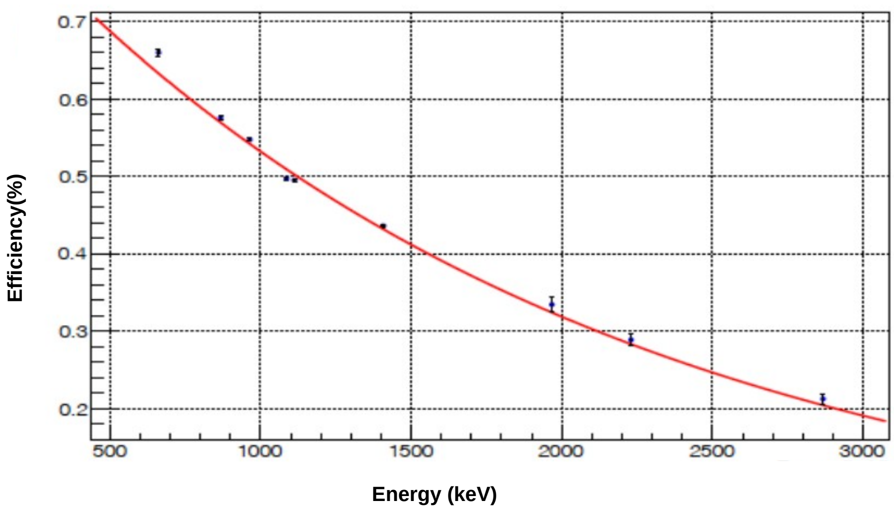

Figure 4.3: Absolute efficiency of the four clover detectors.

4.5 Calibration of Double sided silicon strip detector

The silicon detectors (both thick and thin DSSDs and PADs) were calibrated using the standard alpha sources, ^{148}Gd, ^{241}Am, ^{239}Pu, ^{249}Cf.

Calibrating the energy response of Silicon detectors is a critical step in experimental physics and is typically performed to ensure accurate measurements of particle energies. The calibration process we describe assumes that the response of the detectors is linear with respect to the energy deposition. Here is a general outline of the calibration procedure:

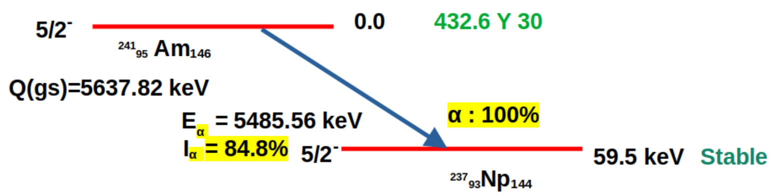

Figure 4.4: Level scheme of ^{241}Am.

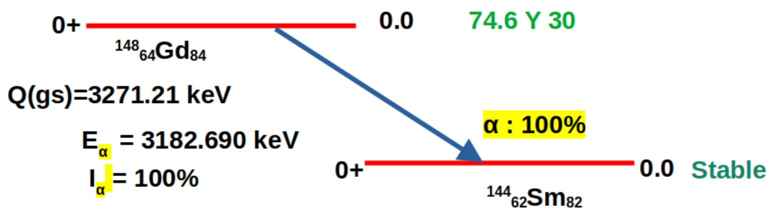

Figure 4.5: Level scheme of ^{148}Gd.

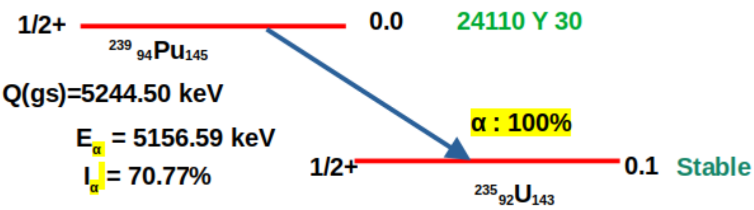

Figure 4.6: Level scheme of ^{239}Pu.

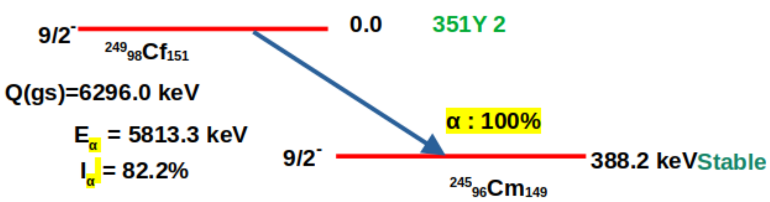

Figure 4.7: Level scheme of ^{249}Cf.

Selection of Calibration Sources:

We have used appropriate calibration sources that emit known energy particles or radiation. It is important to note that these sources should cover a range of energies so that any one can calibrate the detectors. Fig 4.4, 4.5, 4.6, 4.7 show the decay scheme of ^{148}Gd, ^{241}Am, ^{239}Pu, ^{249}Cf respectively.

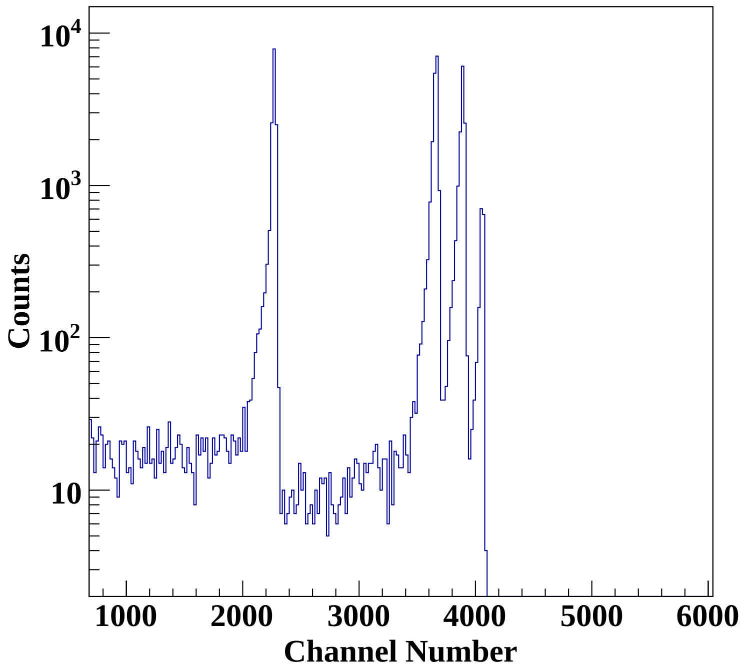

Figure 4.8: Raw charge particle (Alpha) spectrum obtained from one Double Sided Silicon Strip detector by using alpha sources.

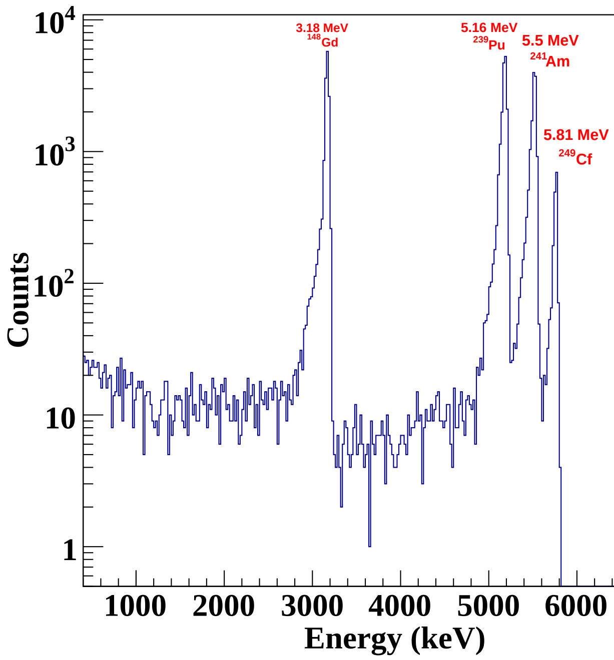

Figure 4.9: Calibrated charge particle (Alpha) spectrum obtained from one Double Sided Silicon Strip detector.

Positioning of Sources:

We kept the selected calibration sources at a known distance from the Silicon detectors. This distance should be consistent for all calibration measurements to ensure reproducibility.

Single Energy Calibration:

We have perform a series of measurements with each calibration source individually. For each source, we have recorded the energy deposition signal obtained from the Silicon detectors. The energy deposition signal is in the form of voltage or charge produced by the detectors.

Fitting of Calibration Curve:

We have Plotted the recorded energy deposition signals against the known energies of the calibration sources. Since linearity is assumed, one should aim to fit a straight line to these data points. The equation of the line should relate the energy deposition signal to the known energy: Energy deposition = slope × (channel number) + intercept.

The slope and intercept of this calibration curve were determined from the data.

Extraction of Calibration Parameters:

We calculated the slope and intercept of the calibration curve through a linear regression or curve-fitting technique. These parameters are crucial for converting future energy deposition signals from the detectors into actual particle energies.

Application of Calibration:

Whenever we used the Silicon detectors to measure particle energies in our experiment, we have to apply the calibration parameters obtained in previous step to convert the recorded energy deposition signals into actual particle energies.

Quality Assurance:

Regularly we verified and validated the calibration by measuring known sources and compared the calibrated energies to their expected values. This ensured that the detectors remain accurate over time.

Documentation:

We Kept comprehensive records of this calibration procedure, including source details, measurement conditions, calibration parameters, and quality control measures. This documentation was essential for maintaining traceability and reproducibility for our experiment. Fig 4.8 shows the raw spectrum(charge particle) obtained from DSSD and Fig 4.9 shows the corresponding calibrated spectrum.

throughout the experiment, since to increase the statistics we have to add all the files taken throughout the experiment at different times. It's important to note that while assuming linearity simplifies the calibration process, it may not always hold true over the entire energy range. In cases where non-linearity is significant, more complex calibration techniques, such as polynomial fits or piecewise linear fits, may be necessary to improve accuracy. Additionally, careful consideration of environmental factors and detector stability is essential to ensure the reliability of the calibration. Stability checks are crucial in experimental physics to ensure that the detectors maintain consistent behavior over the course of an experiment.

This is particularly important when some one plan to combine data collected at different times or during different runs to increase statistics. Here is a general procedure that we had used for checking the stability of the system:

Data Analysis Binning:

We Divided data into time bins or segments that were appropriate for experiment. The choice of bin size is based on the expected time scale of any potential variations in detector behavior.

Signal Histograms:

We Created histograms of relevant detector signals or quantities of interest for each time bin. These histograms captured the distribution of data points within each bin. Here we used ROOT data analysis software to create these histograms.

Comparison of Histograms:

We Compared the histograms from different time bins. We looked for any noticeable variations in the shape, mean, or width of the distributions. Anomalies or drifts in detector behavior may manifest as shifts or changes in these histograms.

Statistical Tests:

We applied statistical tests to quantify the stability of the system. Common tests include: Chi-squared test: This test can help to assess whether the observed data within each time bin matches an expected distribution. Mean and Variance Comparison: We calculated the mean and variance of the data within each time bin and compared them to see if they remain consistent.

Trend Analysis:

We looked for trends or patterns in the data over time. revealtrends or outliers that may indicate instability.

Environmental Monitoring:

We monitored environmental conditions that could affect detector performance, such as temperature, humidity, or radiation levels. of the detectors with the reference detectors to identify deviations.

Re-calibration:

Fot the significant drift or instability we considered re-calibrating the detectors or implementing corrections to account for the observed changes. actionstaken. This documentation is essential for data quality control and reproducibility.Regularly performing stability checks throughout the experiment and addressing any identified issues promptly will help ensure the reliability of the data when combining files taken at different times. It's important to have a well-documented and systematic approachto system stability assessment as part of the experimental workflow.

The procedure we have described involves, calibration by strip and verification of the energy resolution for a set of detectors. This calibration and resolution check process helped us to ensure that the detectors were providing accurate and stable measurements. Here's a step-by-step overview of the procedure:

Stability Verification (Already Discussed):

As we mentioned, before proceeding with calibration, it's essential to verify the stability of the system over the duration of the experiment. This ensures that any variations in detector behavior were minimized.

Data Combination:

We combined all the data files obtained throughout the experiment for further analysis.

Band-by-Band Calibration (Detector's Energy Calibration):

We performed individual energy calibrations for each of the 32 bands within each detector. This calibration mapped the detector signal(voltage or charge) to actual energy depositions. We Created calibration curves specific to each band. These curves were used to convert signal measurements into energy values for each band.

Front and Back Side Spectra:

After calibrating each of the 32 bands individually, we combined the data from the 16 front bands to create a spectrum for the front side of each detector. Similarly, we combined the data from the 16 back bands to create a spectrum for the back side of each detector.

Resolution Check:

We calculated the energy resolution for both the front and back spectra. Energy resolution typically involves measuring the width of the peaks in the spectra, often using the full width at half maximum (FWHM). We compared the energy resolution of the front and back spectra. The goal was to identify which side of the detector provides the best energy resolution.

Side Selection:

We chose the back side of the detector that exhibits the best energy resolution for further analysis. information is well-organized and easily accessible for data analysis and future reference.

Data Analysis:

We proceed with the data analysis using the selected spectra. This could involve tasks such as identifying peaks, fitting spectral lines, and extracting relevant information about the particles or radiation being detected. By following this procedure, we ensured that detectors were accurately calibrated and we were using the back side of the detector that provided the best energy resolution for the analysis. This systematic approach helped to maintain data quality and allows for more reliable results in the experiment.

There were many conditions which were important for ensuring data quality and eliminating noise. Let's summarize and understand each condition:

Multiplicity Condition (Event Multiplicity > 0 and < 3):

This condition helped us to reduce noise in the spectra by excluding events with a multiplicity greater than three in both the front and rear of the DSSDs. High multiplicity events could indicate interactions with multiple particles or noise, and excluding them ensured that we focused on genuine events.

Individual Energy Condition (Energy $<$ 100 keV):

Events with energies less than 100 keV were excluded from the analysis. This is based on the assumption that events below this energy threshold were likely to be noise or unrelated to the desired particle interactions. Since we did not expect proton events at such low energies, it was a reasonable threshold to apply.

Energy Difference Condition (Front-back Energy Difference $<$ 25 keV):

To ensure that signals from the front and back bands of the DSSDs correspond to the same physical event, a condition was imposed that their energy difference (in absolute value) must be less than 25 keV. This condition ensured that we were dealing with events where both the front and back signals were likely due to the same particle interaction. It helped us to eliminate events where the signals might be unrelated or from different interactions.

Elimination of Edge Effects:

Edge effects could lead to misinterpretation of events, especially when a particle interacts in the outermost bands and doesn't reach the back detector PAD. To address this, events from the leading and trailing bands of the detector ends were removed from the analysis. While this slightly reduced the effective solid angle and detector efficiency, it helped to ensure that we were analyzing events where the particle's trajectory was consistent with a genuine interaction in both the front and back detectors. By applying these conditions, we were effectively cleaning and filtering the data to focus on high-quality events that were more likely to represent the desired physical interactions. This improved the accuracy and reliability of the analyses, especially when dealing with particle spectroscopy or related experiments. Additionally, documentation of the application of these conditions in the analysis was essential for transparency and reproducibility of the results.

Fig 4.10, 4.11 and 4.12 present data related to a Double-Sided Silicon Strip Detector (DSSD), referred to as DSSD4, DSSD6 and DSSD5 respectively. The data appears to be related to the energy deposited in the front and back bands of the DSSD when observing the decay of ^{115}Cs. We could see that almost 88% of the statistics (data points or events) fall within an interval of 25 keV. This suggests that most of the observations had a relatively small difference in energy between the front and back bands.

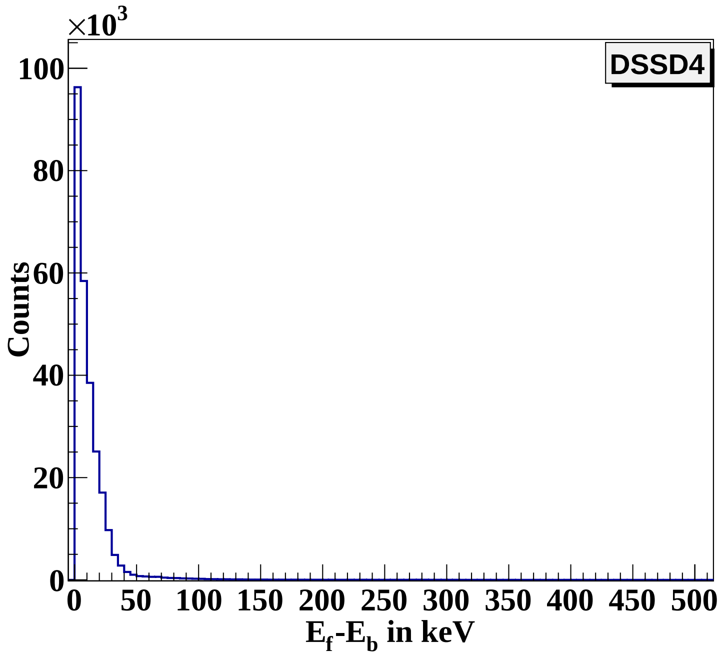

Figure 4.10: Difference in absolute value of the energy deposition in the front and back bands for the DSSD4. It is evident from this figure, most of the statistic (90%) falls within an interval of 25 keV.

Fig 4.13 to Fig 4.18 are showing a graphical representation of the energy of the back bands as a function of the energy of the front bands for the DSSD4, DSSD6 and DSSD5 detector respectively under two different sets of conditions. Here's a breakdown of what the figures and its description are conveying:

In the Fig 4.13, 4.14 and 4.15, only two conditions have been applied: one related to the multiplicity of events and the other related to individual energy. These conditions are applied to both the spectra of the front and back bands of the DSSD4, DSSD6 and DSSD5 detectors. The result is that almost 90% of the statistics or data points are preserved. This means that most of the data points remain relevant. Events that are removed or filtered out are those that do not meet

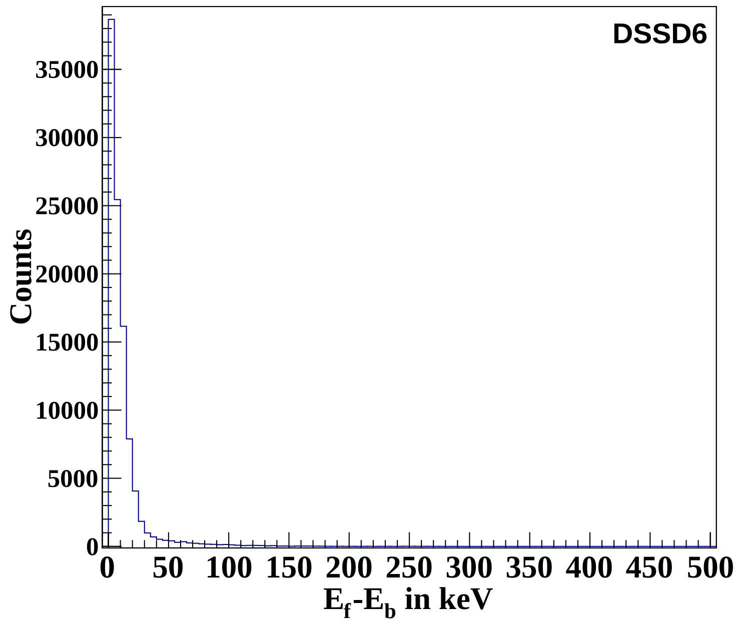

Figure 4.11: Difference in absolute value of the energy deposition in the front and back bands for the DSSD6. It is evident from this figure, most of the statistic (90%) falls within an interval of 25 keV.

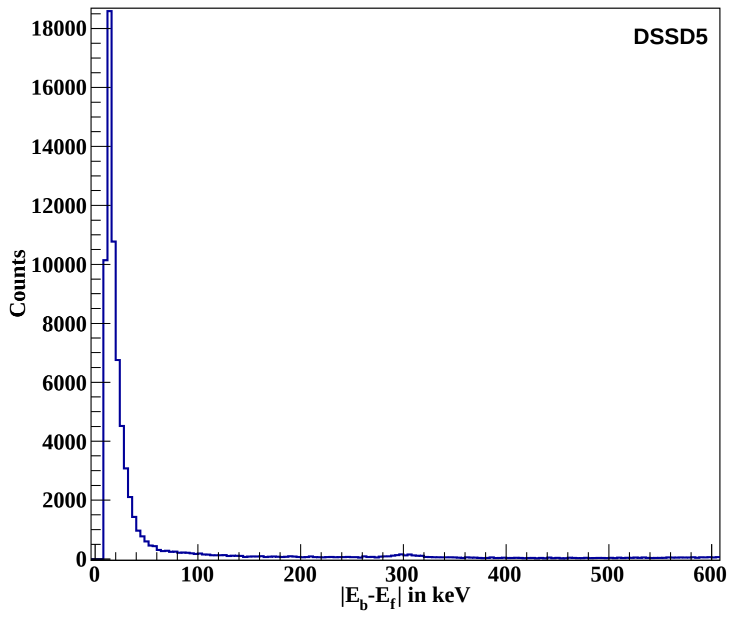

Figure 4.12: Difference in absolute value of the energy deposition in the front and back bands for the DSSD5. It is evident from this figure, most of the statistic (88%) falls within an interval of 25 keV.

these conditions. This may include events where energy is deposited in only one band of the detector.

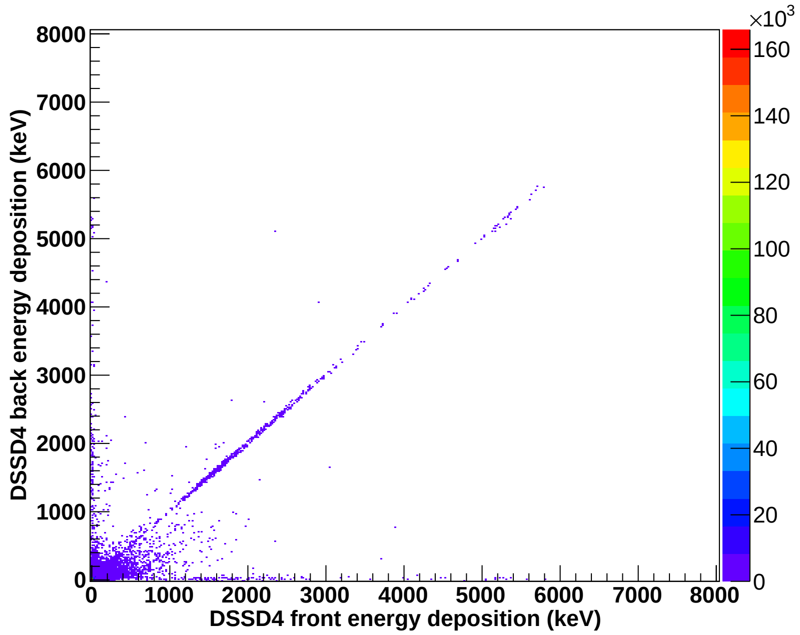

Figure 4.13: Two dimensional energy deposition plot between front and back side of DSSD4.

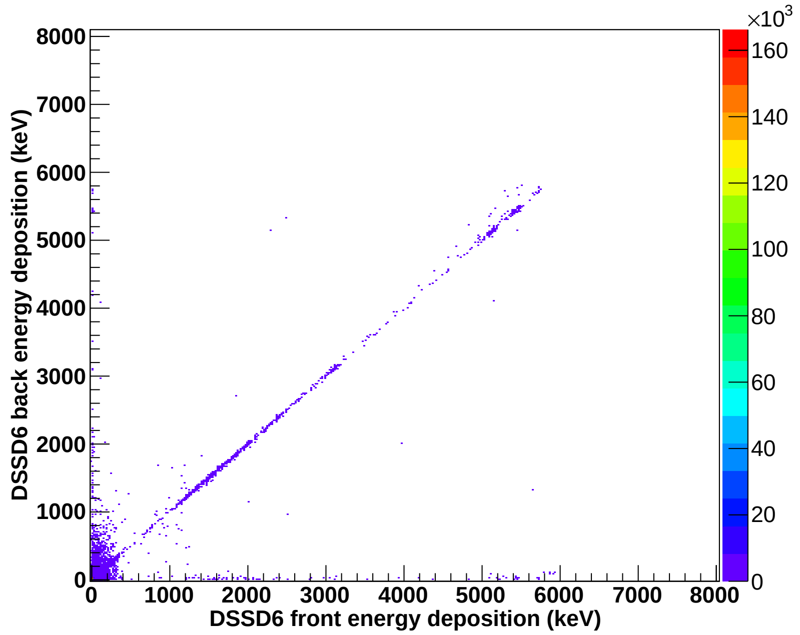

Figure 4.14: Two dimensional energy deposition plot between front and back side of DSSD6.

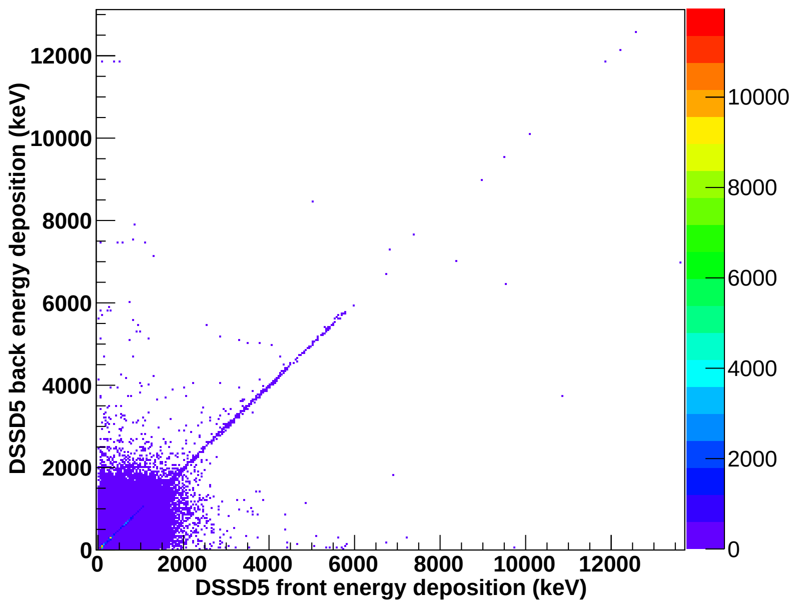

Figure 4.15: Two dimensional energy deposition plot between front and back side of DSSD5.

In the Fig 4.16, 4.17 and 4.18, additional conditions are applied in addition to the multiplicity and individual energy conditions. Specifically, a condition is applied to the difference in energies between the front and rear bands of the detectors (DSSD4, DSSD6, DSSD5 respectively). The effect of applying this additional condition is that off-diagonal events are removed from the data. These off-diagonal events are characterized by forming vertical and horizontal lines in the Fig 4.13, 4.14,and 4.15 respectively. The off-diagonal events represent situations where energy is deposited in one band on one side of the detector and in multiple bands on the other side. This condition eliminates such events.

conditions help filter and refine the data, preserving the most relevant statistics and removing events that do not meet the specified criteria. The bottom part of the figure, in particular, shows the effect of applying an additional condition related to the difference in energies between the front and rear bands, which helps eliminate certain types of events that do not exhibit the desired behavior.

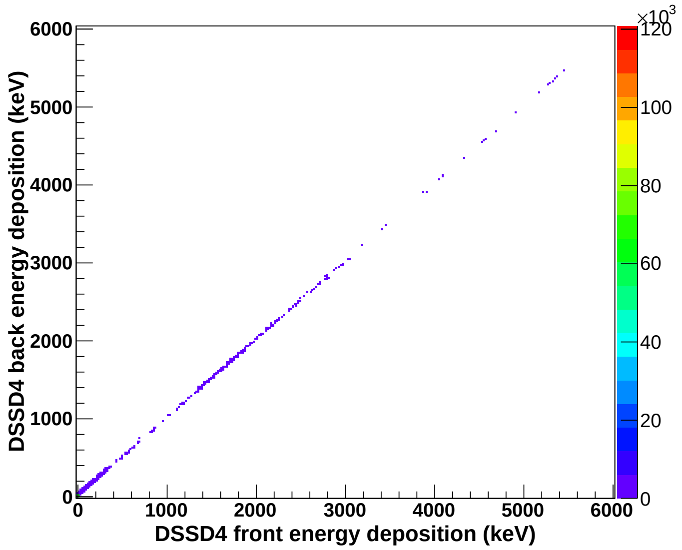

Figure 4.16: Two dimensional energy deposition plot between front and back side of DSSD4.

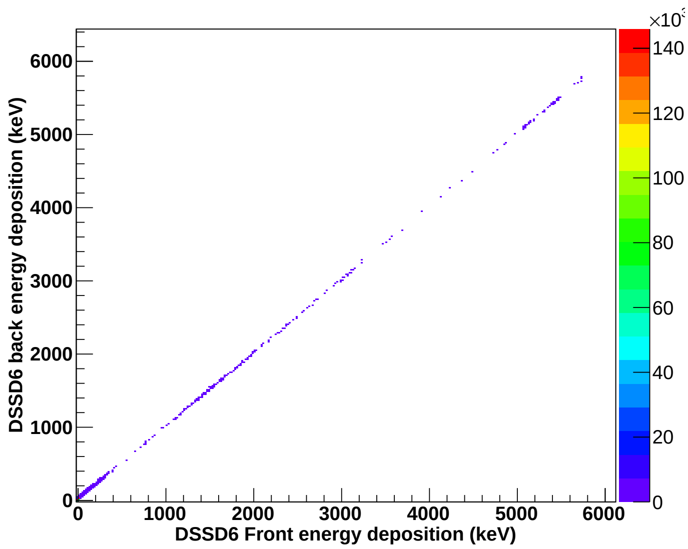

Figure 4.17: Two dimensional energy deposition plot between front and back side of DSSD6.

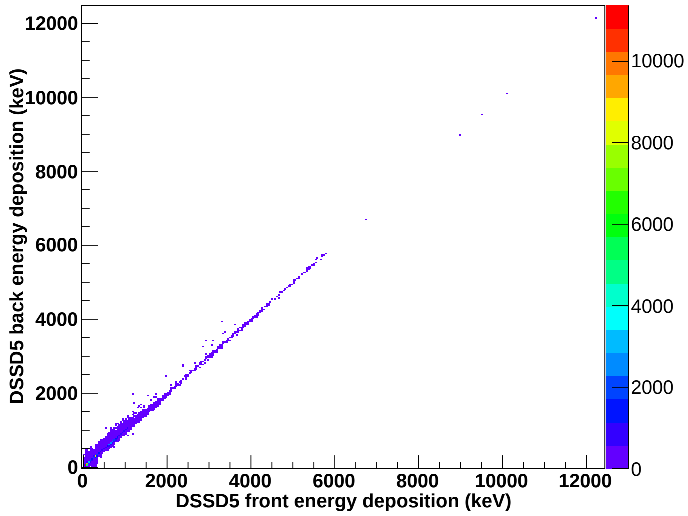

Figure 4.18: Two dimensional energy deposition plot between front and back side of DSSD5.

4.6 Efficiency of DSSD (Double-Sided Silicon Strip Detector) and PAD Detectors

Intrinsic Efficiency:

Silicon detectors have a high intrinsic efficiency for detecting charged particles, which means they are highly likely to detect any charged particle that interacts with them. However, some factors like interstrip effects can reduce this efficiency slightly.

Assumption of Particle Detection:

In our work, we assumed that each emitted particle was detected, which implied that we were considering the ideal case where all charged particles were interacting with the detector were counted. Fig 4.19 represents the hit pattern of DSSD4 from ^{115}Cs data which proves that the response of all the front and back strips of DSSD4 for detecting the charge particles is very good. It is clear from the hit pattern of DSSD5 that the first front strip of DSSD5 is not working which is shown in Fig 4.20. Similarly Fig 4.21 represents the hit pattern of DSSD6 where all the front and back strips of DSSD6 perform well with respect to the detection of the charge particles.

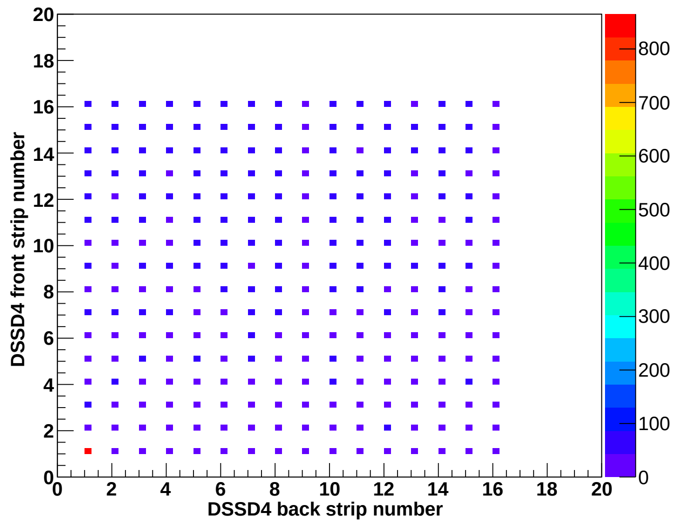

Figure 4.19: Hit pattern of DSSD4 from ^{115}Cs data. The colour gives the number of counts in each pixel.

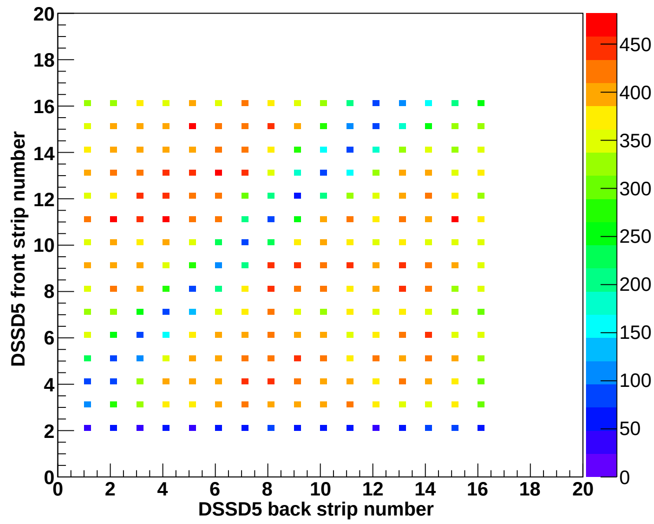

Figure 4.20: Hit pattern of DSSD5 from ^{115}Cs data. The colour gives the number of counts in each pixel.

Total Efficiency:

The total efficiency of the detector was determined by the solid angle subtended by each detector. This means that the detector's geometry plays a crucial role in its overall efficiency.

Solid Angle Calculation: The solid angles have been calculated in different

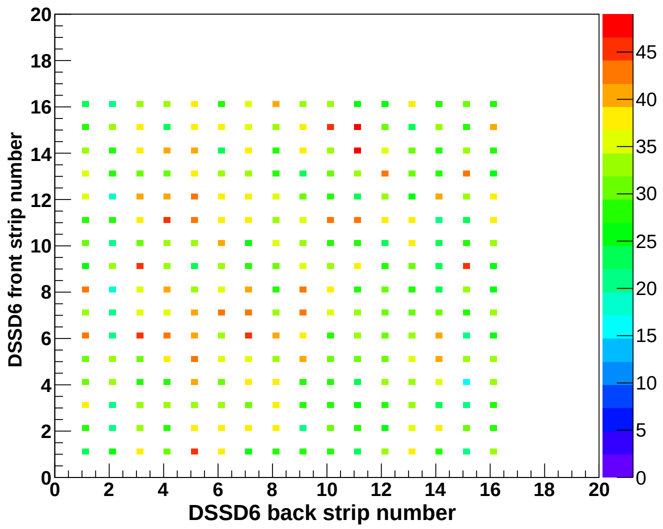

Figure 4.21: Hit pattern of DSSD6 from ^{115}Cs data. The colour gives the number of counts in each pixel.

scenarios:

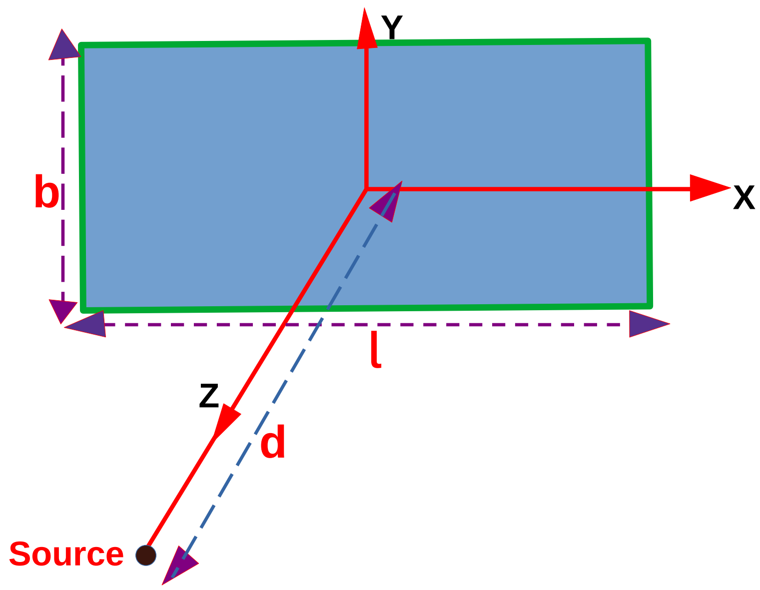

Figure 4.22: Schematic diagram of a double sided silicon strip detector for the calculation of solid angle coverage.

Fig 4.22 shows the solid angle coverage by a rectangle of dimension b×l at a distance d from the source is

$$w = 4\sin^{-1}\left[\frac{(l.b)}{\sqrt{(l^2+4d^2)(b^2+4d^2)}}\right] \tag{4.1}$$

In our case surface area of the DSSD is almost 50x50 mm^2. Using the equation 4.1 we have calculated the solid angle coverage of all the DSSD and PAD detectors. The characteristics and performance of all DSSD, PAD and Clover detectors are shown in the table 4.1, table 4.2 and table 4.3 respectively. Fig 4.23 shows the dimensions and the distances of all the DSSD and PAD detectors.

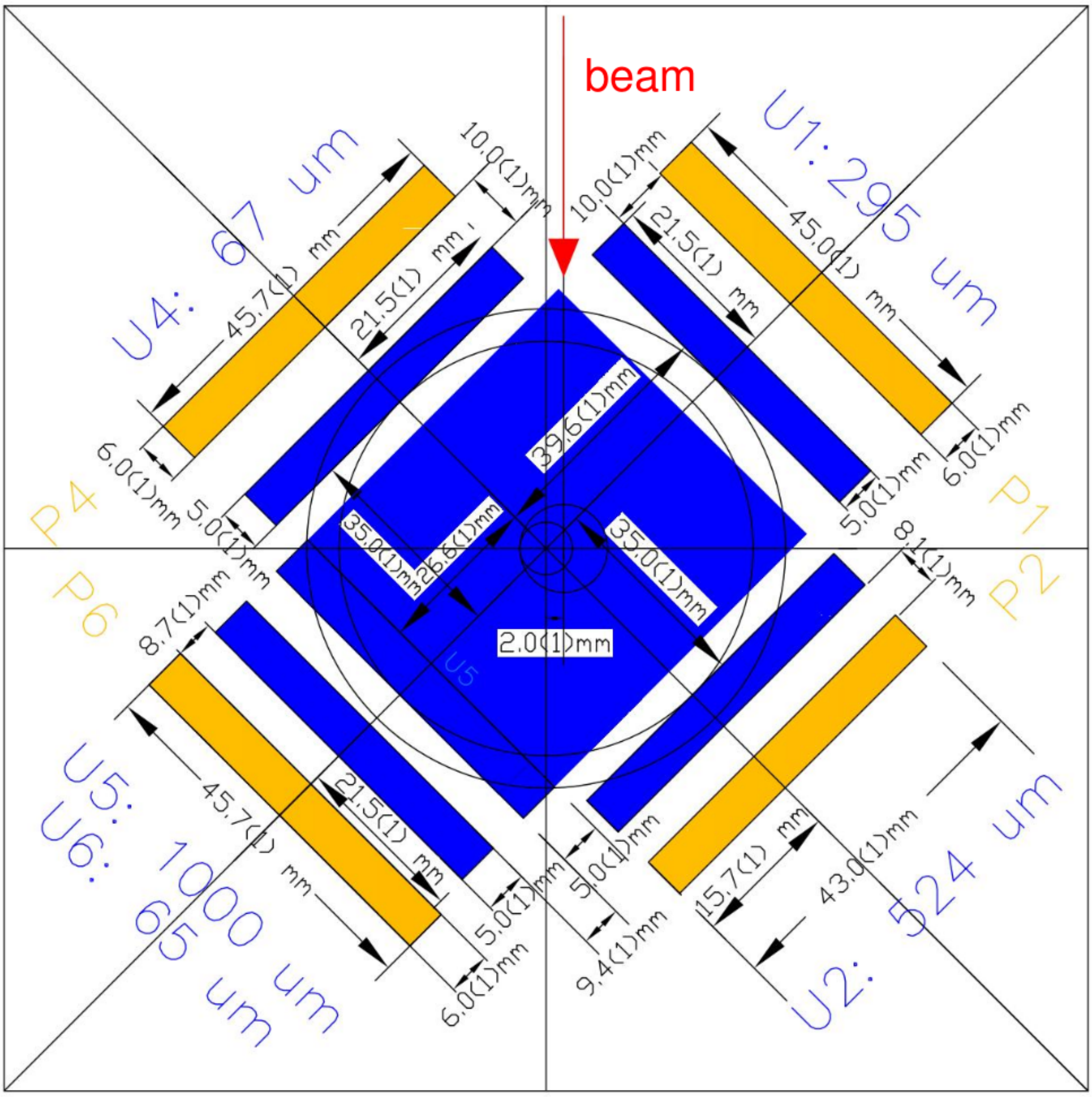

Figure 4.23: Elevation view of the experimental device with its measurements. DSSD5 is the only detector in the lower plane.

Table 4.1: Characteristics and performances of the Double sided silicon strip detector(DSSD).

Characteristics and performances of all DSSD								
Detector	Thickness (μm)	Dimension (mm^2)	Distance (mm)	Solid angle (Sr)	Solid angle (% of 4π)	Working conditon (Yes/No)	Proton stopping energy (MeV)	Alpha stopping energy (MeV)
DSSD1	295	43×43	39.6	0.9186	7.3	No	p< 5.9	α<23.9
DSSD2	524	43×43	35.0	1.1100	8.82	Yes	p< 8.4	α<34.1
DSSD4	67	43×43	35.0	1.1100	8.82	Yes	p< 2.5	α<10.1
DSSD5	1000	48×48	26.6	1.8617	14.80	Yes	p< 12.3	α<49.3
DSSD6	65	43×43	44.4	0.7644	6.08	Yes	p< 2.5	α<9.9

Table 4.2: Characteristics and performances of the PAD detector.

Characteristics and performances of all PAD								
Detector	Thickness (μm)	Dimension (mm^2)	Distance (mm)	Solid angle (Sr)	Solid angle (% of 4π)	Working conditon (Yes/No)	Proton stopping energy (MeV)	Alpha stopping energy (MeV)
PAD1	1483	45×45	54.6	0.583	4.64	No	p<15.3	α<61.4
PAD2	1473	43×43	48.1	0.669	5.32	Yes	p<15.2	α<61.1
PAD4	505	45.7×45.7	50.0	0.695	5.53	Yes	p< 8.3	α<33.4
PAD6	500	45.7×45.7	54.7	0.597	4.75	Yes	p<8.2	α<33.2

Table 4.3: Characteristics and performances of the Clover detectors.

Characteristics and performances of the Clover detectors					
Detector	Dimension (mm^2)	Distance (mm)	Solid angle (Sr)	Solid angle (% of 4π)	Working conditon (Yes/No)
Clover1	82×82	200	0.161	1.2	Yes
Clover2	82×82	200	0.161	1.2	Yes
Clover3	82×82	200	0.161	1.2	Yes
Clover4	82×82	200	0.161	1.2	Yes

Proton Detection Efficiency:

The total solid angle, or detection efficiency, for a proton is reported to be 46% of 4π when excluding bands that do not work. This means that, in this specific configuration, 46% of protons that interact with the detector are effectively detected.

It's important to note that the efficiency of a particle detector can depend on various factors, including the detector's design, materials used, and the specific particles being detected. Therefore, the reported efficiency of 46% of 4π is specific to the described configuration and conditions. The efficiency may vary in different experimental setups or with different types of particles.

Chapter 5

Data Analysis

The data analysis has been performed in the CERN-ROOT platform. The addback algorithm has been implemented for obtaining the final γ-ray spectrum. The charged particles were identified with telescopes of the DSSDs and the PAD detectors. After the decay of ^{115}Cs, the daughter nucleus, ^{115}Xe was populated with excitation energy up to 8.96 MeV which was above one proton, ($S_p = 3.31(2)$ MeV), two protons ($S_{2p} = 4.89(3)$ MeV), and α ($Q_\alpha = 2.5(1)$ MeV) thresholds [62]. Hence ^{114}I, ^{113}Te and ^{111}Te nuclei could be populated through emission of p, $2p$ and α, respectively. Thus, by measuring the delayed proton and alpha, the unbound excited states of the daughter nucleus can be reconstructed. By performing coincidence and anticoincidence with consecutive PAD detectors, the delayed particles, like β, α, proton etc. can be separated.

5.1 ΔE-E spectra of different DSSD and PAD detectors

Fig 5.1 shows the coincidence spectrum between the thin DSSD4 and the consecutive PAD detector(DSSD4-PAD4 telescope array). Similarly Fig 5.2 represents the coincidence spectrum between the thin DSSD6 and the consecutive PAD detector(DSSD6-PAD6 telescope array). From both figures we can see two clear patches of events distributions due to the protons and the betas. Fig 5.3 represents the coincidence spectrum between the thick DSSD2 and the consecutive PAD detector(DSSD2-PAD3 telescope array). From this figure we can not separate charge particles.

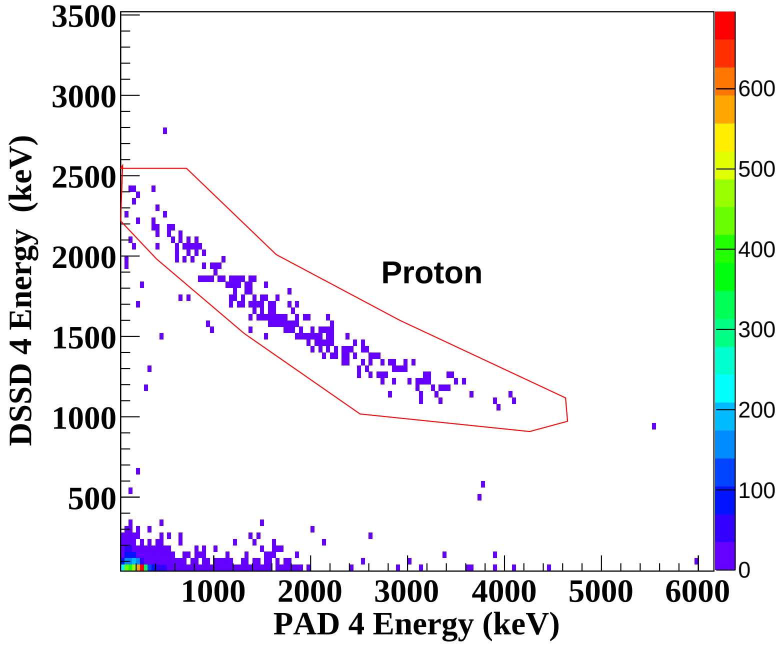

Figure 5.1: ΔE-E(DSSD4-PAD4) coincidence spectrum. Delayed protons with red contour and beta events are shown. Thickness of DSSD4 is 67 μ and thickness of PAD4 is 505 μ.

5.2 Proton energy in laboratory frame

Fig 5.4 represents the energy deposited particle spectrum(Red) for DSSD4(67 μ) detector overlaied with the proton spectrum (Blue) obtained from projection of proton patch in Fig 5.1 projected on thin DSSD4 detector.

Fig 5.5 represents the energy deposited particle spectrum(Red) for PAD4 (505 μ) detector overlaied with the proton spectrum (Blue) obtained from projection of proton patch in Fig 5.1 projected on thin PAD4 detector.

High energy protons deposite some of its energy in thin DSSD and rest of its

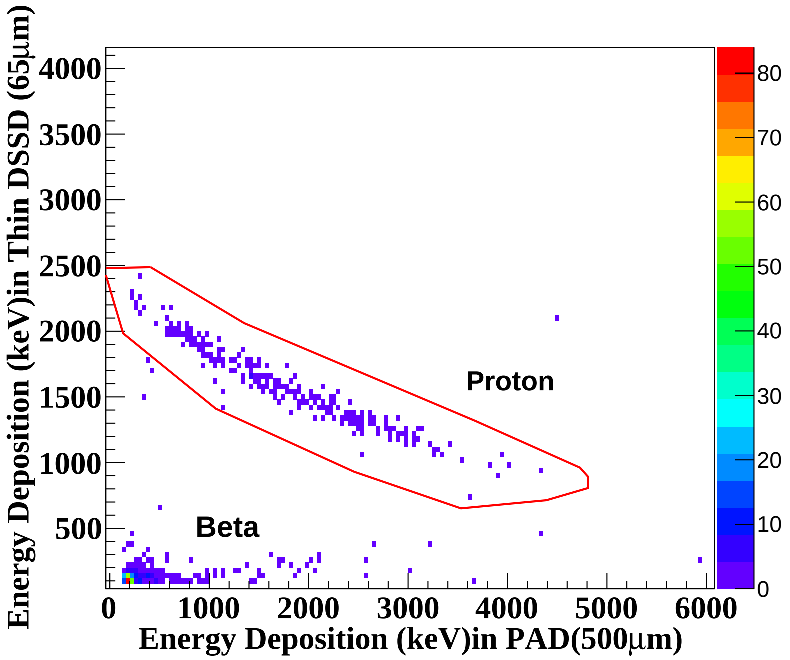

Figure 5.2: ΔE-E(DSSD6-PAD6) coincidence spectrum. Delayed protons with red contour and beta events are shown. Thickness of DSSD6 is 65 μ and thickness of PAD6 is 505 μ.

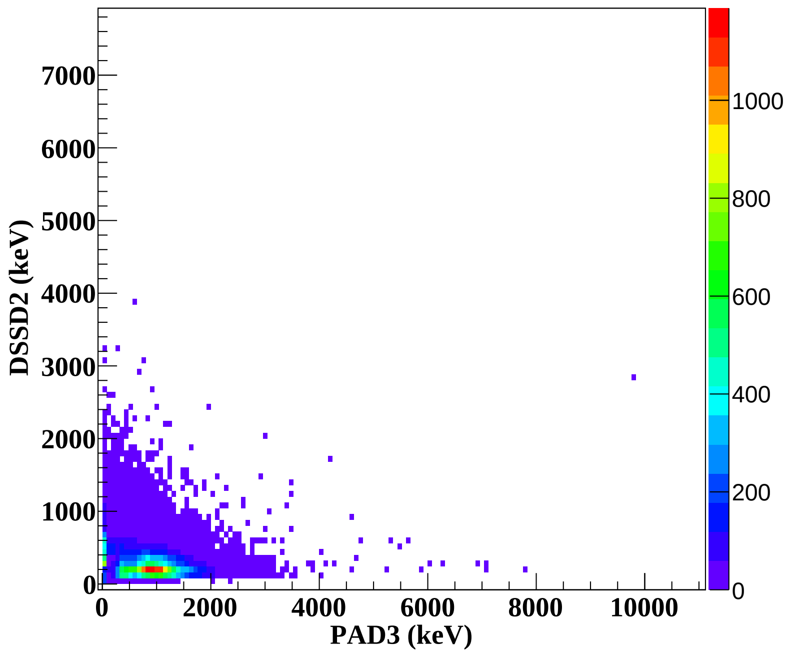

Figure 5.3: ΔE-E(DSSD2-PAD3) coincidence spectrum. Thickness of DSSD2 is 524 μ and thickness of PAD4 is 1423 μ.

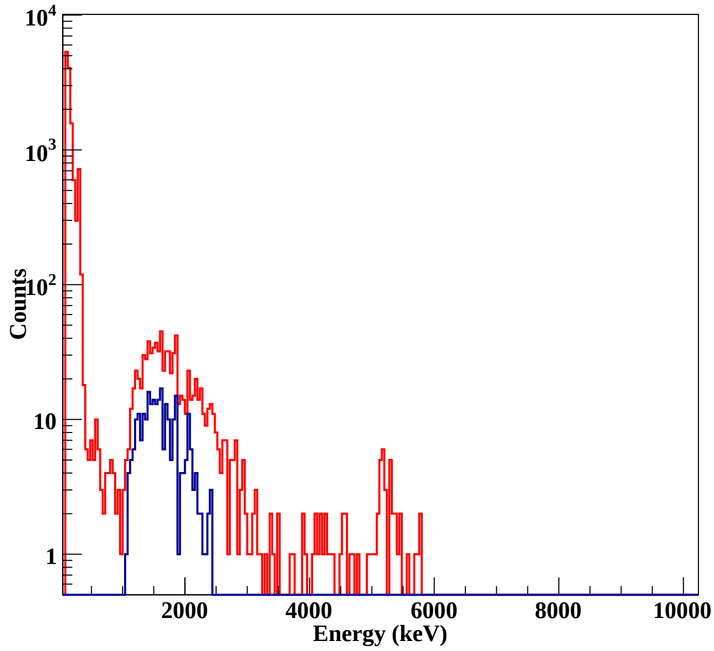

Figure 5.4: The energy deposition of all charge particles spectrum(Red) for DSSD4(67) detector overlaied with the proton spectrum (Blue) obtained from projection of proton patch in Fig 5.1 projected on thin DSSD4 detector.

energy is deposited in corresponding PAD detector placed behind that thin DSSD. The delayed proton energy spectrum (from 2.5 MeV to 5.4 MeV) wais obtained by adding the coincident events of the thin DSSDs and the corresponding PAD detectors. In this way we obtain high energy protons from DSSD4-PAD4 telescope configuration and from DSSD6-PAD6 telescope configuration. Then we have added those two parts to obtain the total coincidence high energy proton spectrum in laboratory frame, which is shown in Fig 5.6.

Fig 5.7 represents the overlay of the total coincidence spectrum with the individual coincidence spectrum obtained from DSSD4-PAD4 telescope configuration and DSSD6-PAD6 telescope configuration.

On the other hand the anti-coincident events are related to α or heavy clusters and the proton with energies below 2.5 MeV. As the Q_α value is 2.50(14) MeV, that means energy of the delayed alpha will be greater than 2.5 MeV.Therefore by applying proper anti-coincidence condition, below 2.5 MeV, between thin DSSDs

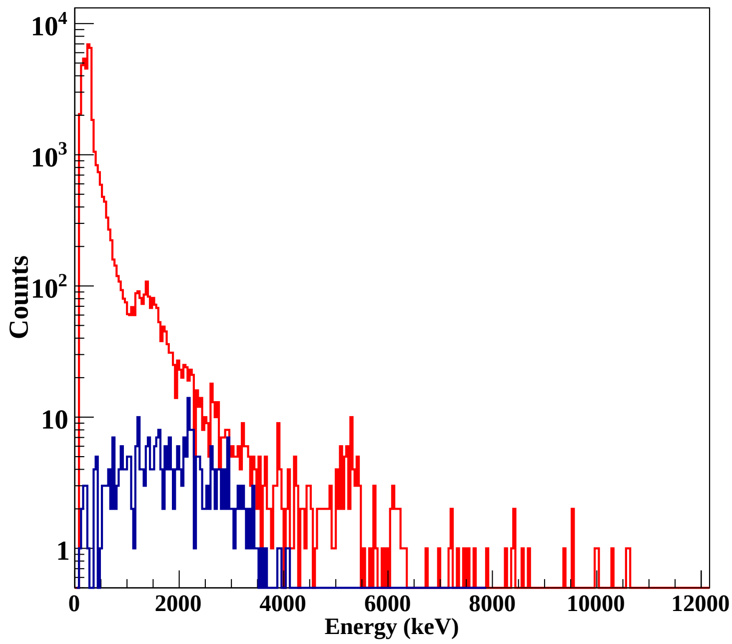

Figure 5.5: The energy deposition of all charge particles spectrum(Red) for PAD4 (505) detector overlaied with the proton spectrum (Blue) obtained from projection of proton patch in Fig 5.1 projected on thin PAD4 detector.

and PADs, one can easily obtain low energy anti-coincidence proton from both thin (DSSD4 and DSSD6) detectors in laboratory frame which is shown in Fig 5.8. By applying anti-coincidence condition between thin DSSDs and corresponding PADs, we ensured that low energy protons deposited its full energy in thin DSSDs not in PADs.

Fig 5.9 represents the overlay of the total anti-coincidence spectrum with the individual anti-coincidence spectrum obtained from DSSD4 and DSSD6 in lab frame.

Now we have added high energy coincidence proton spectrum with the low energy anti-coincidence proton sepctrum. Therefore we obtained total proton spectrum in laboratory frame which is shown in Fig 5.10.

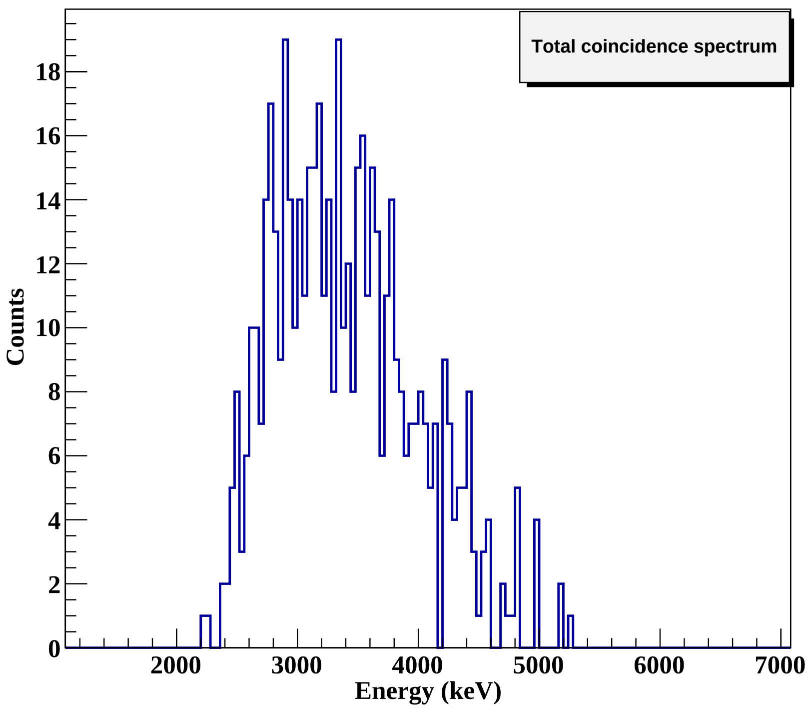

Figure 5.6: Total coincidence high energy proton spectrum in lab frame.

5.3 Proton unbound states of ^{115}Xe in centre of mass frame

To reproduce the proton unbound state of ^{115}Xe first we had to transform the total proton spectrum from laboratory frame to centre of mass frame and then we added 3.31 MeV with the proton spectrum in centre of mass frame.

At first we have transformed the high energy coincidence proton spectrum from laboratory frame to centre of mass frame, which is shown in Fig 5.11. Then we transformed the low energy anti-coincidence proton spectrum from laboratory frame to centre of mass frame, which is shown in Fig 5.12. After that We added these two spectra to reproduce the proton unbound state of ^{115}Xe, which is shown in Fig 5.13

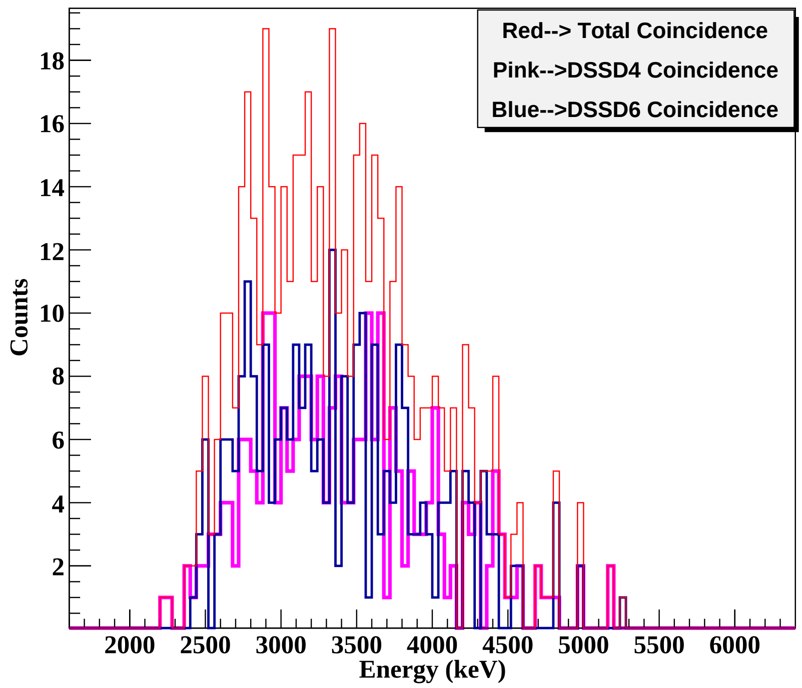

Figure 5.7: Overlay of the total coincidence spectrum with the individual coincidence spectrum obtained from DSSD4-PAD4 and DSSD6-PAD6 telescope configuration in lab frame.

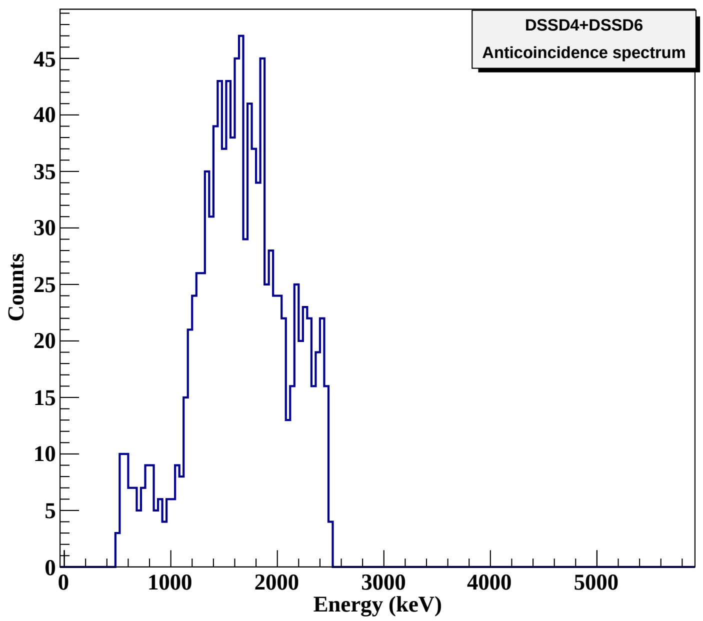

Figure 5.8: Total anti-coincidence low energy proton spectrum in lab frame.

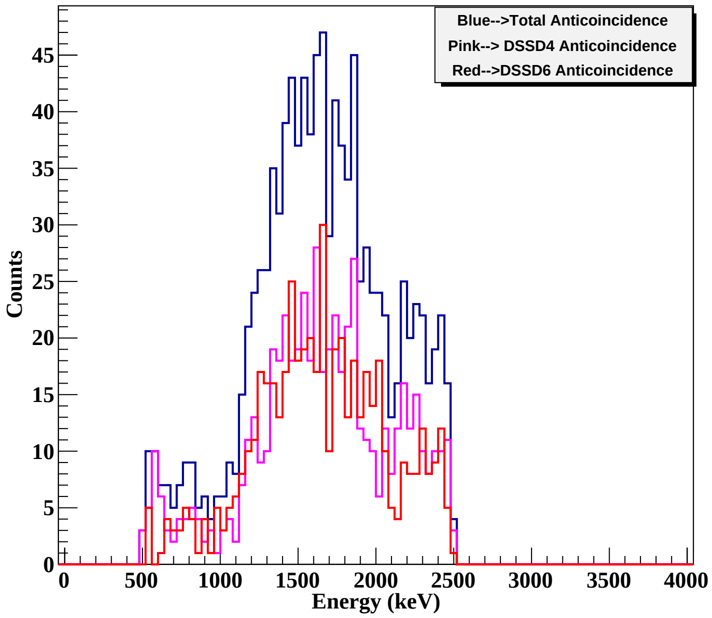

Figure 5.9: Overlay of the total anti-coincidence spectrum with the individual anti-coincidence spectrum obtained from DSSD4 and DSSD6 in lab frame.

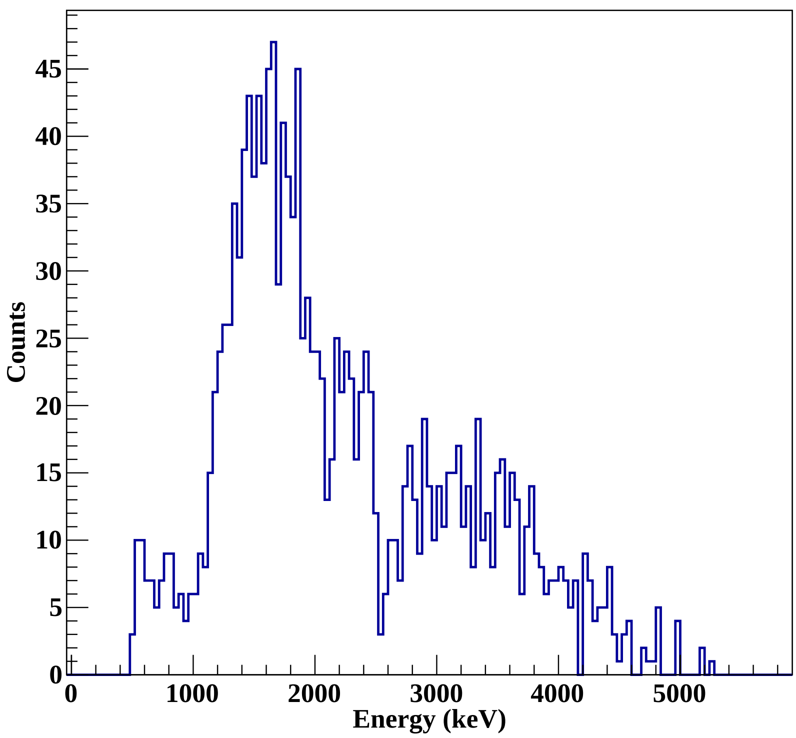

Figure 5.10: Total proton spectrum in lab frame.

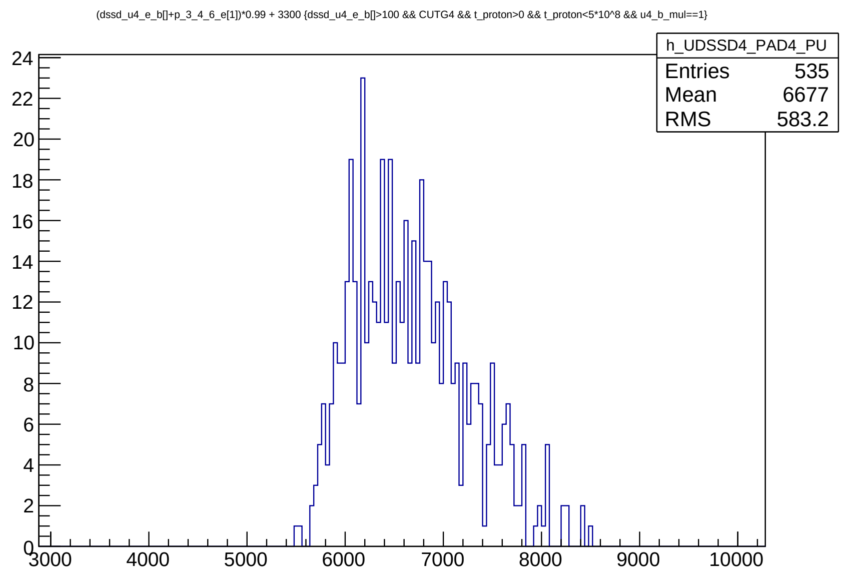

Figure 5.11: High energy proton unbound state of ^{115}Xe.

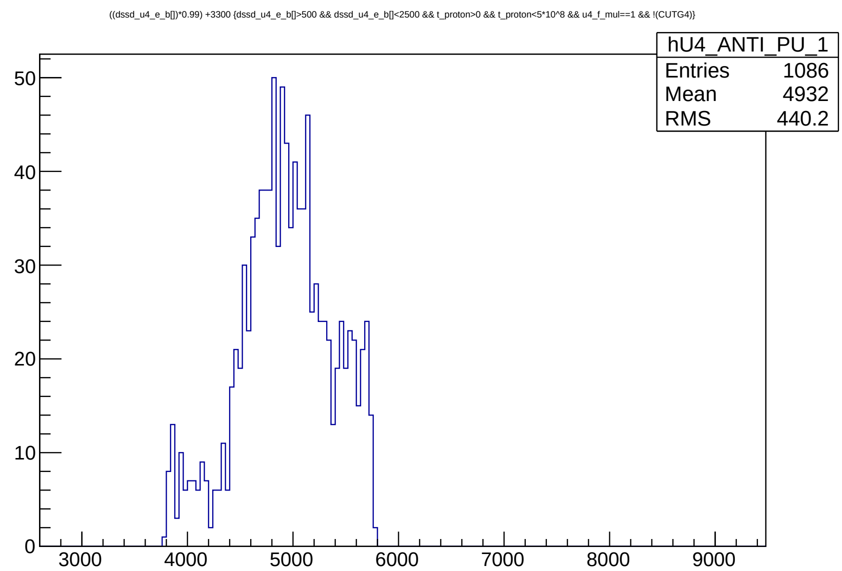

Figure 5.12: Low energy proton unbound state of ^{115}Xe.

5.4 Alpha spectrum

The alpha separation energy of ^{115}Xe is 2.506 MeV. Thus the expected energy of decaying alpha could be from 2.5 MeV to 11.47 MeV considering EC process. By applying proper anti-coincidence condition between the thin DSSDs and corresponding PAD detectors, the energy deposition up to 9 MeV by the alpha particles can be

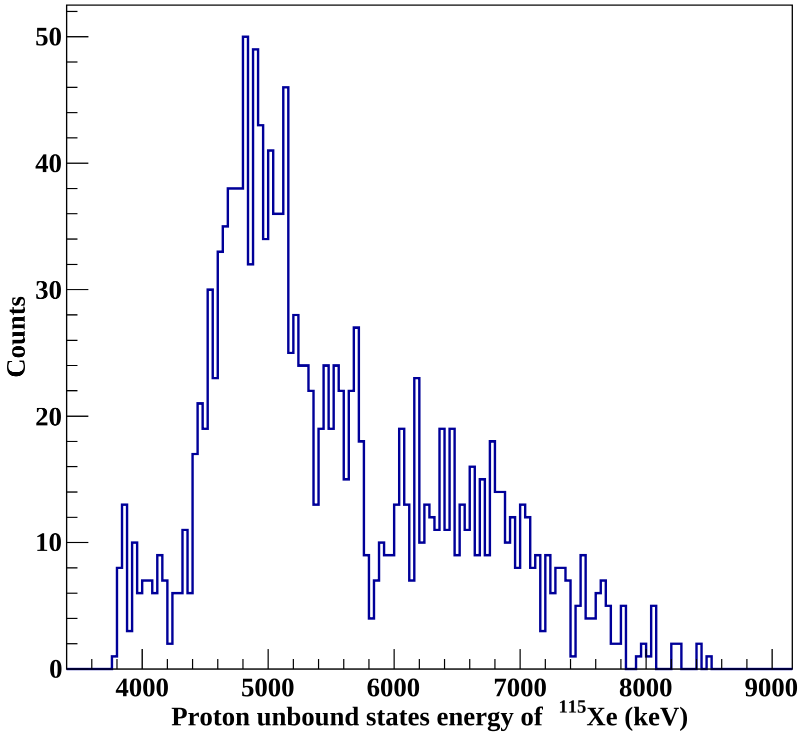

Figure 5.13: Total proton unbound state of ^{115}Xe.

obtained. The analysis of the higher energy alpha spectrum from the thick DSSDs are rather simple. Since the delayed proton energy from ^{115}Cs decay can be up to 5.86 MeV. So the energy spectrum above 6 MeV from the thick DSSDs (DSSD2 and DSSD5) (with t-proton as 5 s) can be considered as a alpha spectrum in laboratory frame. Two peaks with statistically significant at energies, 7.7 (0.422) MeV and 11.3 (0.429) MeV have been observed in Fig 5.14. These states can be considered as the alpha cluster states of the daughter nucleus. The measured spectrum has been further transformed in ^{115}Xe reference frame and the alpha separation energy has been subtracted for obtaining the excited states. These states are corresponding to the alpha-unbound states at 4.9 (0.4) MeV and 8.3 (0.4) MeV, respectively. The widths of those states are mentioned in the brackets of respective states after convolution of detector resolution.

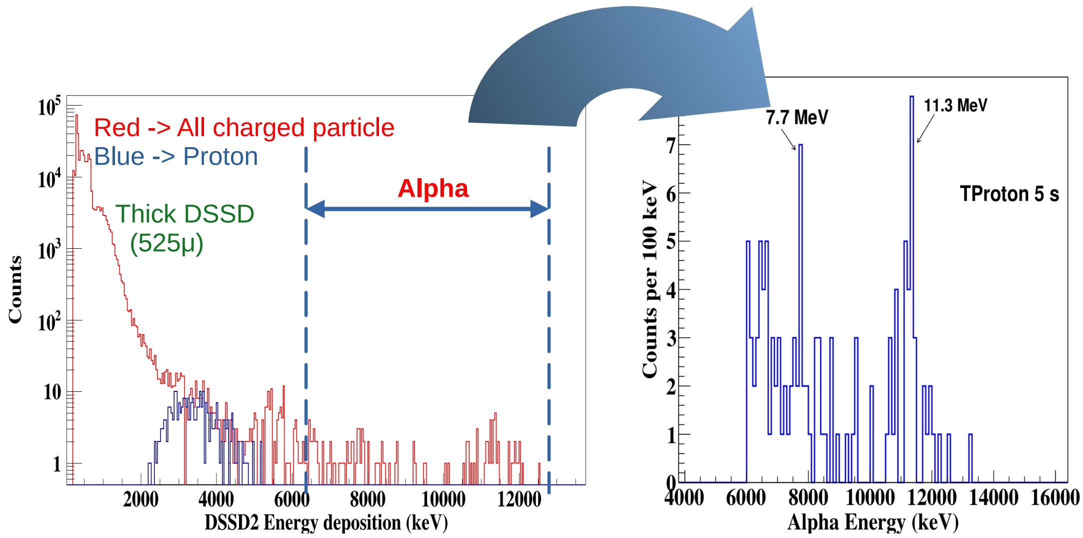

Figure 5.14: Delayed Alpha spectrum.

Chapter 6

Result and Discussion

6.1 Determination of half-life of ^{115}Cs

The half-life of ^{115}Cs has been obtained from the time distributed protons spectrum. Fig 6.1 shows time distribution of delayed protons which were obtained from the banana-cut of DSSD4-PAD4 coincidence spectrum in Fig 5.1 (chapter 5). To obtain the decay half-life of ^{115}Cs, the time distributed proton spectrum is fitted with the exponential decay function $N = N_0 e^{-\lambda t}$ which is shown in Fig 6.1. The obtained half-life of ^{115}Cs is 1.03(10) sec [56]. The previous reported value was 1.4(8) sec [55].

The spin and parity of the ground state of ^{115}Cs is not known. The ground state spin of neighboring ^{113}Cs is the $3/2^+$. The ^{117}Cs has two isomeric states with half lives and spin-parities as : 8.4(6) s; $9/2^+$ and 6.5(4) s; $3/2^+$. The ^{119,121,123}Cs also have an isomeric state close to the ground state. From present experimental data analysis, it is observed that ^{115}Cs after electron capture and/or β^+ decay, populates the daughter nucleus, ^{115}Xe into three different types of excited states. Those states

Table 6.1: Different methods for the determination of half-life of ^{115}Cs.

Different methods for the determination of half-life of ^{115}Cs		
Taken from	Half-life	Method
Present analysis	1.03(10) sec	Delayed proton distribution
Previous litreture [55]	1.4(8) sec	Beta decay

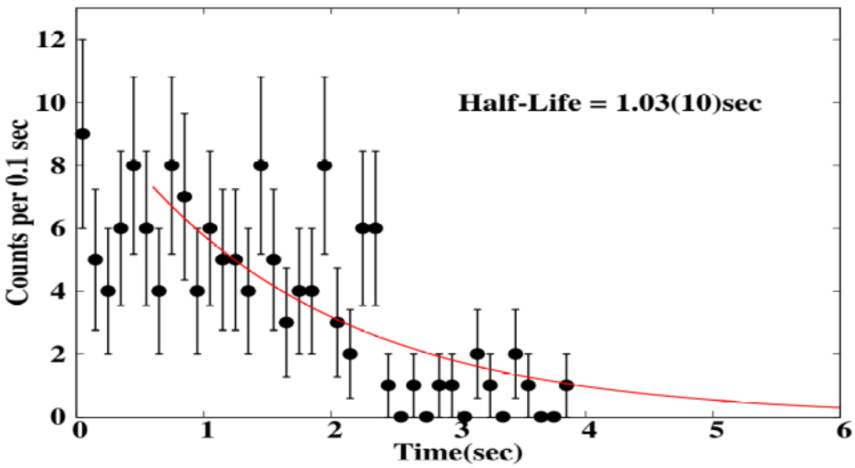

Figure 6.1: The time distribution of delayed proton events obtained after decay of ^{115}Cs from present experiment. The time distributed spectrum has been fitted with $N = N_0 e^{-\lambda t}$ and half-life was obtained.

further decay by either γ-rays or by emitting one proton, two protons and α or heavy cluster(s).

6.2 γ-ray spectra with different conditions

Fig 6.2 shows the γ-ray spectrum, obtained from all four clover calibrated add-back data during ^{115}Cs run. All the γ-ray spectra are shown with 2 keV binning. As evident from the spectrum, many background γ-ray are also present. In the present experimental data, apart from the natural background γlines, a strong with energy of 336 keV has been observed. This γ-ray is due to decaying from isomeric state of ($T_{1/2}$ = 4.48 h) to the ground state of ^{115}In [1].

Fig 6.3 and 6.4 show the background γ-rays which were present during the experiment in the beam hall. We have identified the sources of those γ-ray, presented in Fig 6.3 and 6.4.

Those natural background γ-rays have been subtracted from the γ-ray spectrum of Clover-array during ^{115}Cs runs. The peak at 1461 keV is produced by the decay of the long-lived naturally occurring isotope ^{40}K. The 1461 keV γ-line has been considered for normalization to obtain background subtracted γ-ray spectrum. Fig

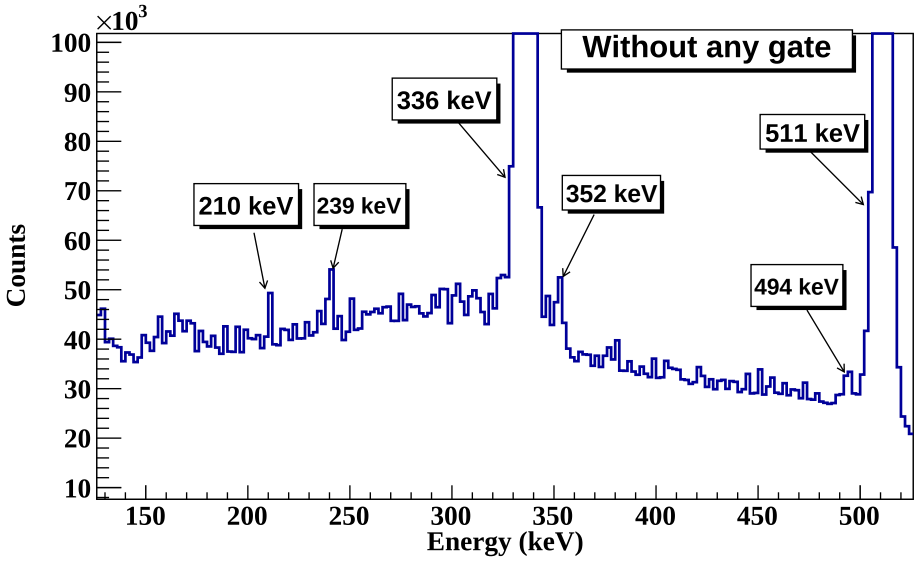

Figure 6.2: γ-ray spectrum obtained from addition of all four Clover calibrated data during experiment [IS545] (^{115}Cs) without any condition.

6.5 shows the background subtraction γ-ray spectrum for ^{115}Cs decay. But 336 keV gamma is also present in background subtracted γ-ray spectrum. Therefore, it can be concluded that the 336 keV γ-ray is mainly coming from the beam contamination. To eliminate this contamination β-gating condition has been applied and β-gated γ-ray spectrum has been produced, as shown in Fig 6.6. Here we have done this β-gate from DSSD5. In that figure, the 336 keV is absent. So, the main contaminant with the beam of ^{115}Cs was ^{115}In. But that nucleus (^{115}In) has no delayed charge particle branch.

6.3 Bound states of ^{115}Xe

Over the past few years, the study of excited states in very neutron-deficient nuclei just above the Z=50 shell closure draws significant attention. The high-spin states on neutron-deficient ^{115}Xe was studied via fusion evaporation reaction. Several bands of high spin states in ^{115}Xe were populated using ^{60}Ni(^{58}Ni, 2pn) ^{115}Xe reaction [63]. The ^{58}Ni heavy-ion beam with energy 250 MeV was obtained from the Tandem Accelerator Superconducting Cyclotron (TASCC) facility at the Chalk

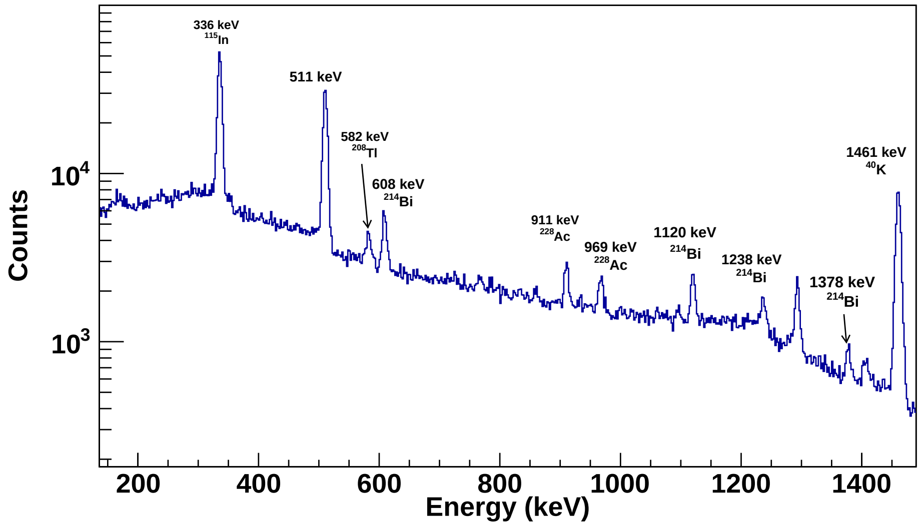

Figure 6.3: The background γ-rays at the experimental hall(low-energy part).

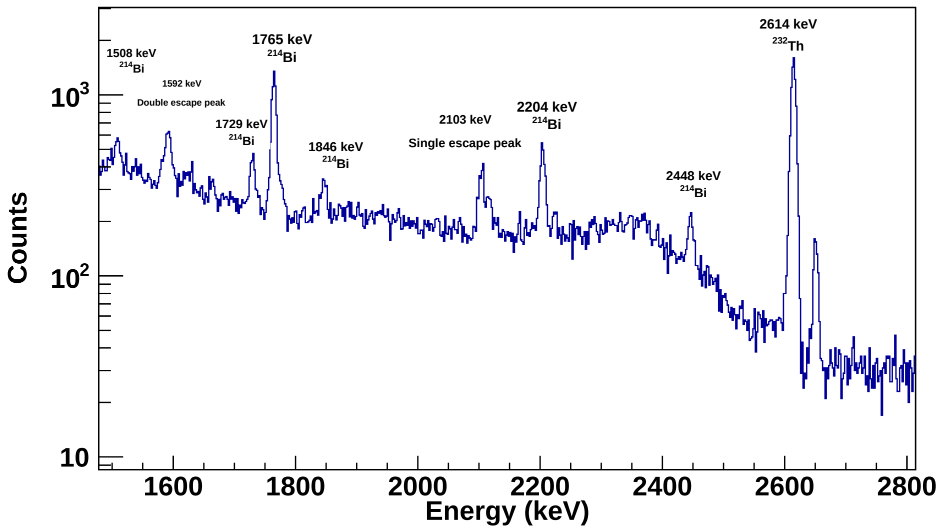

Figure 6.4: The background γ-rays at the experimental hall (high energy part).

River Laboratories, Canada. The $\gamma-\gamma$ Coincident data were taken using the 8π spectrometer, consisting of 20 Compton-suppressed HPGe detectors plus a 71-element BGO inner-ball calorimeter. The decaying transitions were assigned to ^{115}Xe. Fig 6.7 shows the corresponding level scheme of ^{115}Xe, obtained from that work.

The ground state spin and parity of ^{115}Xe is tentatively known as the $(5/2^+)$ [62]. In present experimental data, after decay the populated bound states of daughter nucleus are low-spin states. The reasons behind it are the limitation of the efficiency of clover array and limited beam time. Thus only allowed decay transitions are

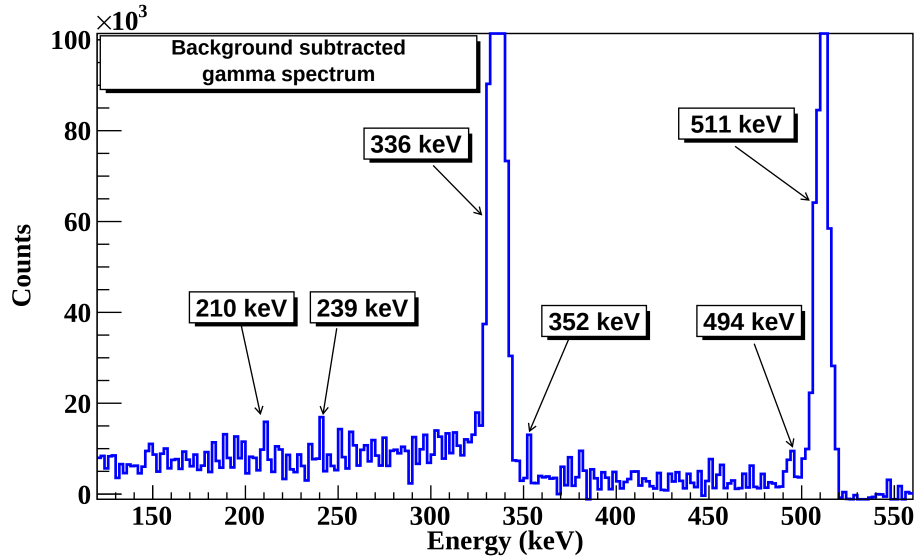

Figure 6.5: Background subtracted γ-ray spectrum from ^{115}Cs decay.

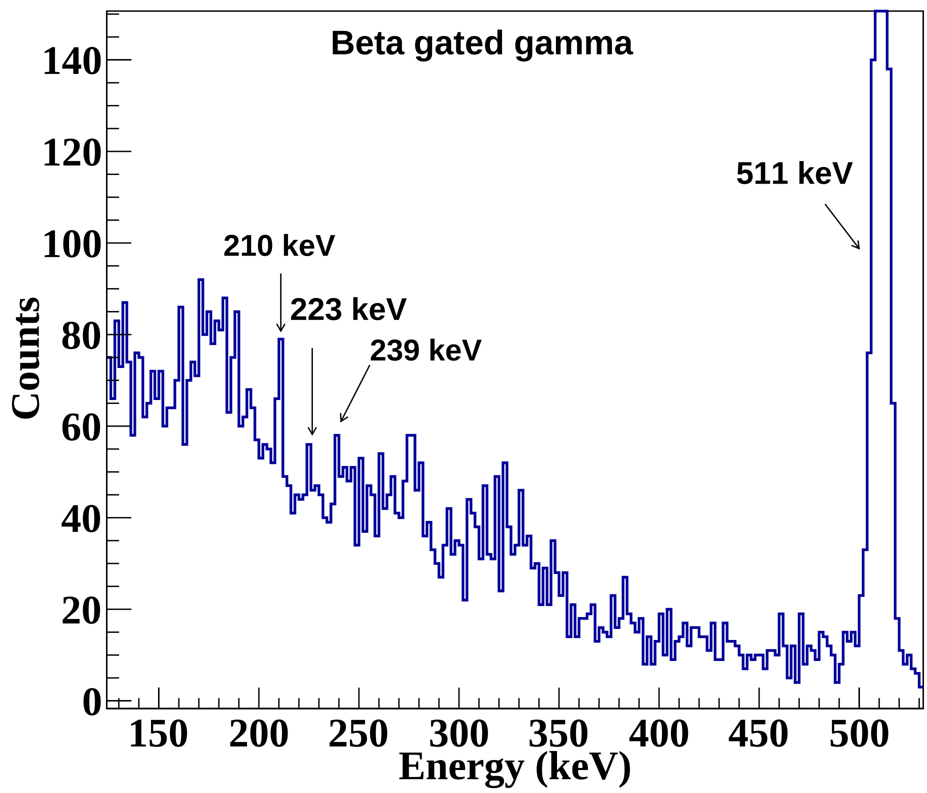

Figure 6.6: β-gated γ-ray spectrum from ^{115}Cs decay.

observed for bound states of the daughter nucleus. The β-gated γ-ray spectrum with the t-proton gate as 5 s shows several characteristic γ-rays of ^{115}Xe, such as

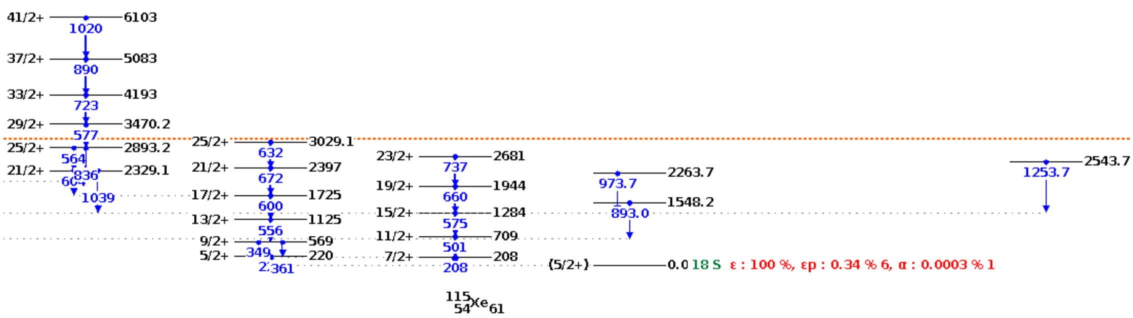

Figure 6.7: level scheme of ^{115}Xe [1].

210(2) keV, 223(3) keV, 239(3) keV and 349(5) keV. The delayed γ-transitions can be the members of three strongly populated bands. These bands were originated from $\nu(g_{7/2}/d_{5/2})$ and were studied in detail using in beam γ-ray spectroscopy and fusion evaporation reaction [63]. The observed delayed γ-ray transitions from present experiment could be corresponding to the transitions 208(1) keV ($7/2^+ \rightarrow (5/2^+)$), 220(1) keV ($5/2^+ \rightarrow (5/2^+)$), 349(1) keV ($7/2^+ \rightarrow (5/2^+)$), reported earlier [63], shown in Fig 6.6. Though the excited state with energy 241(2) keV ($11/2^-$) was reported but no decay transition was mentioned [63]. The observed γ-ray transition with energy of 239(3) keV could be decaying from 241(2) keV ($11/2^-$) to ($5/2^+$) [63]. This is possible for the nucleus with octupole deformation. Fig.6.6 shows the delayed β^+ gated γ-ray spectrum and some of the observed γ-ray transitions from ^{115}Xe are labeled with the energies. It is evident from the Figure below, many other delayed γ-ray transitions are there.

However, to establish the new γ-ray transition, a detailed analysis of a data with better statistics is necessary. Here we are more focused on the unbound states, observed by the exotic decay modes. From present data, it is clear that the daughter nucleus was populated to the $7/2^+$ with major intensity (24$\pm$ 8%).

6.3.1 $\gamma - \gamma$ coincidence spectra

Fig 6.8 shows the 210(2) keV γ gated coincidence γ-ray spectrum, obtained from present experimental data. It is evident from the figure that 160 keV, 302 keV and 1253 keV γ-rays are in coincidence with 210(2) keV γ-line. It was reported by E.S.Paul et al. [63] that 1253 keV γ-line is in coincidence with the γ-ray of 634 keV $(19/2^- \rightarrow (15/2^-))$ and 414 keV $(15/2^- \rightarrow (11/2^-))$. But we obtained that 1253 keV γ is in coincidence with 210 keV γ (see Fig 6.8). Similarly 303 keV γ- gated coincidence spectrum is shown in figure 6.9. In that gated spectrum, The γ-rays with energies of 56 keV, 117 keV, 190 keV and 210 keV gammas are in coincidence with 302 keV γ line. But 160 keV γ-ray is not in coincidence with 302 keV γ. So, we can conclude that 160 keV and 302 keV γ-lines are in parallel but both are coincidence with 210 keV γ. Thus few new transitions of ^{115}Xe have been observed in the present delayed γ-ray spectroscopy. A future experiment with more statistics and larger clover array may provide a significant information of low-lying and low-spin states of ^{115}Xe. That may provide valuable information about the intricacies of the structure of very neutron deficient nucleus.

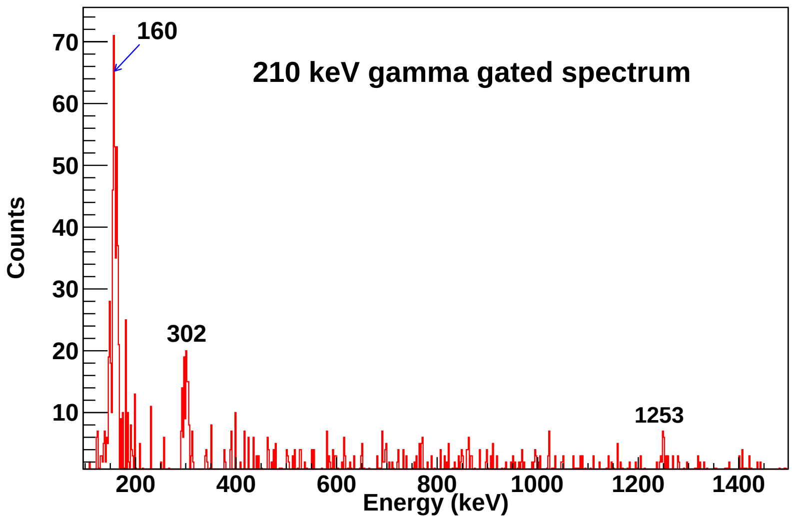

Figure 6.8: 210(2) keV γ-ray gated γ-ray spectrum from present experiment.

6.4 Unbound resonance states

The primary motivation of studying exotic decay mode of the nuclei near the drip-line is the population of the highly excited states above the particle threshold(s). By using very low energy (few tens of keV) RIB, one can populate the excited states up

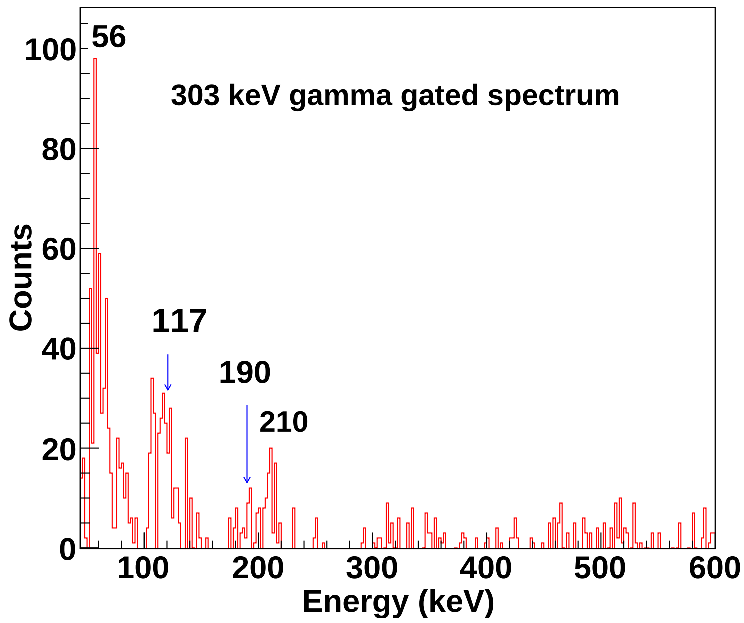

Figure 6.9: 302(2) keV γ-gated γ-ray spectrum from present experiment.

to 8.96 MeV (in present situation). Till today, no particle unbound states of ^{115}Xe has been reported [1]. The unbound states of the daughter nucleus ^{115}Xe, have been reconstructed from the energy spectrum of delayed proton and alpha from present experimental data [58]. More details are being described below.

6.4.1 Proton unbound states

The delayed proton spectrum for higher energy has been obtained by addition of the deposited energies in the thin DSSD and the corresponding PAD detectors, obtained in coincidence mode. On the other hand low energy protons (<2.5 MeV) were fully stopped in the thin DSSD which has been obtained from the thin DSSD spectrum in anti-coincidence mode with the PAD detector. This low energy spectrum has been added to the higher energy part. The delayed proton spectrum has been converted into the reference frame of ^{115}Xe and the proton separation energy has been added to extract the proton unbound excited states of ^{115}Xe. Now Proton unbound States of ^{115}Xe has been obtained by fitting with peaks via χ^2 minimization [58], which are shown below. Fig 6.10 represents the proton unbound states of ^{115}Xe obtained

Table 6.2: χ^2/ndf values for fitting delayed proton energy spectrum (corrected with proton separation energy) considering different number of peaks.

Different peak fitting		
Figure	Number of peaks	χ^2/ndf value
5.4	3	2.1
5.5	4	1.8
5.6	5	1.7
5.7	6	1.6

by fitting three peaks via χ^2 minimization. Similarly Fig 6.11 represents the proton unbound states of ^{115}Xe obtained by fitting four peaks via χ^2 minimization. Fig 6.12 and Fig 6.13 represent the proton unbound states of ^{115}Xe obtained by fitting five and six peaks respectively via χ^2 minimization.

Table 6.2 shows the different χ^2/ndf values for different fittings for proton unbound states of ^{115}Xe. We have selected Fig 6.13 as the best fitted proton unbound states of ^{115}Xe due to its lower χ^2/ndf value.

Fig 6.14 represents the proton unbound excited states obtained from present data without efficiency correction [58].

The spectrum has been fitted with multiple Gaussian functions with variable widths via χ^2 minimization. This fit indicates the presence of six unbound states. The detector energy resolution has been considered to extract the widths of the states. The table 6.3 shows the energies and widths of the observed proton unbound states. The decay widths indicate that the lifetime of these states are of the order of zepto-seconds [58]. After the efficiency correction, total number of delayed protons have been considered to obtain delayed proton branch. According to our experimental data, the decay fraction of the delayed proton branch is 0.2±0.06% [58] which is more than the previously reported value of 0.07 % [55].

6.4.2 Bayesian estimation of parameters

The delayed proton spectrum has been fitted with Bayesian approach to obtain the properties of excited states [58]. This method further enables us to carry out

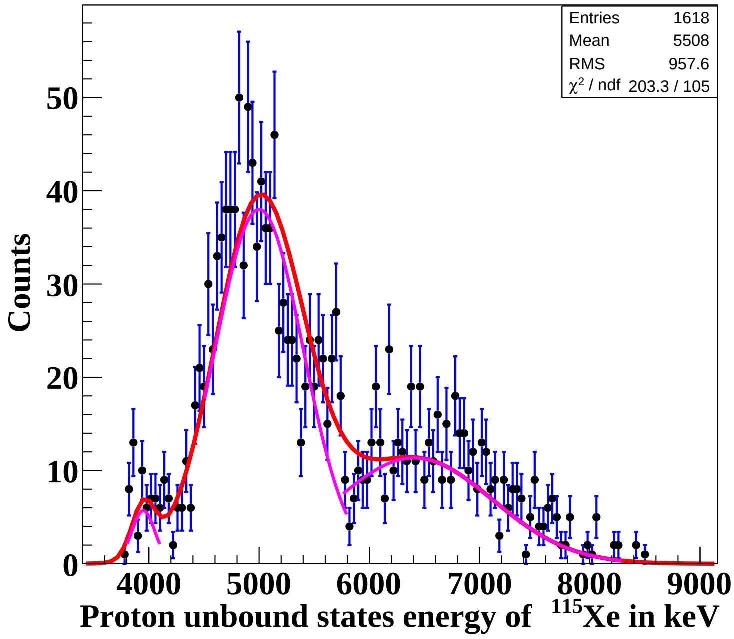

Figure 6.10: Proton unbound states of ^{115}Xe obtained by fitting three peaks via χ^2 minimization.

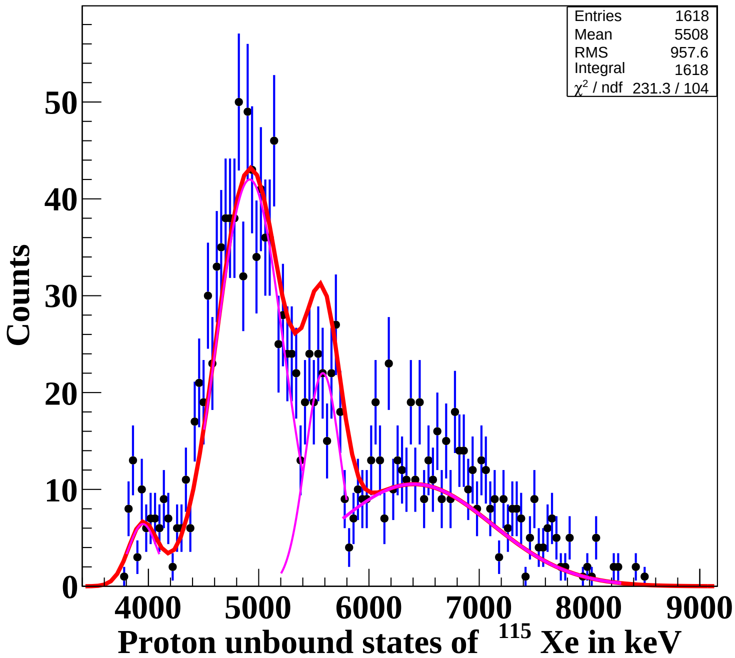

Figure 6.11: Proton unbound states of ^{115}Xe obtained by fitting four peaks via χ^2 minimization.

detailed statistical analysis of the fitted parameters. It yields joint posterior distributions of the parameters which can be used to study not only the distributions of given parameters but also to examine correlations among model parameters. This

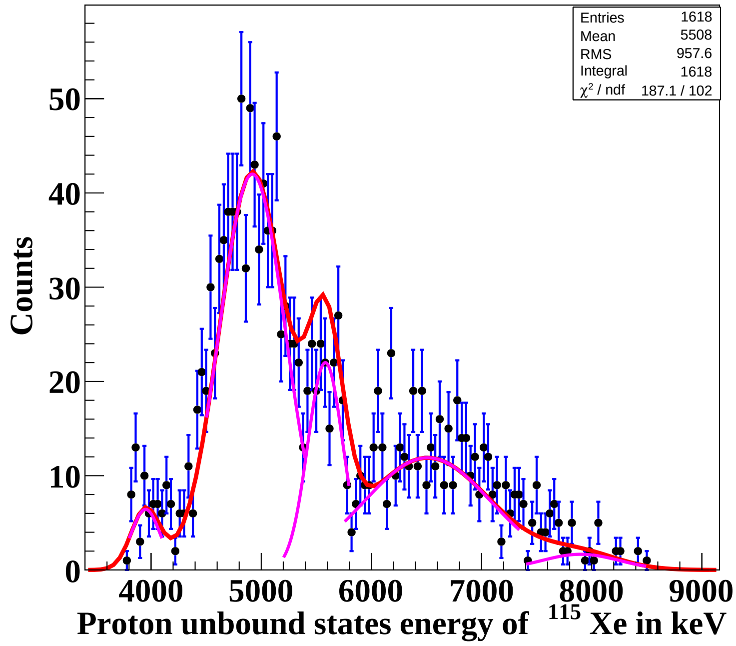

Figure 6.12: Proton unbound states of ^{115}Xe obtained by fitting five peaks via χ^2 minimization.

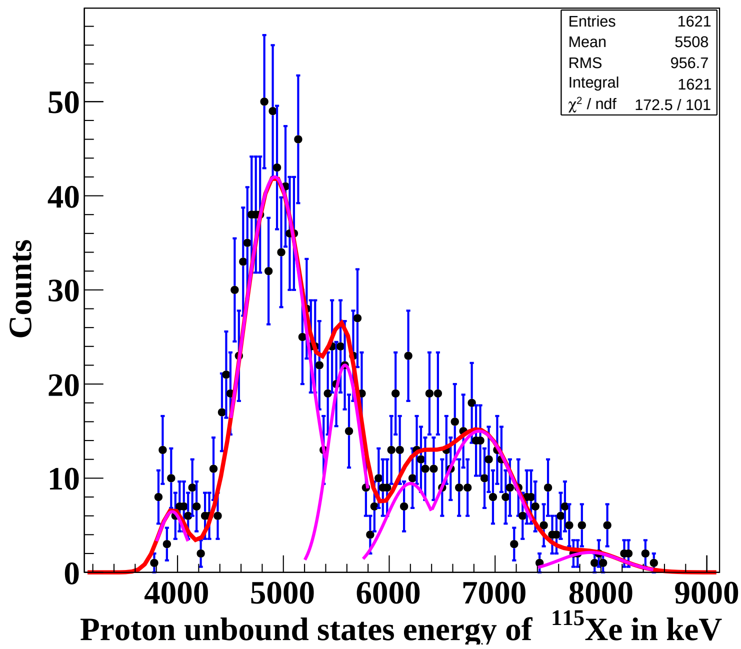

Figure 6.13: Proton unbound states of ^{115}Xe obtained by fitting six peaks via χ^2 minimization.

approach is mainly based on the Bayes theorem which states that [64],

$$P((\theta|D) = \frac{\mathcal{L}(D|\boldsymbol{\theta})P(\boldsymbol{\theta})}{\mathcal{Z}}, \tag{6.1}$$

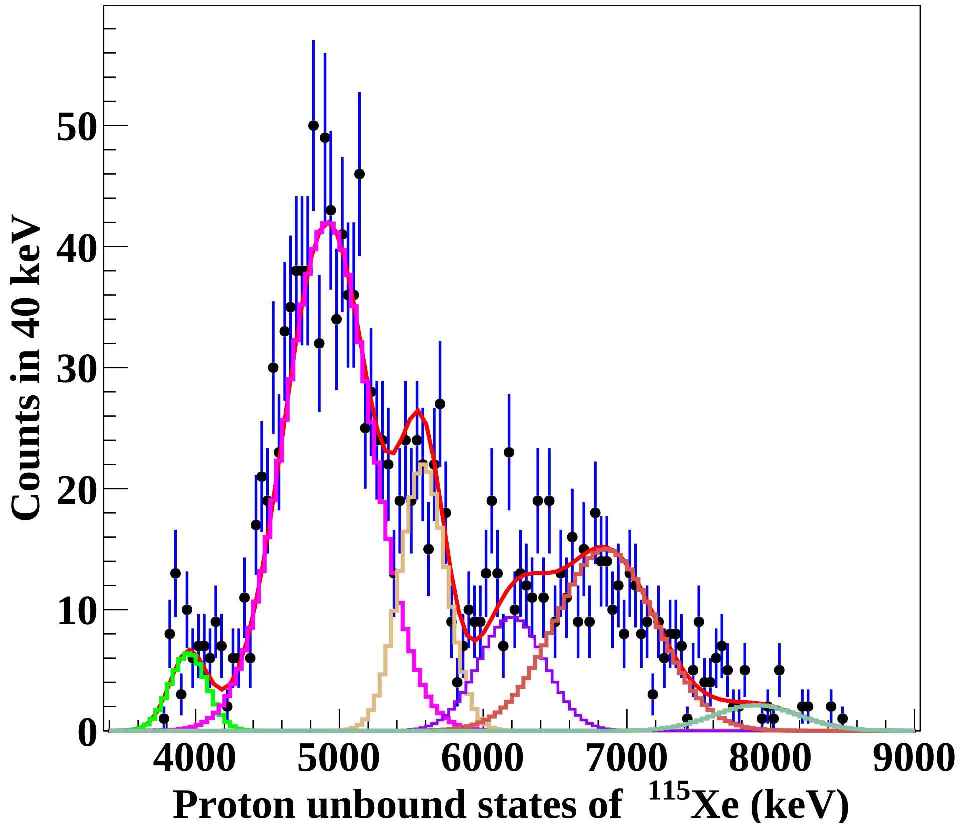

Figure 6.14: Proton unbound excited states of ^{115}Xe with individual fitted peak.

where $\boldsymbol{\theta}$ and D denote the set of model parameters and the fit data, respectively. The $P(\boldsymbol{\theta}|D)$ is the joint posterior distribution of the parameters, $\mathcal{L}(D|\boldsymbol{\theta})$ is the likelihood function, $P(\boldsymbol{\theta})$ is the prior for the model parameters and $\mathcal{Z}$ is the evidence. To populate the $P(\boldsymbol{\theta}|D)$, we implement a nested sampling algorithm by invoking the Pymultinest nested sampling [65] in the Bayesian Inference Library [66]. We use Gaussian likelihood function defined as,

$$\mathcal{L}(D|\boldsymbol{\theta}) = \prod_j \frac{1}{\sigma_j\sqrt{2\pi}} e^{-(D_j - M_j(\boldsymbol{\theta}))^2/2\sigma_j^2} \tag{6.2}$$

where the index j runs over all the data. D_j and σ_j are the data and corresponding uncertainties, respectively. The M_j are the model values that are obtained using the sum of the six Gaussian with their mean m_j and widths s_j, $(i = 1, 2, ...6)$.

Fig 6.15 represents the delayed proton energy spectrum fitted with the Bayesian

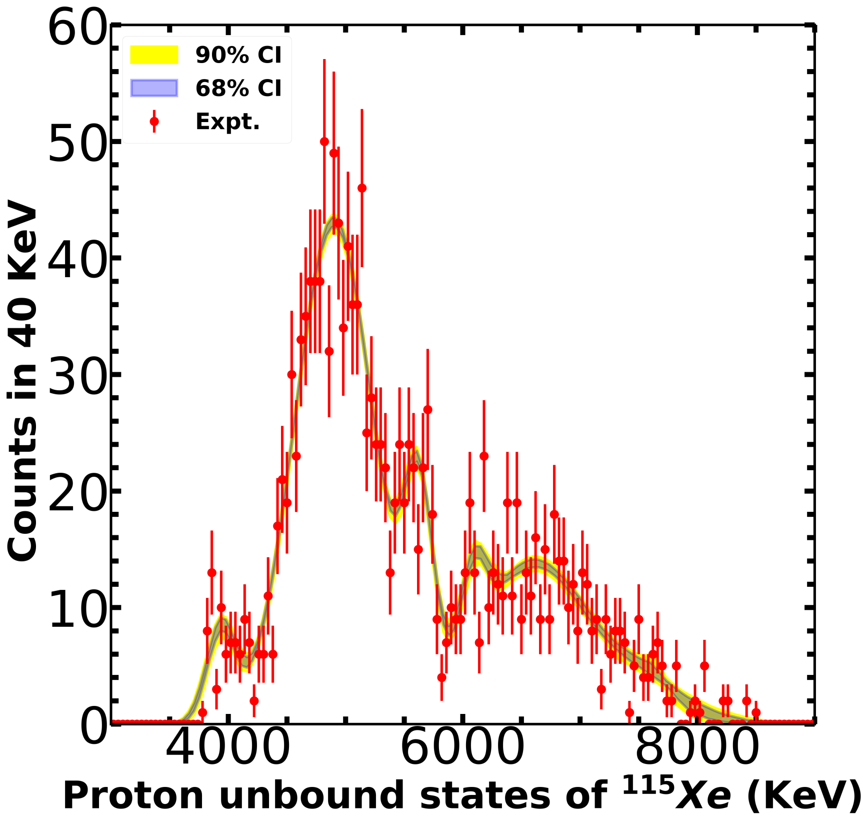

Figure 6.15: Proton unbound excited states of ^{115}Xe using Bayesian analysis.

analysis. The energies and widths of those states from the Bayesian analysis are 3.9(0.29) MeV, 4.9 (0.79) MeV , 5.6 (0.29) MeV , 6.1 (0.26) MeV, 6.6 (1.1) MeV, 7.5 (0.84) MeV. These values are very similar to those obtained by χ^2 fitting except the last few higher energy states. The higher energy proton unbound states have a broad energy distribution according to the Bayesian analysis. These values are given within the bracket in Table 6.3.

Fig 6.16 shows the corner plot of the Bayesian analysis. It shows the correlation of various parameters which are energies of the states (m_i) and related widths (s_i , i = 1, 2, 3, 4, 5, 6). The diagonal plots show the univariate sample distribution of the parameters. Posterior mean and standard deviation are indicated in the figure. The off-diagonal plots show the KDE (Kernel density estimates) estimations of the bi-variate posterior distributions of the parameters. As it is evident from the Fig.6.16, the errors obtained by fitting the energies of the proton unbound states are only few

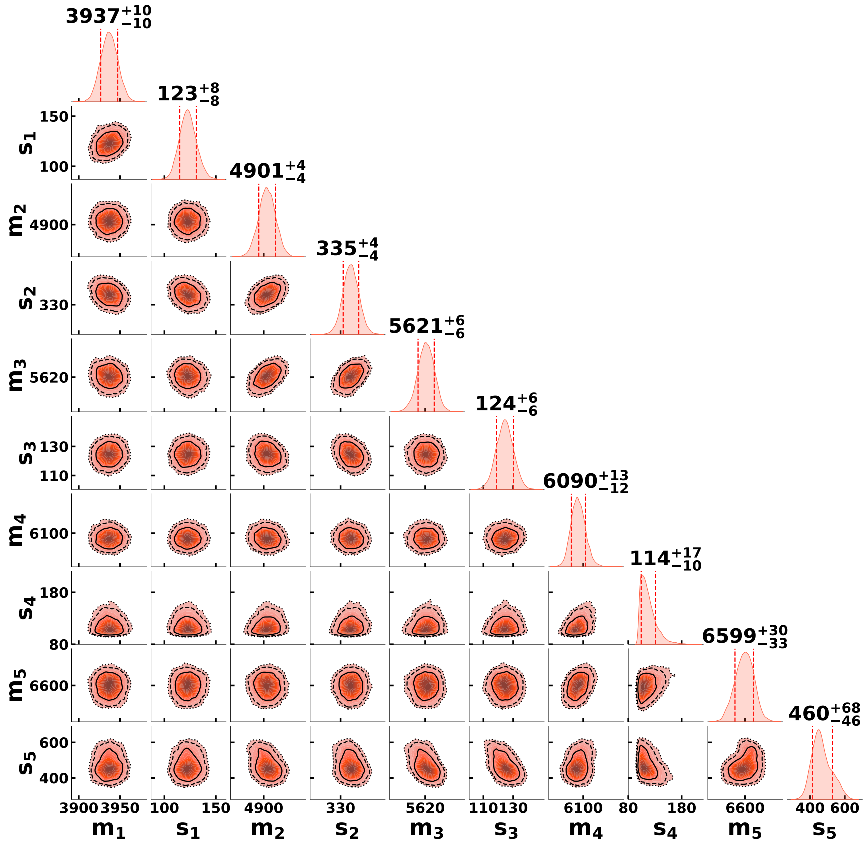

Figure 6.16: The corner plot of the Bayesian analysis with the correlation among the parameters.

keV (∼ 0.1 %) except for the higher lying states (∼ 1 %). On the other-hand, the errors in the fitted widths of the unbound states are more (1-13%). It is important to note from the fits that the energy of a particular state is correlated with the widths of the neighboring states. This observation emphasizes the fact of overlapping widths of the states. On the other hand the lifetime of the states is of the order of zepto-seconds. The values corresponding to Bayesian analysis are within the third bracket in Table 6.3. Though the results, obtained from the standard method (χ^2 minimization) and the Bayesian analysis are somewhat similar but later method is free from any assumption on distribution of parameters which is more acceptable. The above information on the proton unbound states can be a valuable input for

Table 6.3: Unbound states of ^{115}Xe, populated after decay of the ^{115}Cs. Both fitted the spectrum via χ^2 minimization and the Bayesian method (mentioned in the parenthesis) are shown.

Unbound-states of ^{115}Xe				
Energy of the unbound states (MeV)	Width of the unbound states (keV)	Measured life time (zepto-seconds)	Branching %	Obtained from this expt. via delayed
3.9 [3.9]	289 [285]	2.3 [2.3]	0.006(1)	proton
4.9 [4.9]	702 [787]	0.9 [0.8]	0.10(1)	proton
4.9	422	1.6	0.005(1)	alpha
5.6 [5.6]	364 [290]	1.8 [2.3]	0.030(2)	proton
6.2 [6.1]	532 [262]	1.2 [2.5]	0.020(2)	proton
6.8 [6.6]	817 [1079]	0.8 [0.6]	0.040(5)	proton
7.9 [7.5]	690 [841]	1.0 [0.8]	0.005(1)	proton
8.3	429	1.5	0.006 (2)	alpha

understanding an open quantum many body system calculation. But at present, we have limitation of no core shell model up to the nuclei with A$\sim$ 76 [67]. To understand the experimental data qualitatively, we have used Nilsson model predictions. Typical deformation in this region is around $\beta_2 \sim 0.28$ [68]. The odd proton in the ground state of ^{115}Cs may occupy either [404]$9/2^+$ or [422]$3/2^+$. On the other hand, if the ground state of ^{115}Cs is oblate, the tentative state which can be occupied by the valence proton is [404]$7/2^+$ or [413]$5/2^+$. The odd neutron of ^{115}Xe may occupy [532]$5/2^-$, or [411]$3/2^+$ or [404]$9/2^+$. The ground state spin and parity is known tentatively as $(5/2^+)$ [55]. According to the present experimental observation, after decay it populates the bound state, $7/2^+$ with a large branching ratio (24$\pm$8%). So the probable ground state spin of ^{115}Cs can be $7/2^+$ or $9/2^+$. It may be noted that with deformation ($\beta_2 \sim 0.28$) and N = 4 positive parity states, 7-8 MeV excited states can not be obtained from the Nilsson prescription. A higher deformation (β_2 $\sim$ 0.5- 0.6) is necessary to obtain the state(s) around 7-8 MeV of excitation.

Table 6.4: Branching ratios of the delayed proton and alpha of ^{115}Cs.

Branching ratios	
Delayed Branch	Branching in %
proton	0.2±0.06
alpha	0.01±0.005

6.4.3 Cluster-unbound states

The decay study of ^{115}Cs is fascinating as the alpha breakup threshold (S_α = 2.8 MeV) [62] is lower than that for one proton (S_p = -100 keV). The situation is similar for the alpha unbound daughter nucleus, ^{115}Xe. Thus a possible alpha cluster structure of the daughter nucleus may exist. Hence a detailed study of the quasi-bound alpha states will be an important aspect to investigate. The ground state of the neighboring nucleus, ^{113}Xe has a known direct alpha decay probability [69]. On the other hand for ^{114}Cs in addition to the delayed proton and alpha, a direct alpha decay branch was observed [70]. ^{115}Xe ($t_{1/2}$ = 18 s) has a alpha decay possibility. The alpha separation energy of ^{115}Xe is 2.506(14) MeV [57]. Thus the expected energy of decaying α could be from 2.5 MeV to 11.47 MeV considering EC process. By applying proper anti-coincidence condition between the thin DSSDs and corresponding PAD detectors, the energy deposition up to 9 MeV by the alpha particles can be obtained. The analysis of the higher energy alpha spectrum from the thick DSSDs are rather simple. Since the delayed proton energy from ^{115}Cs decay can be up to 5.86 MeV. So the energy spectrum above 6 MeV from the thick DSSDs (DSSD2 and DSSD5) (with t-proton as 5 s) can be considered as a α-spectrum in laboratory frame. Two peaks with statistically significant at energies, 7.7(0.422) MeV and 11.3(0.429) MeV have been observed [58]. These states can be considered as the alpha cluster states of the daughter nucleus. The measured spectrum has been further transformed in ^{115}Xe reference frame and the alpha separation energy has been subtracted for obtaining the excited states. These states are corresponding to the α-unbound states at 4.9(0.4) MeV and 8.3(0.4) MeV, respectively [58]. The widths of those states are mentioned in the brackets of respective states after convolution of detector resolution. However, in the present experimental situation, we cannot rule out the possibility of decay of a heavy cluster, like ^{11}C, ^{8}Be etc. If 11.3 MeV energy deposition at thick DSSDs is due to ^{11}C then the energy of the unbound cluster state, ^{104}Cd$\otimes^{11}$C, is 5.6 MeV. To confirm this heavy cluster emission, further dedicated investigation is necessary. The analysis of low energy alpha spectrum is rather complex due to the low statistics and complexity of the system. Through anti-coincidence of the events between the thin DSSDs and the PADs, the alpha spectrum above 2.61 MeV would be due to delayed alpha. But a part of the threshold strength could be due to a direct α-decay from the ground state of ^{115}Xe. This part can be reduced by a t-proton gate. Even after the t-proton gate as 5 s, some strength close to the ground state of the daughter nucleus has been observed. The strength is around the energy of 23^{+42}_{-23} keV which is shown in Fig 6.17. Clearly, the width of that α-unbound state is comparable with the energy resolution of the DSSD. Thus a state of the alpha cluster close to the ground state is there. Fig 6.17 represents the schematic diagram of various decay processes of ^{115}Cs. Table 6.3 shows the energies with the widths of the observed α-cluster states of the daughter nucleus. Table 6.4 shows the measured delayed proton and alpha branching ratios of the ^{115}Cs [58].

6.4.4 Delayed two proton emission

Zel'dovich [71] proposed the possibility of emission of two protons simultaneously. Fig 6.18 shows the schematic diagram of delayed one and two proton radioactivity. H Goldanskii [72], and Janecke [73] proposed the nuclei which have possibilities of two proton radioactivity. Many scientists [74–76] studied the nuclei, ^{39}Ti, ^{42}Cr, ^{45}Fe and ^{48,49}Ni to observe the decay. More than 58 years after its theoretical proposal, two proton decay was discovered. In later experiments observation of two proton decay were reported in ^{54}Zn [77] and ^{48}Ni [78].

In the present experimental data, a search for delayed two proton has been attempted. Considering multiplicity two, two dimensional E-ΔE spectrum using

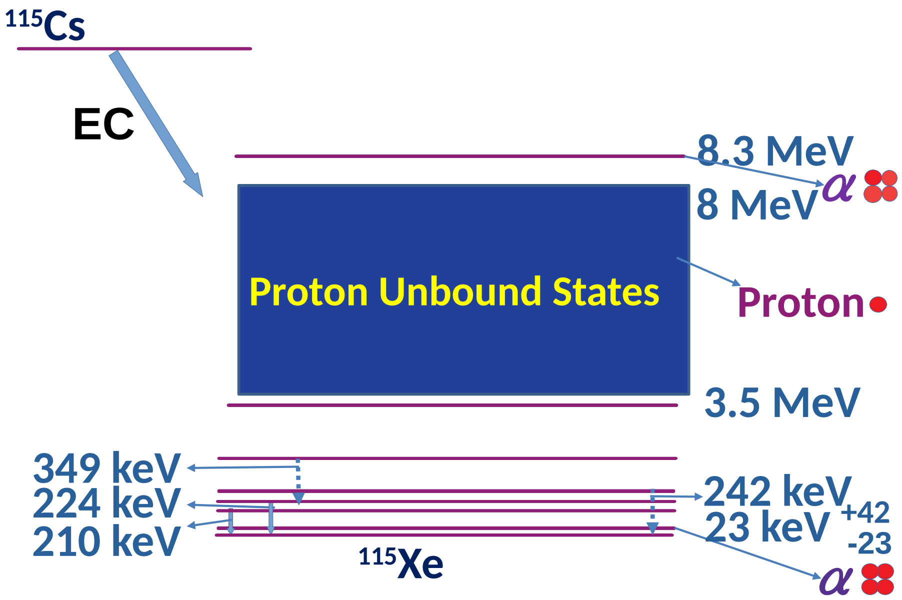

Figure 6.17: Schematic diagram of the exotic decay mode of ^{115}Cs.

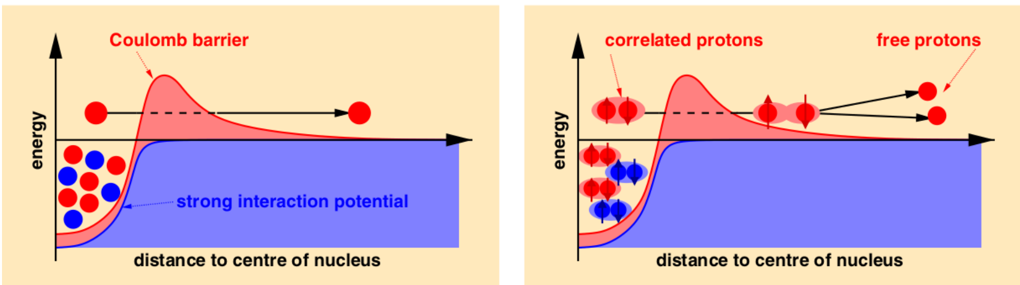

Figure 6.18: Schematic diagram of delayed one and two proton radioactivity [79].

DSSD4-PAD4 and DSSD6-PAD6 have been plotted (see fig.6.19, fig.6.20). Clearly very few events have been observed. The hit-map of these two proton are also shown in the Fig 6.21 and Fig 6.22 . We have calculated the two proton branching ratio which is less than 0.0010(5)%. However to confirm more details invetigation with better statistics is necessary.

In summary, the first detailed study of various decay modes of the proton and alpha unbound nucleus, ^{115}Cs is reported in this thesis. The bound and unbound states of the daughter nucleus, ^{115}Xe, were populated up to 8.3 MeV. Addition-

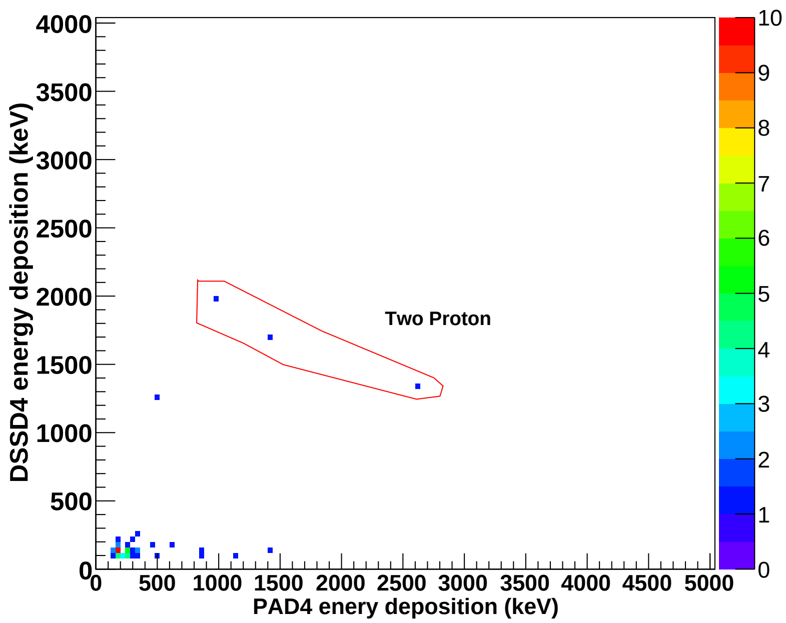

Figure 6.19: Delayed two protons spectrum from DSSD4-PAD4.

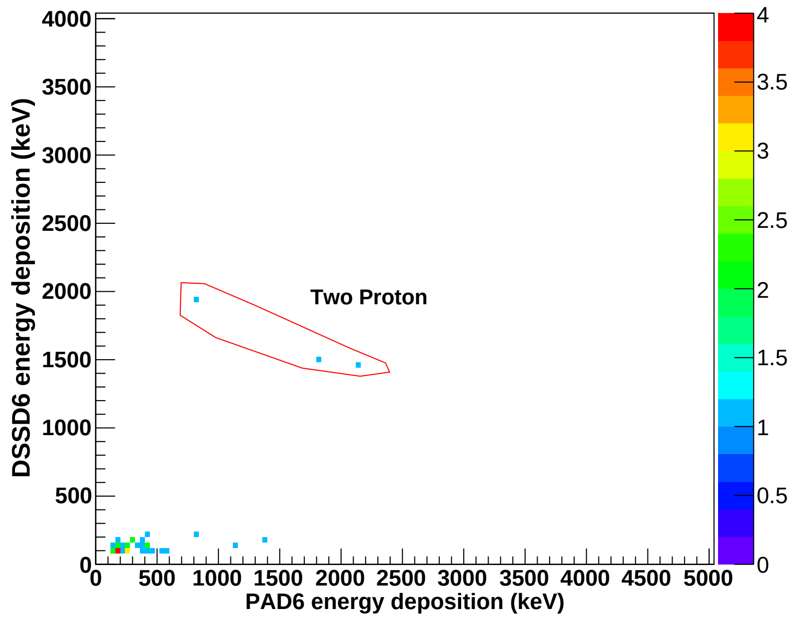

Figure 6.20: Delayed two protons spectrum from DSSD6-PAD6.

ally, the measured branching ratios of delayed proton and alpha decay for ^{115}Cs are reported. By employing the Bayesian method of analysis, several new proton unbound states have been identified, characterized by very short lifetimes of the order of zeptoseconds. These findings have the potential to constrain calculations in the open quantum shell model for heavy nuclei, providing important insights into the

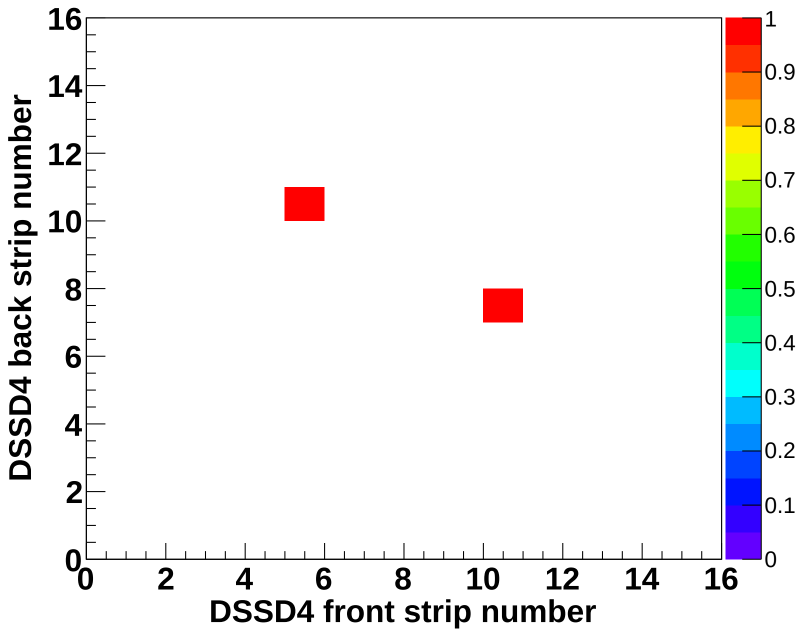

Figure 6.21: Hitmap of delayed two proton events which are obtained from the 2 dimensional plot front and back strip number of DSSD4.

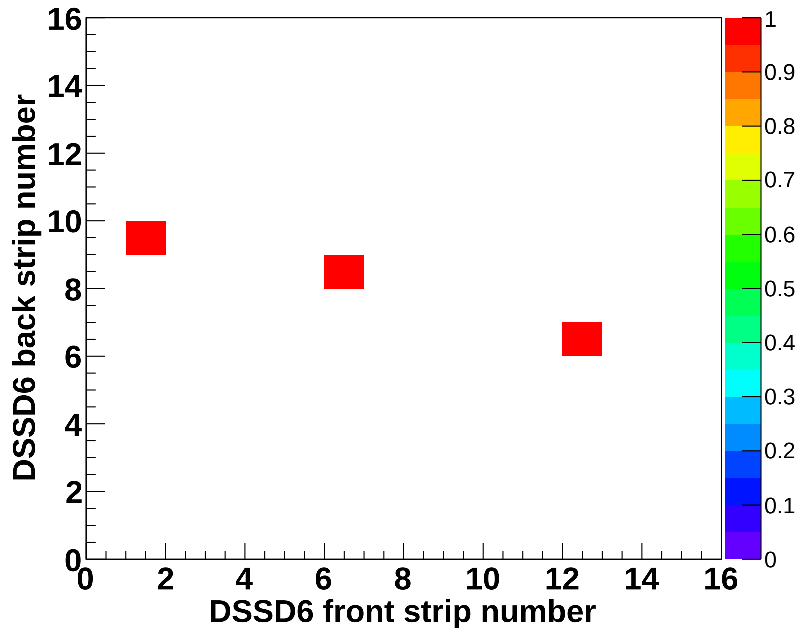

Figure 6.22: Hitmap of delayed two proton events which are obtained from the 2 dimensional plot front and back strip number of DSSD6.

behavior of exotic nuclear systems. Overall, this research sheds light on the decay mechanisms and nuclear structure, contributing to our understanding of rare and intriguing phenomena in nuclear physics.

References

[1] nndc.bnl.gov

[2] Y. Blumenfeld, Physics 15.177 (2022).

[3] D. S. Ahn, Phys. Rev. Lett. 129, 212502 (2022).

[4] Rolfs CE, Rodney WS. Cauldrons in the Cosmos. Chicago: Univ. Chicago Press(1988)

[5] Tanihata I, *et al.*, Phys. Rev. Lett. 55, 2676 (1985)

[6] Hansen PG, Jonson B. Europhys. Lett. 4, 409 (1987)

[7] Hansen PG *et al.*, Annu. Rev. Nucl Part.Sci. 45, 591 (1995)

[8] Tanihata I, J. Phys. G. 22, 157 (1996)

[9] Riisager K. Residence in Forbidden Regions. Dissertation, AarhusUniversity, Aarhus, Denmark (1994)

[10] Shwab W *et al.*, Z Phys. A 350, 283 (1995)

[11] Minamisono T *et al.*, Phys. Rev. Lett. 64, 2058 (1992)

[12] T. Otsuka *et al.*, Phys. Rev. Lett. 104, 012501 (2010)

[13] J. Erler *et al.*, Nature **486**, 509 (2012).

[14] A. Miller *et al.*, Nature physics **15**, 432 (2019).

[15] G. A. Lalazissis, D.Vretenar, P.Ring, Nucl. Phys. A **650**, 133 (1999).

[16] D.Suzuki *et al.*, Phys.Rev.Lett. 103, 152503 (2009)

[17] L.Lalanne *et al.*, Phys.Rev.Lett. 129, 122501 (2022)

[18] C.Thibault *et al.*, Phys.Rev.C **12**, 644 (1975).

[19] U. Datta *et al.*et al., Phys.Rev.C **94**, 034304 (2016).

[20] S. Chakraborty *et al.*et al., Phys.Rev. C **96**, 034301 (2017).

[21] A. Ozawa, T. Kobayashi,*et al.*et al., Phys.Rev. Lett. **84**, 24 (2000).

[22] I. Tanihata, J. Phys. G **22**, 157 (1996).

[23] G. Audi and A. H. Wapstra, Nucl. Phys. A**595**, 409 (1995).

[24] D. Guillemaud-Mueller *et al.*, Nucl. Phys. A**426**, 37 (1984).

[25] N.Paar *et al.*, Phys.Rev.Lett. 94, 182501 (2005).

[26] Hai Liang Ma *et al.*, Phys.Rev. C. 85, 044307 (2012)

[27] A. A. Leistenschneider, *et al.*, Phys.Rev.Lett. **86**, 5442 (2001).

[28] P. Adrich *et al.*, Phys.Rev.Lett. **95**, 132501 (2005).

[29] P. J.Woods and C.N.Davids Ann.Rev. Nucl. Part.Sc. **47**, 541 (1997).

[30] M J G Borge, Phys.Scr. 014013 (2013).

[31] M. Pfuetzner *et al.*, Rev. Mod. Phys. **84**, 567 (2012).

[32] R. Barton *et al.*, J. Phys**41**, 2007 (1963).

[33] J. C. Hardy, AIP Conf. Proc. **518**, 229–238 (2000)

[34] Yonghao Gao *et al.*, Scientific Reports **10**, 9119, (2020).

[35] J. Ray *et al.*, EPJ **66** , 02089 (2014).

[36] U. Datta *et al.*, AIP **2038**, 020020 (2018).

[37] M. Mougeot *et al.*, Nature physics 17, 1099 (2021).

[38] D.Lubos *et al.*, Phys.Rev.Lett. 122,222502 (2019).

[39] Magdalena Gorsa, Physics 4(1), 364 (2022).

[40] K. Auranen *et al.*, Phys.Rev.Lett. 122,222502 (2019).

[41] R.Clark *et al.*, Phys.Rev.C 122,222502 (2020)

[42] S. Frauendorf and A. O. Macchiavelli , Phys.Rev.Lett. 122,222502 (2020)

[43] L.Caponi *et al.*, Phys.Rev.C 94,024314 (2016);

[44] R. D. Page *et al.*, Phys. Rev. C 49, 3312 (1994).

[45] H.J.Rose and G.A.Jones Nature 307, 245 (1984).

[46] P.B.Price *et al.*, Phys.Rev.Lett. 54, 297 (1985).

[47] C.Mazzocchi *et al.*, Phys.Lett 532B, 29 (2002).

[48] A.Gulielmetti *et al.*, Phys.Rev.C 56,R2919 (1997);

[49] A.Gulielmetti *et al.*, Phys.Rev.C 52, 740 (1995).

[50] V.V.Elomaa *et al.*, Phys. Rev. Lett. 102, 252501 (2009).

[51] H. Schatz *et al.*, Phys. Rep. **294**, 167 (1998)

[52] H. Schatz *et al.*, Phys. Rev. Lett. **86**, 3471 (2001).

[53] S. Lahiri and G.Gangopadhyay Int. Jour. of Mod. Phys. E **21**, 1250074 (2012).

[54] K. Auranen *et al.*, Phys. Lett. B **792**, 187 (2019).

[55] J. M. D'auria *et al.*, Nuclear Physics A **301**, 397 (1978).

[56] P. Das *et al.*, Jour. of Phys. **1643**, 012127 (2020).

[57] M. Wang , G.Audi , Chin. Phys. C **36**, 1603 (2012).

[58] P. Das, U. Datta , *et al.*, Phys. Rev. C **108**, 064304 (2023).

[59] P. Sanger *et al.*, FAIR Project Report,2020.

[60] Karin Markenroth, Ph.D. Thesis, Exploring th Exotic,Experimental investigation far from stability, 2001.

[61] Razvan Lica, Ph.D. Thesis, Development of the ISOLDE Decay Station and γ spectroscopic studies of exotic nuclei near the N=20 "Island of Inversion", 2017.

[62] J. Blachot, Nucl. Data Sheets **113**, 2391 (2012).

[63] E. S. Paul *et al.*, Phys. Rev. C **53**, 2520 (1996).

[64] A. Gelman, J. B. Carlin, H. S. Stern, *et al.*, CRC Press, Boca Raton, Florida, 2013.

[65] J. Buchner, A. Georgakakis, K. Nandra, *et al.*, Astrophys. **564**, 015805 (2014).

[66] G. Ashton *et al.*,, Astrophys. J. Suppl. Ser. 241, 27 (2019)

[67] J. Kostensalo, J. Suhonen, K Zuber, Accepted Physics Letters B, (2022)

[68] M. Aggarwal, Phys. Rev. C. **89**, 024325 (2014).

[69] S. Kumar et al., Nucl. Data Sheets **137**, 1 (2016).

[70] G. Gurdal and F.G.Kondev, Nucl. Data Sheets **113**, 1315 (2012).

[71] Y. B. Zel'dovich Sov. Phys.—JETP 11, 812 (1960).

[72] V. I. Goldansky Nucl. Phys. 19, 482 (1960).

[73] J. Janecke Nucl. Phys. 61, 326 (1965).

[74] B. A. Brown Phys. Rev. C 43, R1513 (1991).

[75] B. J. Cole Phys. Rev. C 54, 1240 (1996).

[76] W. E. Ormand Phys. Rev. C 53, 214 (1996).

[77] B. Blank *et al*. Phys. Rev. Lett. 94, 232501 (2005).

[78] C. Dossat *et al*. Phys. Rev. C 72 054315 (2005).

[79] B. Blank and M. Ploszajczak Rep. Prog. Phys. 71, 046301 (2008).